TECHNISCHE UNIVERSITÄT WIEN

Diploma Thesis

# A Systematical Numerical Study on Transcranial Extracorporeal Shock Wave Therapy (ESWT)

by

Jonas Flatscher

carried out at the

**Institute of Chemical, Environmental and Bioscience Engineering**

in cooperation with the

**Ludwig Boltzmann Institute**

submitted to the

**Technische Universität Wien**

Master's programme Biomedical Engineering

**Supervisor**

Redl Heinz, Univ.Doz. Univ.Prof. Dipl.-Ing. Dr.techn.

**Co-Supervisor**

Slezak Cyrill, Assoc. Prof. PhD

Location, Date

Jonas Flatscher

# Abstract

In the recent years the field of application of extracorporeal shock waves (ESW) has been extended to other areas of the body, including the use for minimally invasive operations or stimulation of the brain. However, the skull acts as a protective barrier and influences the focus position and shape of the focal zone and pressure signal due to its acoustic properties and irregularity. This makes it challenging to predict the behaviour of the pressure waves when penetrating the skull bone.
In this thesis, using the MATLAB-toolbox k-Wave, an attempt is made to compare the different shock wave technologies and to investigate their behaviour as they propagate through the skull. For this purpose, models for the electromagnetic (EM), piezoelectric (PE) and electrohydraulic (EH) shock waves are devised and applied to a CT of the skull bone using different bone attenuation models, and the simulation in a plain water bath is used as a reference to investigate the impact of bone as a barrier based on various bone attenuation models. The pressure distribution and signals are recorded and used to determine the advantages and disadvantages of the observed technologies in this application area.

# Kurzfassung

Momentan wird versucht, das Einsatzgebiet der extrakorporalen Stoßwelle (ESW) auf weitere Körperareale zu übertragen, unter anderem auch die Verwendung für minimal-invasive Operationen oder Stimulationen am Schädel. In einem solchen von Knochen dominierten Areal ist eine Vorhersage des Verhaltens pauschal nicht möglich, denn der Knochen verändert aufgrund seiner unregelmäßigen Struktur und akustischen Eigenschaften die Position des Fokusses und Form des Drucksignals.
In dieser Arbeit wird mithilfe der MATLAB-Toolbox k-Wave versucht, die unterschiedliche Stoßwellen-Technologien zu vergleichen und deren Verhalten beim Durchdringen des Schädelknochens zu untersuchen. Dazu werden Modelle für die elektromagnetisch (EM), piezoelektrische (PE) und elektrohydraulische (EH) Stoßwelle erstellt und auf ein CT des Schädelknochens mit unterschiedlichen Absorptions-Modellen für Knochen angewandt; als Referenzsignal wird eine Simulation im Wasserbad herangezogen. Unterschiedliche Parameter werden aufgezeichnet und zur Bestimmung der Vor- und Nachteile der untersuchten Technologien in diesem Einsatzgebiet herangezogen.

# Contents

# Introduction

Ultrasound-based medical devices are widely used in humans, the application areas range from imaging methods to urinary stone treatments [65, 35, 75], but is also used as stimulation and therapy of the human musculoskeletal system [32, 33, 54]. There have also been attempts to apply it on the central nervous system, both as a minimally invasive surgical method (eg. ExAblate), and as a stimulation in Alzheimer's patients [74]. However, the brain is surrounded by a thick layer of bone, which represents an acoustical barrier for ultrasound propagation, not only dampening the pressure signal, but also affecting its shape and scattering it. Increasing computational power in recent years has created a way to simulate ultrasound at a reasonable resolution, and even to predict its propagation through the skull.

For this purpose, the simulation toolbox k-wave is used to compare different technologies for the generation of shock waves - an extremely thin, high pressure waveform - in the ultrasound range when penetrating the skull bone. The aim is to determine which of the technologies is most suitable to be applied transcranially and which limitations the bone imposes as a barrier.

The first chapter is devoted to a brief introduction to the physical principles necessary for the occurrence of so-called non-linearities: these are essential for the generation of shock waves and differentiate them from conventional ultra-sound medical devices. Subsequently, a short overview of the different applications of shock waves and the different technologies for their generation is given. Then the experimental setup and the implementation in the Matlab toolbox k-Wave will be presented. Finally, based on the conducted simulations the investigated technologies are compared to their applicability to bone-penetrating scenarios and further potential improvements are discussed.

# 1 Acoustic Waves

Acoustic waves travel in a longitudinal way, the pressure is transferred through small temporary displacements in the same direction as the wave propagation. The medium is either compressed or rarefied, the particles oscillate around their origin (see figure 1.1); mechanical energy is transmitted without mass transfer.

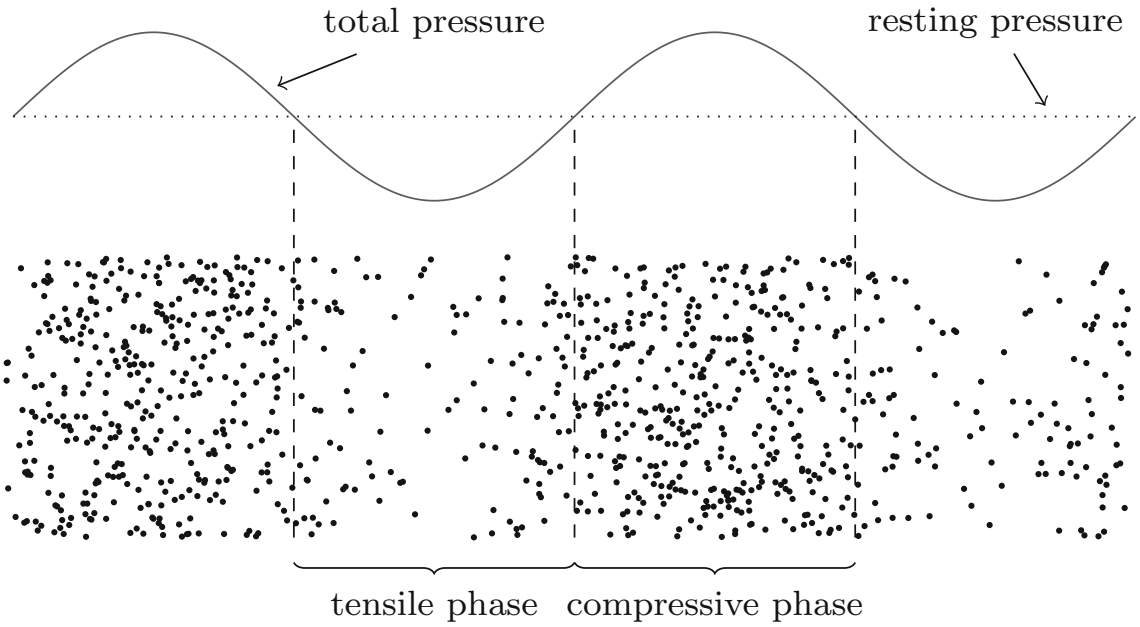


Figure 1.1: The total pressure is the sum of the resting pressure and the pressure changes; this results in a compression or rarefaction of the material particles.

In contrast to electromagnetic waves (e.g. light, radio, x-rays), where particles travel through space, acoustic waves rely on the presence of a physical medium: A propagation in an empty space (vacuum) is not possible. This implies a strong relationship between the medium and the acoustic properties of the acoustic wave.

The main focus in the following research lies on the use of ultrasound, which is the frequency range higher than the audible range. As the ability to perceive high frequency sounds is diminished with age, the lower limit ranges from 16 kHz to 20 kHz, though the American National Standards Institute (ANSI) defines it as sound at frequencies greater than 20 kHz.

## 1.1 Mechanics of Shock Waves

As the name already reveals, the typical shock wave is a sudden pressure change comprised of a compressive pressure wave with a steep gradient, followed by a smaller tensile phase. A part of the particles move faster than the speed of sound of the medium which creates the typical shape as the accumulate at the leading edge as can be seen in figure 1.2.

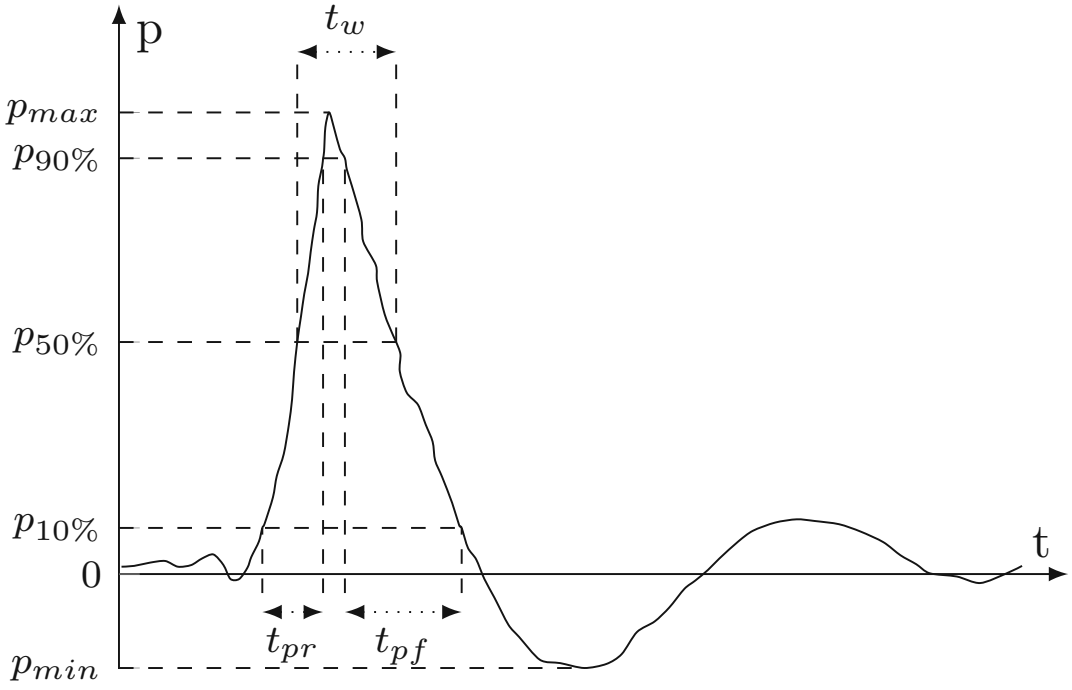


Figure 1.2: A typical measurement of a shock wave.

There are several parameters which are used to describe a shock wave signal [65]:

- $p_{max}$ - maximal pressure reached, depending on the device used between a few MPa up to over 100 MPa;
- $p_{min}$ - maximal negative pressure in the tensile wave, typically only a fraction of $p_{max}$;
- $t_{pr}$ - pulse rise time: time for a pulse to rise from 10 % to 90 % of the maximum peak pressure (in soft tissue longer than in water [75]); decreases with increasing power [7]. In water a shock wave generated by an applicator typically has a duration of a few µs, the rise time is most of the times less than 5 µs;

- $t_{pf}$ - pulse fall time: time for a pulse to fall again from 90 % to 10 % of the maximum peak pressure;
- $t_w$ - pulse width (FWHM - full-width half-maximum), width of the pulse at half amplitude $p_{50\%}$ of the peak pressure;

The appearance of shock waves is not limited to the ultrasound spectrum, two well known examples are the sonic boom at supersonic aircraft and the shock wave created by an explosion, but the main focus of this work is the propagation of shock waves in the human body and the interaction with human tissue. In contrast to a common sine wave often found in medical ultrasound used for imaging (figure 1.3), the frequency band in shock waves is much wider: it ranges from 100 kHz up to 20 MHz.

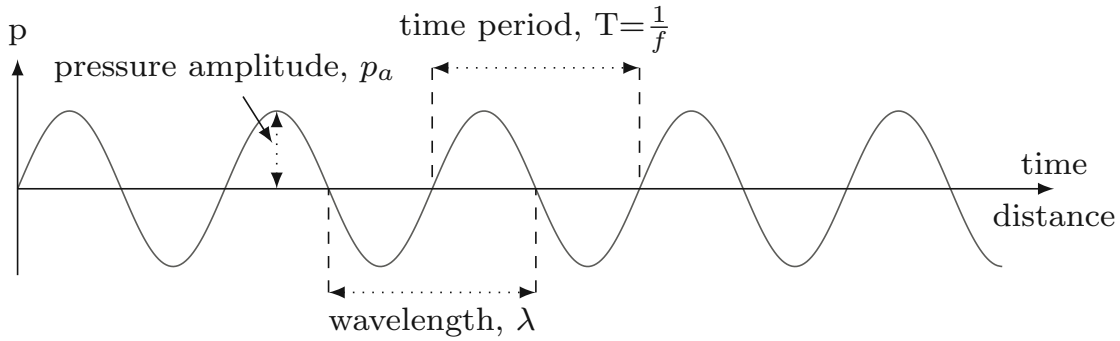


Figure 1.3: A sinusoidal pressure wave and its characteristic parameters; depending on the type of measurement either the frequency $f$ or the wavelength $\lambda$ can be determined.

## Shock Wave Effects

A comparison of different shock wave studies and their influence on tissue is difficult due to the use of different devices and the lack of available documentations [17]. A different sound field may trigger also a different biological reaction. While for some devices the whole target may be possible to envelop in the pressure field, an applicator with a smaller focal zone leads to a completely different pressure distribution. Furthermore, in *in vitro* experiments the target is often placed in a falcon tube for easier handling. Unfortunately, the pressure waves are refracted, and the cells may be treated with only a fraction of the pressure. A reduction of 11 % in the pressure showed a different biological reaction; therefore every possible disturbance factor should be eliminated. Another aspect to keep in mind is to maintain a distance between the focal zone and surfaces with an abrupt change in acoustic impedance.

Otherwise, this could lead to a reflection and a secondary focus, thereby increasing the forces and possibly changing the outcome [44].

Several biological effects are correlated with the use of shock waves in the ultrasound range [16, 44, 33, 66]:

- improved blood flow/perfusion;
- generation of stem cells;
- increased production of TGF-$\beta$1[1];
- higher gene expression of bone morphogenetic proteins;
- higher angiogenesis[2];
- cavitations;
- micro-lesions in tissue which stimulates regeneration;
- mechanical deformation of cells which may improve the activation of ion channels and improve gene expression.

The exact biological mechanisms behind those effects on the other hand are mostly still unknown; one mechanism which is studied in more detail is the release of cellular ATP through the shock wave and the subsequent activation of extracellular signal-regulated kinase (ERK) for enhanced cell proliferation and wound healing [5].

## Cavitation

A cavitation is an indirect effect which can be observed in certain liquids. After the alternating compression-tension phase caused by the shock wave the static pressure of the liquid can fall below its vapour pressure during the tensile phase and can develop a vapour filled cavitation. This bubble grows and collapses, generating a secondary shock wave. At close interfaces with a high acoustic impedance difference the bubbles can not collapse uninterrupted - they collapse asymmetrically, applying a force on the boundary. This can lead to so called micro-jets which have a high energy and can erode surfaces and damage tissue. Next to dynamic fatigue, squeezing

[1] Transforming Growth Factor
[2] Formation of blood vessels.

and shear induced failure, the generated micro-jets are one of the main reasons for kidney stone comminution [44, 75].

Next to an increase in viscosity of the environment, also a higher shock rate is associated with a reduction of the effects of cavitations - although for latter it is unclear if the device is not able to recharge properly (which powered by high voltage capacitors in the kV range), the pressure needs time to normalize inside the tissue or the time in between the pulses are lower than the primary cavitation bubble lifetime (up to 5 s) [53, 62, 16, 63]. A high repetition rate would therefore decrease the effect of cavitation bubbles and the damage they cause [75]- which is favourable in tissue stimulation. After a primary bubble collapses, the remaining secondary bubbles can serve as nuclei for the next pulse cavitation.

Although the phenomenon is rarer in soft tissue, cavitations can also occur there - it is believed that a trapped gas bubble may serve as a nucleus [75]. One has to be careful to apply the shock wave close to regions with a large change in acoustic impedance like bones or gas-filled areas, e.g. the lungs: the reflected pressure wave increases the tensile pressure and by that also the occurrence of cavitations which may damage the nearby tissue. Cavitations are in general associated with cell damage and generating micro-bleedings by rupturing blood vessels - latter could improve healing of the surrounding tissue [66]. There is a disadvantage, though: haematoma are possible, and the thereby increased amount of fluid increases the probability of further cavitation bubbles if the treatment is continued. For a therapeutic use regions with a high blood perfusion should be avoided. Patients with bleeding diathesis and use of anti-platelet, anti-thrombotic or anticoagulant medications have therefore to be especially careful, and medication is necessary to discontinue to reduce risks of the treatment [53, 62, 40, 75].
The effects of cavitations in soft tissue are chaotic in their appearance, hard to predict and difficult to observe. Therefore for a non-destructive use-case it would be best to avoid them *in vivo* [44].

### Cumulative Shear Mechanism

Shock waves develop a force at the borders of areas where a change of acoustic impedance occurs, e.g. kidney stones, but also at less distinctive boundaries some force effects can be experienced. The effect of a shock wave depends on the applied

pressure: with low pressures the cells get stimulated by reversible deformation, while at higher pressures the cells and its surrounding structures may rupture [40].

While a single low pressure shock wave is not strong enough to significantly damage soft tissue, according to Freund et al. [40] the tissue needs to relax until it reaches its unstrained state to be as resilient as before the loading. This may not be possible if a high pulse frequency (>6 Hz) is applied, which could lead to an accumulation of the strain and thereby damage the tissue. As the interstitial tissue is not able to recover completely in about 1 s, an even lower delivery rate slower than 1 Hz is suggested.

## 1.2 Ultrasound in Medical Devices

The usage of Ultrasound in medicine is manifold: Next to its usage in diagnostic and imaging, it is used in therapeutic devices. Ultrasound is able to heat up the tissue, and possibly even damage it in this process; at higher pressures it can also tear it apart and cavitations are possible. An example for the therapeutic use is the warming of deeper tissue layers and thereby accelerate the healing process [2]. Another popular application is the diminution of kidney stones which reduces the need for a surgical intervention. In the following subsections some ultrasound applications are presented.

### Medical Imaging

Currently, one of the main application of ultrasound in medicine is the use for ultrasonic imaging: A source emits an acoustic signal in the ultrasound frequency, simplistically thought of as a periodic sine signal in the MHz range, which travels through the tissue which is being examined. Due to the interaction with the tissue some of the wave energy is absorbed, but some is reflected or scattered in various directions. The geometry and the acoustic properties of the material determine the ratio on how the energy is divided. By measuring the reflected waves it is possible to reconstruct the composition of the tissue and thereby the anatomy.

### High Intensity Focussed Ultrasound (HIFU)

High intensity focussed ultrasound (HIFU) is a mostly destructively used technique; it is able to increase the temperature in the focal spot to more than 70°C in less than

3 seconds. This causes a coagulative necrosis in the focal spot and thermally ablates the targeted tissue. The typical frequency for HIFU is between $1 - 10$ MHz, with $2 - 4$ MHz being the most popular range. There is ongoing research focussing on a minimal invasive removal of several different tumours, as well as Uterine fibroids and even transcranial MRI-guided surgery for reducing tremors by a thalamotomy[3](e.g. ExAblate[4]).

As a side effect the excessive amount of energy entering the body may result in a skin burn, since skin has a higher absorption than other soft tissue [54]. To prevent overheating cooling or very large applicators of the tissue are needed [37]. One has to be especially careful when applying ultrasound techniques to the skull, though: standing waves may develop from the reflections and cause haemorrhages in the brain [55].

### Low Intensity Pulsed Ultrasound (LIPUS)

Low Intensity Pulsed Ultrasound (LIPUS) is an ultrasound therapy with a short signal burst of 200 µs and a main frequency of around 1.5 MHz, but a lower repetition rate of about 1 kHz. This therapy consists of short sessions and is applied over a longer period.

Several micromechanical and biological effects have been observed: an increase in gene expression, transcription factors and stem cell activation, mainly for bone regeneration have been observed. Although these effects seem very promising, and due to the pulsatile application thermal effects are negligible, the healing rates are not consistent and vary a lot in between different studies [33].

### Shock Wave Lithotripsy (SWL)

Shock Wave Lithotripsy (SWL) was the first medical application of shock waves, while the original use was to research the impact of rain drops and micro-meteorite on the wings of aircraft [35]. SWL is a non invasive method for the destruction of hardened masses like stones in kidney and gallbladder. A stationary device is used to generate a high energy and high pressure shock wave with a rather low repetition rate and is focussed through the body; the therapy consists of a few hundred to several thousand shock waves. It is assumed that a synergy of circumferential squeezing, spallation, cumulative shear and cavitations at the surface are the main reason for

[3]Opening of the thalamus and selective destruction of a part of it.
[4]For certain surgeries FDA approved minimal invasive HIFU.

stone diminution, the remaining debris can then be additionally dissolved chemically and are excreted through the urinary tract.

### Extracorporeal Shock Wave Therapy (ESWT)

There are also several non-destructive uses for low pressure shock waves: an acceleration in the healing of living tissue has been reported. It shows effectiveness in erectile dysfunction [67], plantar fasciitis [92] and tendinopathies [88], dissolves calcifications in joints and tendon insertions [66], and also promotes the unification of pseudoarthrosis[5] [33, 60]. A typical application for therapeutic use consists of up to 4000 impulses with a repetition rate of up to 8 Hz, while the energy flux intensity may vary between the different shock wave devices from 0.05 to 0.8 $\frac{\text{mJ}}{\text{mm}^2}$ [33, 44]. In a recent study [74] also the effect of shock waves as stimulation of the brain has been researched and an improvement of neuropsychological scores have been reported.

### Boiling Histotripsy

Boiling histotripsy could be described as a mix between HIFU, LIPUS and shock waves: A short 'train' of several high pressure shock waves ($60 - 120$ MPa) is generated, followed by a longer pause. The goal is to mechanically fractionate tissue by creating boiling bubbles when the tissue reaches 100°C. The gas bubbles grow and violently collapse destroying the tissue thereby. The additional high pressure shock wave fractionate the tissue even further [3]. This technique allows the body to remove the destroyed tissue debris more easily than damage caused by a thermal necrosis alone [70], but also promotes an immunogenic cell death which can be helpful in a cancer treatment [18]. If thermal effects are desired, though, shock waves should be handled carefully because inducing non-linearities reduces their predictability [50].

[5]Fractured bones which do not grow together after 6 months and have a resemblance to a fibrous joint.

## 1.3 Pressure Equations

In the following section a brief introduction to the physical equations governing the wave propagation is given in order to describe why shock waves appear [31, 13].

The achievable speed of sound $c$ - the 'velocity' at which an acoustic wave propagates - depends on the material. As discussed in this and the following section, the speed of sound also depends on the temperature of the material and the pressure of the signal. If the speed of sound is given as a material constant, it usually refers to the speed of sound $c_0$ for small amplitudes in a resting medium at 20°C. Solid materials have in general a higher speed of sound than fluids and gases (e.g. steel: $c_0 \approx 5600\frac{\mathrm{m}}{\mathrm{s}}$, water: $c_0 \approx 1500\frac{\mathrm{m}}{\mathrm{s}}$, air: $c_0 \approx 343\frac{\mathrm{m}}{\mathrm{s}}$).

Apart from the frequency $f$ the wavelength

$$\lambda = \frac{c}{f} \tag{1.1}$$

in a material also depends on its speed of sound. Another medium property is the characteristic impedance

$$Z = \rho\, c, \tag{1.2}$$

which can be calculated with the speed of sound and the density $\rho$. It is a measure on how much a medium is opposing the longitudinal wave propagation.
In every liquid and fluid medium the total pressure $p_t$ depends on the total density $\rho_t$ and the temperature $T$:

$$p_t = p_t(\rho_t, T), \tag{1.3}$$

but because of the nature of ultrasound the changes are so quick that the temperature exchange is often negligible:

$$p_t = p_t(\rho_t), \tag{1.4}$$

The sound pressure $p$ is then defined as the deviation of the total pressure $p_t$ from its resting value (in most cases the ambient pressure) $p_0$; the same is true for the

density $\rho$:

$$\begin{aligned} p &= p_t - p_0, \\ \rho &= \rho_t - \rho_0. \end{aligned} \tag{1.5}$$

The pressure $p$ can be approximated with a Taylor series (Appendix A.1) to

$$p(\rho) = \frac{A}{1!}\left(\frac{\rho}{\rho_0}\right) + \frac{B}{2!}\left(\frac{\rho}{\rho_0}\right)^2 + \frac{C}{3!}\left(\frac{\rho}{\rho_0}\right)^3 + ... \tag{1.6}$$

with

$$A = \rho_0 \left(\frac{d\,p}{d\,\rho}\right)_0, B = \rho_0^2 \left(\frac{d^2\,p}{d\,\rho^2}\right)_0, C = \rho_0^3 \left(\frac{d^3\,p}{d\,\rho^3}\right)_0. \tag{1.7}$$

Next the equations for impulse and mass conservation are introduced, which connect the pressure and the density and are derived from the fundamental physical principles while neglecting the viscosity:

$$\begin{aligned} \nabla(p) + \rho_t \frac{d\,\vec{v}}{d\,t} &= 0, \\ \nabla \cdot (\rho_t\,\vec{v}) + \frac{\partial\,\rho}{\partial\,t} &= 0. \end{aligned} \tag{1.8}$$

The vector $\vec{v}$ represents the particle velocity, the speed of a parcel of fluid as it oscillates in the direction of the acoustic wave, caused by the exposure to pressure.

Normally the density changes $\rho$ are small in comparison to the resting value $\rho_0$ and therefore higher orders of a Taylor series (1.6) can be neglected. The changes to the base values $\rho_0$ to $p_0$ in (1.7) are normally very small, which results in

$$p = \left(\frac{d\,p}{d\,\rho}\right)_0 \rho = c^2\,\rho \tag{1.9}$$

with

$$c^2 = \frac{d\,p}{d\,\rho} \approx \left(\frac{d\,p}{d\,\rho}\right)_0. \tag{1.10}$$

Also for small changes $\rho_t$ can be replaced with $\rho_0$. If equation (1.9) is applied to a diagnostic ultrasound with around 2 MPa, a density change in water of below 0.1 % is observed, even with an already high shock wave value of 100 MPa the change would still be less than 5 %.

Using the same assumptions of only small changes of the velocity in equation (1.8)

the total acceleration $\frac{d\vec{v}}{dt}$ can be replaced through the local acceleration $\frac{\partial\vec{v}}{\partial t}$ which results in

$$\begin{aligned} \nabla p + \rho_t \frac{\partial \vec{v}}{\partial t} &= 0, \\ \rho_0 c^2 \ (\nabla \cdot \vec{v}) + \frac{\partial p}{\partial t} &= 0, \end{aligned} \tag{1.11}$$

and can be transformed into the partial derivative

$$\Delta p = \frac{1}{c^2} \frac{\partial^2 p}{\partial t} \tag{1.12}$$

through elimination of the particle velocity $\vec{v}$. For small amplitudes this description may be suitable, but for higher pressures a more general form has to be applied.

## 1.4 Non-Linear Effects

As discussed above, in most use-case scenarios the pressure amplitude of an ultrasound is relatively small - the generated particle velocities $v$ are smaller than the speed of sound of the material $c$ the wave propagates in.

Since the pressure depends on the local density due to a non-linearity in (1.4) the approximation of the speed of sound in (1.10) does not suffice for higher pressures. It has to be noted that the pressure wave is moved through convection (the particles show a small net-velocity in the direction of propagation)

$$v = \frac{p}{\rho_0 c_0} \tag{1.13}$$

as well. Therefore instead of (1.10)

$$c = v + \sqrt{\frac{dp}{d\varrho}} \tag{1.14}$$

has to be used, where $\varrho$ represents the alternating density. Moreover the derivation of the pressure to the alternating density $\frac{dp}{d\varrho}$ is developed to the second element of the Taylor series and not only the first, while $\varrho$ is replaced with $\varrho_0 \frac{v}{c_0}$:

$$\frac{dp}{d\varrho} = \frac{A}{\varrho_0} + B\frac{\varrho}{{\varrho_0}^2} = \frac{A}{\varrho_0}\left(1 + \frac{B}{A}\frac{v}{c_0}\right) = {c_0}^2\left(1 + \frac{B}{A}\frac{v}{c_0}\right) \tag{1.15}$$

with

$$A = \varrho_0 \left(\frac{d\,p}{d\,\varrho}\right)_0 = \varrho_0\, c_0^2. \tag{1.16}$$

This can then be inserted in (1.14). Since the particle velocity $v$ is assumed to be small in comparison to the speed of sound $c_0$ only the first term of the power series (Appendix A.2) is needed to describe the root function and can be expressed as

$$c = c_0 + \left(1 + \frac{B}{2\,A}\right) v. \tag{1.17}$$

The ratio

$$\frac{B}{A} = \frac{\varrho_0}{{c_0}^2} \left(\frac{d^2 p}{d\varrho^2}\right) \tag{1.18}$$

(also found as *BonA*) is used as the second order non-linearity parameter of the material, sometimes also $\beta = \left(1 + \frac{B}{2\,A}\right)$ is found instead. A high *BonA* indicates the ability to form higher harmonics, the parameter is pressure and temperature dependent[6] [9, 13]. As described in (1.17), the speed of sound of the material depends on the local particle velocity; as a consequence, high pressure waves with a higher particle velocity can propagate faster than low pressure waves. For example, a sinusoidal wave steepens up during its propagation on the front while flattening at the back. At a certain distance - which is called *shock formation distance* $\bar{x}$ (also found as *discontinuity distance*) - a sinusoidal wave would evolve a discontinuity with a vertical tangent:

$$\bar{x} = \frac{{c_0}^2}{\hat{v}\,\omega\,(1 + \frac{B}{2A})} = \frac{\rho_0\,{c_0}^3}{\hat{p}\,2\,\pi\,f\,(1 + \frac{B}{2A})}, \tag{1.20}$$

with $\hat{v}/\hat{p}$ as the peak particle velocity/pressure and $\omega$ the angular frequency. Since a sound wave cannot roll over, the wave will steepen up until it reaches a sawtooth-like appearance (see figure (1.4)).

[6] The pressure, but also the speed of sound is temperature dependent. While the temperature change through the wave dissipation can often be neglected, observing shock waves other than at room temperature may significantly influence the behaviour. The more sophisticated formula with the temperature term included can be noted according to Bjorno [13] with

$$\frac{B}{A} = 2\rho_0 c_0 \left\{\left(\frac{\partial c}{\partial p}\right)_T\right\}_{\rho=const.} + \frac{2c_0 T\beta}{c_p} \left\{\left(\frac{\partial c}{\partial T}\right)_p\right\}_{\rho=const.}, \tag{1.19}$$

where $\beta$ is the volume coefficient for thermal expansion, T is the absolute temperature, and $c_p$ the specific heat at constant pressure.

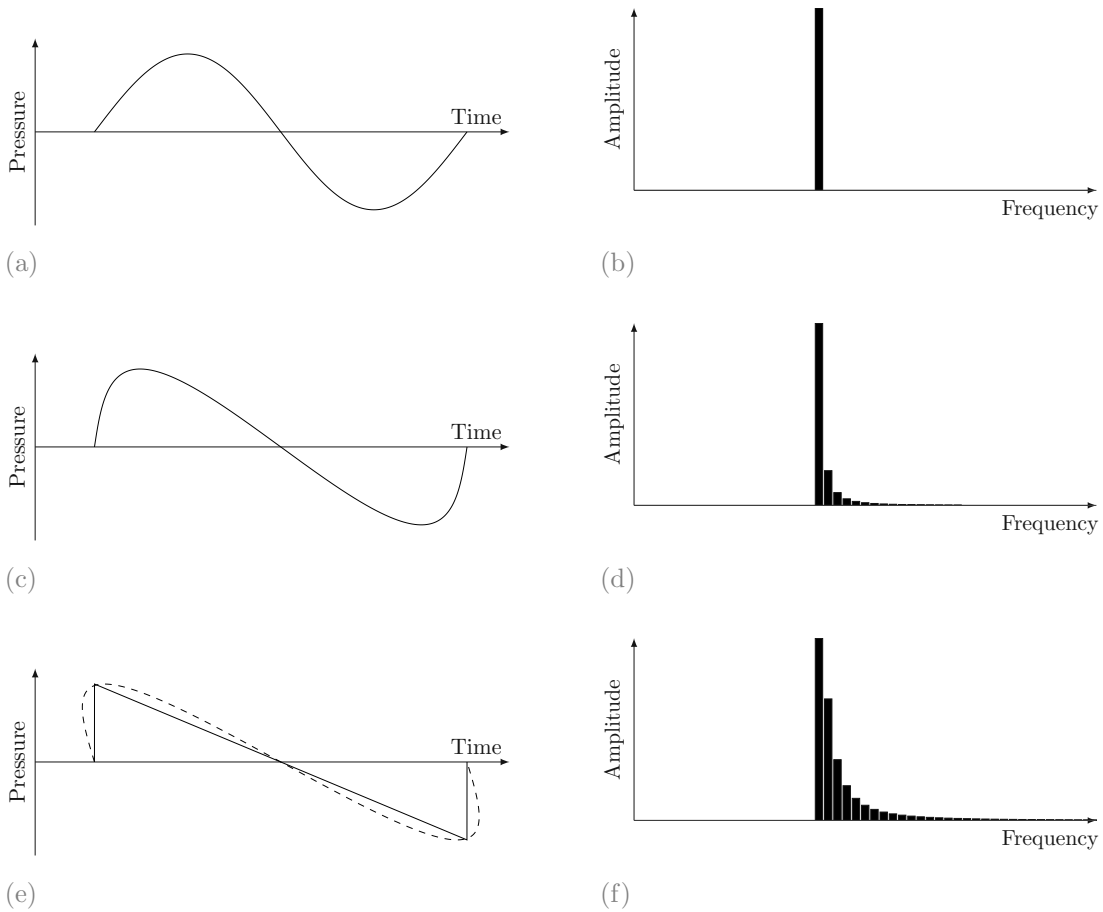


Figure 1.4: The start signal (a) which slowly evolves (c) into its final sawtooth-like shape (e) because the higher pressure parts are moving faster; since it is physically not possible to have two pressure values at the same spot (*dashed line*), the overlapping parts in (e) are cancelled out and a signal with an infinite slope develops. During this process the energy is moved to the higher harmonic frequencies, and can be made visible by plotting the signals in the frequency domain ((b), (d), (f)) respectively.

Non-linear effects do not change the acoustic energy, they merely cause a rearrangement of the frequency distribution - the energy is shifted to its higher harmonic frequency components (see figure 1.5). The amplitude of higher harmonics are inversely proportional to its harmonic number [13].

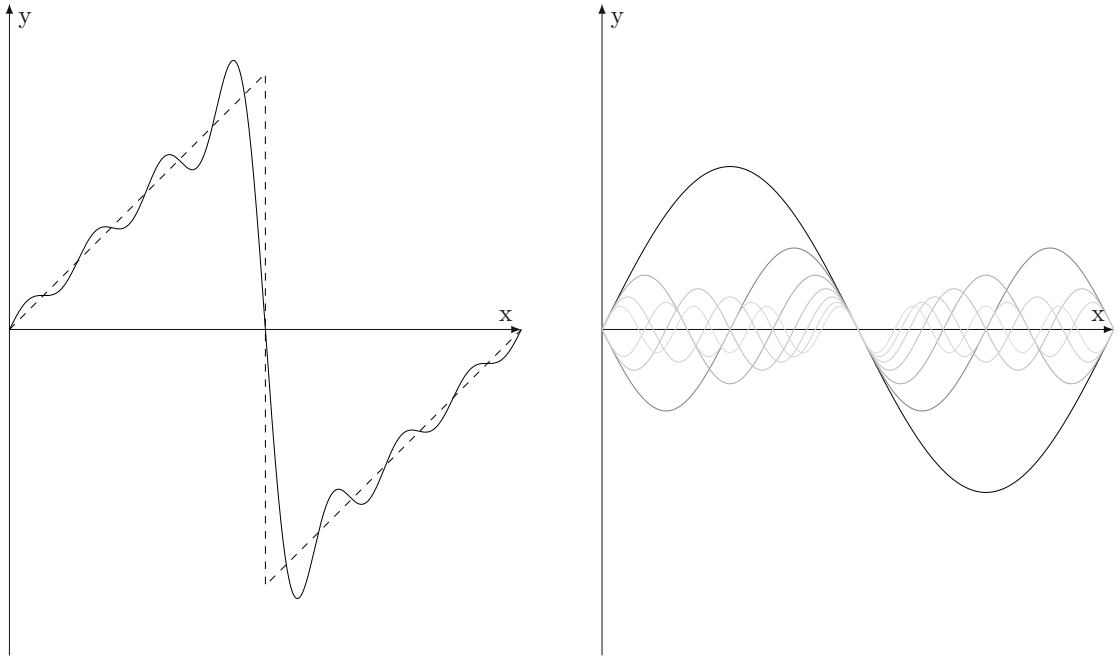


Figure 1.5: *(Left)*: A sawtooth function (dashed) and an approximation (solid) with a combination of six sine functions - a higher number improves the result.
*(Right)*: The single sine components of the approximation, composed of a start-sine function and 5 of its harmonics.

There are two major effects in a material which influence the signal form: first dissipation, which arises from viscosity, heat conductivity and relaxation processes, and second non-linearity, which leads to the formation of higher harmonic frequencies. These transformations are only possible with high pressure waves: the harmonic frequencies of a low pressure wave would be damped before they are present in a noticeable amount to trigger this transformation, especially since the absorption increases with higher frequencies. Similar to that, after travelling over a long distance, the sawtooth-like shape disappears again and due to the higher dissipation of the higher frequencies only the low frequency components remain [6, 13].

For example, using the equation (1.20) a sinusoidal wave in water with a pressure of 10 MPa and a frequency of 1 MHz at the source would take less than 2 cm to build a shock front, while a 1 MPa pressure wave with 0.5 MHz would need around 30 cm; long range therapy devices have a natural advantage in producing shock waves [16]. In comparison, the discontinuity distance in air of 100 Pa ($\approx$ 134 dB) at 10 kHz is more than 5 m - while the attenuation is neglected.

## 1.5 Energy

In general sound in a fluid physically consists out of the oscillatory elastic compression and the oscillatory displacement [31, 59]. Therefore the sound energy is composed out of a potential and kinetic component, and as consequence also the energy density $ED$ is composed out of a potential and kinetic part:

$$ED = ED_{pot} + ED_{kin} = \frac{\bar{p}^2}{2\,\rho_0\,c^2} + \frac{\rho_0\,\bar{v}^2}{2}. \tag{1.21}$$

For a plane propagating wave the the equation (1.13) can be used to either replace the time mean particle velocity $\bar{v}$ or the time mean pressure $\bar{p}$ which results in a total energy density of

$$ED_{total} = ED_{pot} + E_{kin} = \rho_0\,\bar{v}^2 = \frac{\bar{p}^2}{\rho_0\,c^2}, \tag{1.22}$$

the unit is $\frac{\mathrm{mJ}}{\mathrm{mm}^3}$. As a single sensors provide a measurement of pressure $p(t)$, the energy flux density $EFD$, often denoted as pressure integral intensity (PII), is more commonly used by the different manufacturers:

$$EFD = \int_T \frac{p(t)^2}{\rho\,c}\mathrm{d}t. \tag{1.23}$$

The energy flux density is the energy $E$ passing through an area in a time interval $T$, the unit is $\frac{\mathrm{mJ}}{\mathrm{mm}^2}$. It is also possible to calculate the energy flux density only on the compressive ($EFD_+$) or the tensile ($EFD_-$) part of the pressure.

The sound energy in an observed volume $V$ can then be obtained by integration of the energy density $ED$:

$$E_V = \int_V ED\,\mathrm{d}V = \int_V \rho_0\,\bar{v}^2\,\mathrm{d}V = \int_V \frac{\bar{p}^2}{\rho_0\,c^2}\,\mathrm{d}V. \tag{1.24}$$

If the energy flux density $EFD$ is at hand, the energy which passes through the area $A$ in the observed time $T$ can be calculated using

$$E = A \cdot EFD = A \int_T \frac{p(t)^2}{\rho_0\,c}\mathrm{d}t. \tag{1.25}$$

Also here the value can be calculated integrating over the total duration of the pulse, or only over the compressive or the tensile pressure part. The energy is often summed up over a whole therapy session to describe the total treatment energy. The negative aspect about specifying the device using the energy is that as it is obtained

by integration all the properties of the pressure signal like gradient or pulse profile are lost, the same applies to the EFD. Furthermore, it is measured at a single point and therefore only valid for a very small area.

# 2 Shock Wave Applicators

A shock wave applicator is a handheld or fixed device, which transforms electrical into acoustic energy, which is focussed through the body to reach a high pressure amplitude signal. The application is either possible with a stationary device (e.g. Lithotripter) or with a handheld device for therapeutic treatment. If the shock waves are applied to a deeper tissue, a locating device is helpful (e.g. CT, Ultrasound, MRI). Due to the heterogeneity of human tissue and the often very narrow focal zone an imprecise focus is a common problem with ESWTs. A simulation for targeting would often be favourable, but a real time guidance is still not possible due to the high computational effort [46]. An alternative would be an approximation using ray-tracing with an inclusion of Snells Law and a prediction of attenuation [15].

## 2.1 Source Types

There are three popular ways to generate a shock wave signal: first, by generating an expanding plasma in liquid, second, by using a coil similar to a loudspeaker and third, by using piezoelectric crystals .

### Electrohydraulic Applicator

The electrohydraulic (EH) impulse is generated by charging a high voltage capacitor and discharging it across two electrodes in the with liquid filled reflector. A plasma channel is created, generating a gas bubble which unfolds with supersonic speed and thereby compressing the neighbouring fluid - a high pressure peak emerges, which propagates radially. For a higher efficiency and accuracy a reflector is used which directs the acoustic wave towards the focal centre. There a two popular types of reflectors, an ellipsoid reflector with a narrow focal spot and a parabolic reflector with a soft focal area (see figure 2.1 and 2.2 ).
This is the only type of reflector where the pressure signal at the point of origin is already a shock wave, the other two methods generate a signal in the form of a smooth oscillation, which steepens up on the way to the focus: with those technologies the rise time is strongly pressure dependent [7].

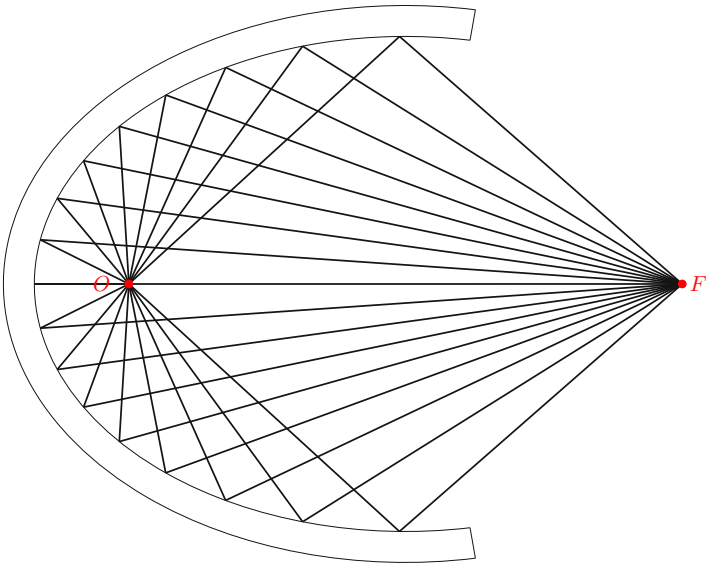


Figure 2.1: An EH applicator with an ellipsoidal reflector and its pathway of the emerging shock waves.

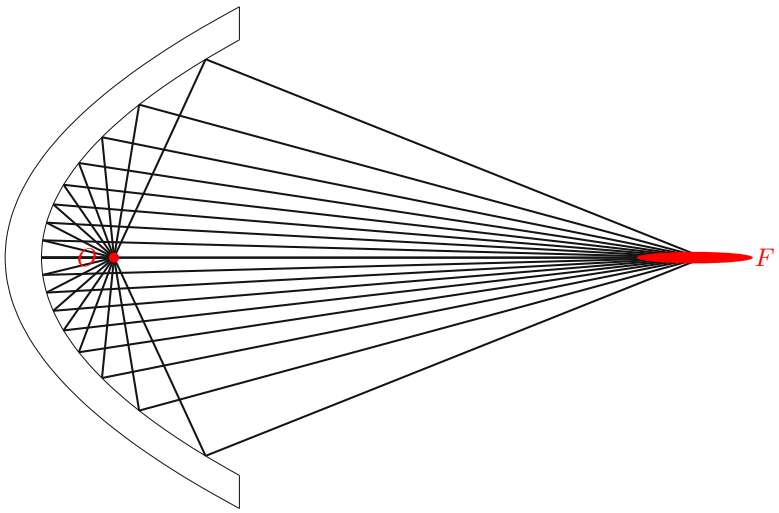


Figure 2.2: An EH applicator with a parabolic reflector and its pathway of the emerging shock waves. The focal area is bigger with the same source than the ellipsoidal reflector and therefore provides a 'softer' focal zone.

There are quite a few disadvantages, though:

- the shock wave losses are higher due to the higher initial frequencies;
- there is a primary (i.e. direct, caused by explosion) and a secondary (reflected by reflector) shock wave - which could influence cavitation [75];
- the origin may vary due to stochastic fluctuations and therefore the focus varies as well - not suitable for experiments where reproducibility is a requirement;
- high maintenance - the electrodes need to be replaced regularly;
- its use is unpleasant due to the very loud sound.

### Electromagnetic Applicator

The electromagnetic (EM) applicator is based on the principle of induction and works similarly to a loudspeaker. There are two configurations: one uses a flat coil whose shock waves are focussed through an acoustic lens; the other configuration is based on a cylindrical coil with a paraboloid metal reflector. Both work in a similar way: A coil is isolated with a non conductive membrane from a conductive metallic membrane. When a current flows through the coil, a magnetic field is induced, which induces a current in the metallic membrane and generates an opposing magnetic field - the membranes repel each other and create a pressure wave. This technology can also reach the highest pressures amplitudes (≈100 MPa), while being very stable in the outcome, having a long lifespan and low maintenance costs. Depending on the type of reflector the focussing is either achieved through the acoustic lens or with the metallic reflector.

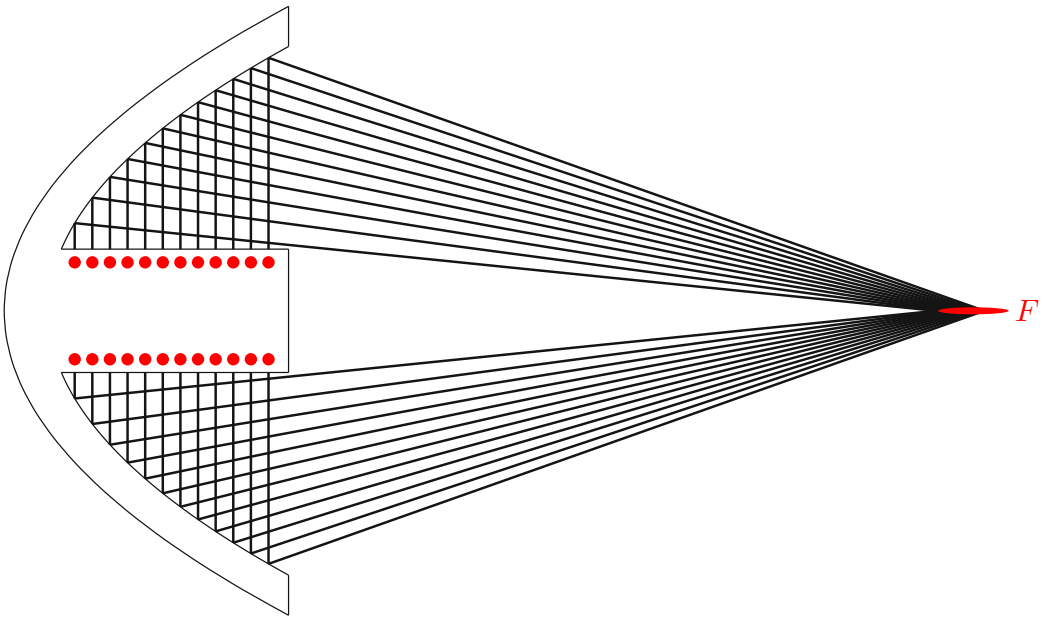


Figure 2.3: An EM applicator with a cylindrical coil (*red*) and its pathway of the emerging shock waves. The reflector has a typical paraboloid shape; even if the focus area is still small, focussing on a single spot is not possible.

## Piezoelectric Applicator

The piezoelectric (PE) applicator has a close relationship to the medical imaging ultrasound device, but there are still some basic differences. Both rely on the same technology, a piezoelectric crystal which rapidly expands if an electrical field is applied. In contrast to the periodic signal in an ultrasound device, the shock wave applicator relies on a short, but high voltage excitation signal as well as on a different crystal alignment in the shape of a sphere section with a geometrical focal point. The signal generated in the ultrasound device is composed out of periodical sine oscillations in a lower frequency spectrum. Due to the low pressure, non-linear effects arise to a lesser degree. The shock wave devices try to achieve the opposite: high output pressure in a single pressure peak, preferably with a high frequency spectrum. Non-linearities are desired but do not evolve unless the waves travel a certain distance or are bundled in the focal centre, the frequency range at the crystal is between several kilohertz up to 10 MHz. In some devices it is possible to steer the focus to a certain degree without moving the applicator by controlling the piezoelectric-elements individually [69].

The size of the single piezoelectric element, the manifold possibilities in their arrangement and the ability to control each element individually makes it the most adaptable applicator. To achieve a small focal zone a large aperture is needed and the piezoelectric transducer, having no limiting factor in this regard, is therefore perfect for this purpose [75]. On the other hand, the output energy per area is limited and therefore for a high pressure signal a large applicator is needed [71]. At higher pressures the piezoelectric crystals 'ring' after excitation and create a pressure trail [75].

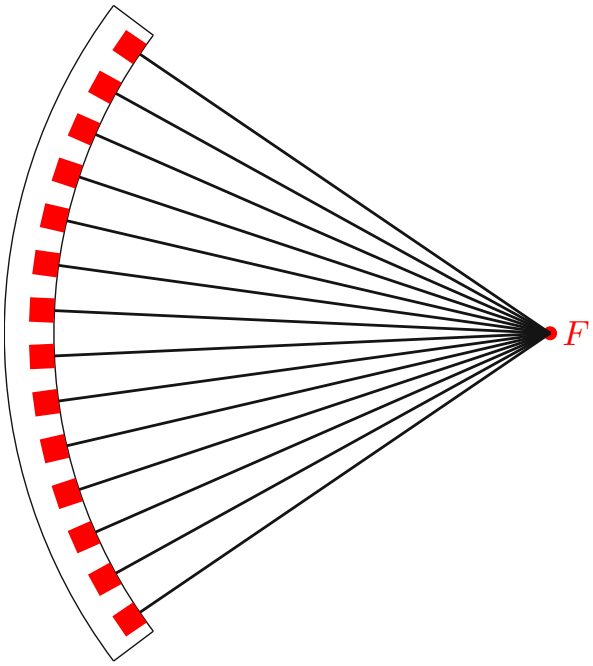


Figure 2.4: A Piezoelectric applicator and its pathway of the emerging shock waves.

## 2.2 Focal Zone

Due to shape of the applicator the focus is not limited to one single spot with high energy, but also expands to its surroundings - which is called the focal zone. It is mostly in an ellipsoidal shape, but may vary depending on the reflector and on the settings used.

### -6 dB Zone

The -6 dB zone marks the volume where the pressure exceeds half the maximum compressive pressure, commonly also the tensile pressure or energy density are used instead. Some reflectors have a very big focal zone, but only the very centre has a pressure high enough to be still classified as the -6 dB zone (mostly with a paraboloid reflector); other reflectors show a very sharp focus where almost the complete focal zone can be defined as -6 dB zone (with sphere sections found in PE applicators). The zone is no guarantee for any biological effects to take place [66]. To describe the focal zone only with the -6 dB zone it is not sufficient to fully characterize, since a loss of half the pressure is already a lot; neither does it reflect the treatment area [44, 7].

### 5 MPa Therapy Zone

Another way to characterize the focal zone is use the volume where the pressure exceeds 5 MPa. The 5 MPa zone makes it easier to compare the different reflectors to a certain degree, even though the pressure limit is rather arbitrary since no physical or biological effect is guaranteed either [66]. If new biological indications arise, the 5 MPa limit could be adapted to the pressure where a biological effect observed.

# 3 Experimental Setup

To correlate the actual effect with the induced signal the impact of the shock wave on the observed tissue has to be known. Reliable *in vivo* measurements are hard to achieve due the destructive placement of the sensors and the thereby related ethnic question. *Ex vivo* measurements are able to avoid the latter, but the uncertainty of having influenced the measurements with the placing of the sensor and the connected coupling losses still remain [1].
The typical setup for measuring the focal zone of the applicator in a water bath (figure 3.1) can not be compared to the actual application on tissue due to its heterogeneity, neither is it possible to apply as many measuring points as needed for this task.

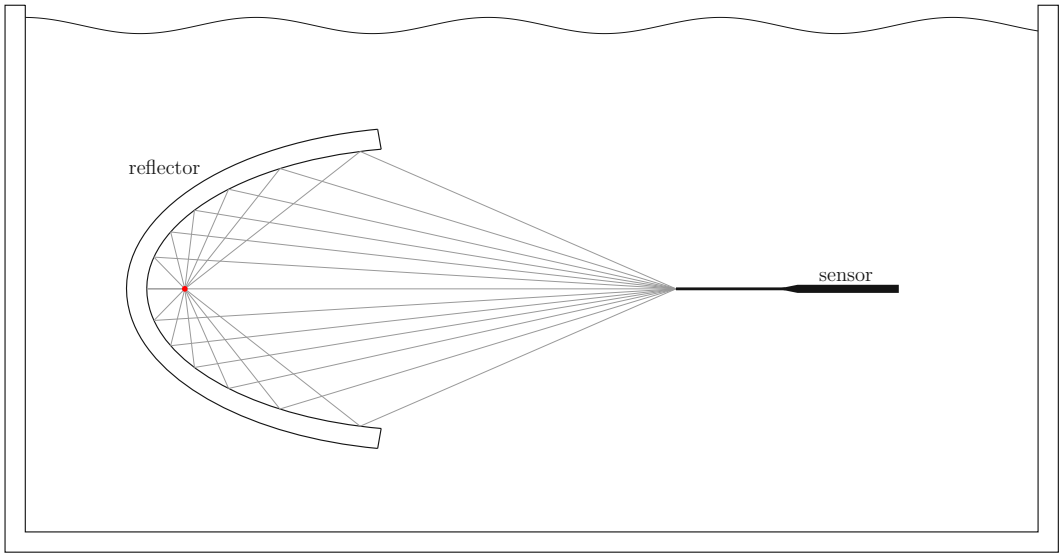


Figure 3.1: A typical setup to measure a shock wave reflector in a water bath.

If the influence of a material is to be observed, in this case the skull bone, it is normally placed in the water bath (figure 3.2) between the applicator and the sensor. To simulate a real application the water could be replaced with olive oil, which has a similar attenuation coefficient and non-linearity parameters as the human tissue [47].

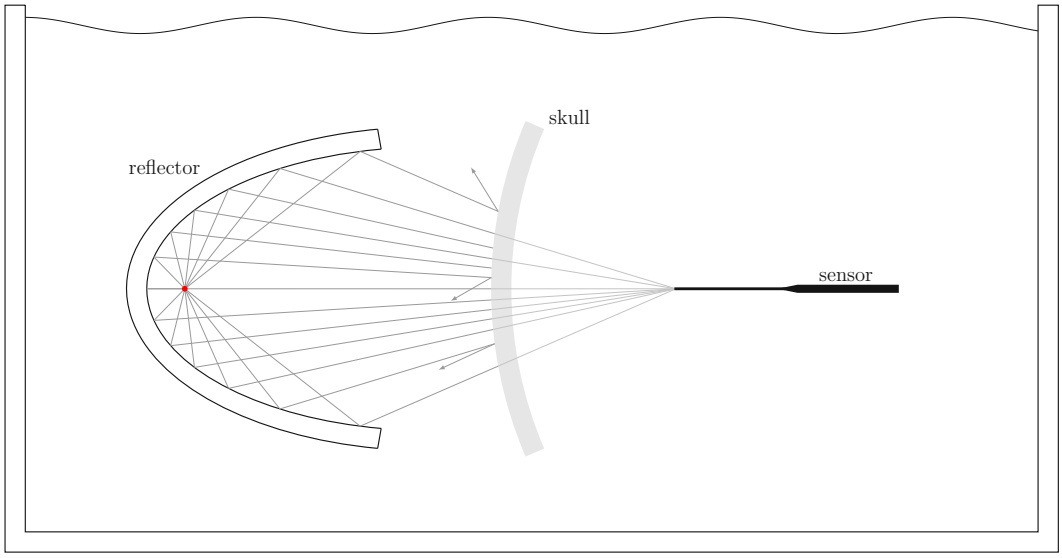


Figure 3.2: A typical setup to measure the influence of an introduced obstacle, in this case the skull.

While experimental measurements in combination with high precision sensors are nonetheless the standard, it was not possible to obtain all the different applicator technologies for a direct comparison.

For this reason a simulation was used: With the increase of the computational power in the last years, it is now even possible to calculate approximations for a realistic use-case with a common workstation. To increase the accuracy a more powerful device is needed, though. While the preparation of the simulation can be laborious, there are almost no restrictions on the placement of sensors and the material to observe.
In this case it is possible to obtain a complete pressure distribution for an application of a shock wave using a full head CT.

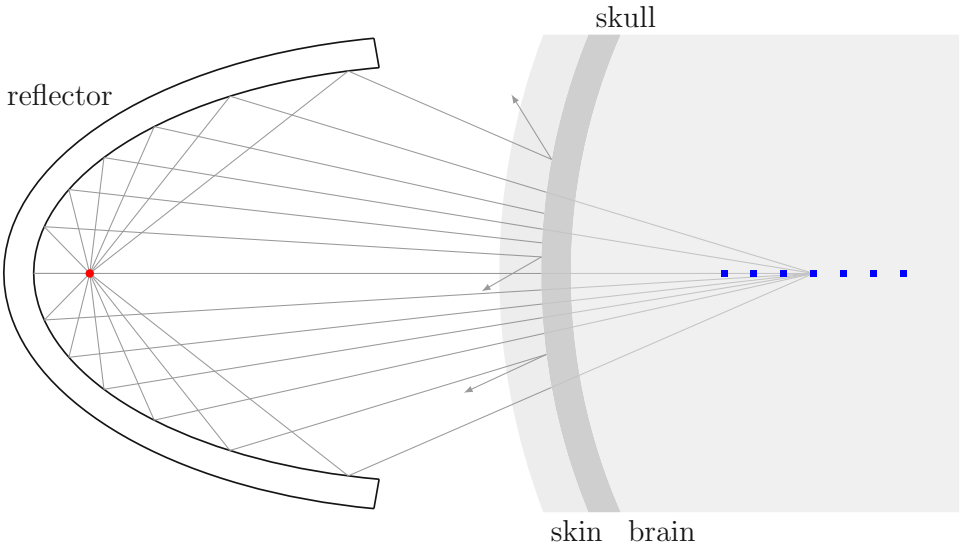


Figure 3.3: A simulation setup to measure the pressure distribution in the brain, with the blue dots representing the multiple possible recording positions.

To determine which shock wave technology is the most appropriate for this type of application, the three shock wave technologies are reconstructed with a total of five different applicators. These are then located in direct contact with a 3D volume prepared from a human CT. Sensors, which record the arriving signal, are then placed at different spots on the skull, while also a map with the minimal and maximal pressure for the whole medium is obtained. These data are then compared to determine which of the applicators are able to preserve its pressure signal properties through the natural acoustic barrier of the skull.

# 4 Target Tissue

The shock waves have to pass multiple layers before they reach their target, the brain. The first layer is the scalp, which can be divided again into five separate sub-layers; the total thickness is approximately 5 mm:

- **skin** - contains hair follicles;
- **connective tissue** - connects the skin to the layer below and is strongly vascularized;
- **aponeurosis** - tendon like structure associated with muscles of the forehead and neck;
- **loose connective tissue** - contains blood vessels;
- **pericranium** - outer layer of the skull bones.

The soft tissue is then followed by the approximately 6 mm thick skull bone, which has the typical sandwich form of a cancellous bone (Diploe) enclosed by an outer and inner cortical layer (lamina externa, lamina interna).
On the inside of the skull the three meninges can be found: The Dura mater, which is the stiffest one, followed by two softer membranes, the Arachnoidea mater and the Pia mater. The Pia mater forms the last layer before the brain and is firmly adhered to its surface while only being attached loosely to the Arachnoidea mater with a spiderweb-like structure. The space between the latter two membranes is called subarachnoid space and is filled with cerebrospinal fluid [28, 24].

## 4.1 Skull Tissue and Acoustic Wave Propagation

The main reason for the sparse use of ultrasound in the region of the skull is that the acoustic signal is not able to penetrate the skull properly without heating up the surrounding tissue. While in other regions the ultrasound applicator has to be moved around regularly to avoid damaging the tissue, the skull makes it even more difficult. The secondary heat dissipation originated from the skull can cause burns in the scalp and even damage the brain surface [29].

The poor propagation through bone is caused by several mechanisms:

- **absorption**
  The bone shows a much higher absorption than the surrounding tissue. The acoustic energy is translated into thermal energy and heats up the surrounding tissue [12]. The porous structure of the bone leads to multiple reflections inside the bone and even more absorption.

- **reflection**
  The acoustic impedance difference at the tissue/bone interface causes a high reflection of the acoustic waves. Further details can be found in section 4.2.

- **scattering**
  The curvature of the skull leads to another problem. As long as the incident pressure waves are perpendicular to the surface, no refraction occurs - which would only be possible if a piezoelectric applicator with the same curvature as the skull were used. In every other case the skull bone acts as an acoustic lens and due to the large gradient of the skull creates a second focus point through refraction rather close to its inner surface - which strongly limits its use. Small skulls may interact more due to their sharper geometry [42, 20].

Only the high absorption is a direct cause for the heat development, but the reflection and scattering mechanisms force the user to apply a higher energy in order to be able to penetrate the bone. The heating is rather quick: 10 s of ultrasound at the bone are able to create a temperature increase of around 10°C [29].

There are some approaches where a large applicator array is used, but the tissue has still to be constantly cooled. Another option would be to reduce the applied energy by correcting the phase aberrations electronically induced by the skull using 'phase correction' [1].

Soft tissue has a similar behaviour as a fluid with ultrasound, showing only slight variations, bone on the other hand is more complex. While soft tissue mostly supports the propagation of compressive waves and little to none shear waves, bone supports both. Additionally the bone structure and therefore its physical simulation

[1] A method to synchronize the piezoelectric elements to improve the pressure wave propagation according to the present obstacle - see section 5.4 for further explanation.

parameters are much more heterogeneous. The density and speed of sound between cortical and trabecular bone may vary by a factor of 2, and the porosity strongly depends on the observed position and bone. The trabecular elements (50-150 µm, separation of 0.5 to 2 mm [29]) are also close to the typical ultrasound frequency of 1 MHz. This structure is smaller than the resolution of the CT provided and while included in the attenuation coefficient, it is impossible to simulate their exact influence - a significant part of the attenuation is caused by these microstructures inside the bone [61], though. The exact composition of mineralized collagen and bone marrow considerably depends on the persons's sex and age; with advancing age a more rod-like structure develops [22]. Finding a universal model therefore may be a challenge.

There are several studies [45, 37] which deal with the topic of finding the optimal frequency in order to penetrate the skull - mostly with ultrasound and not with shock waves. These studies showed that frequencies above 1.11 MHz (acc. to [45]) or 1 MHz (acc. to [37]) are heavily distorted and absorbed (estimated loss at 1 MHz: 12 dB; at 1.3 MHz: 20 dB[2] [71]). This is a reason for heat generation and should be avoided - achieving a sharp focus is almost impossible.

While the rise in temperature is negligible for shock waves due to the low repetition rate, the high absorption losses remain.

Subsequently, the ratio of absorption and scattering to the total loss was investigated. According to Fry [27] the absorption loss is almost linearly proportional to the frequency (in the range of 0.4-1.2 MHz), while scattering is more frequency dependent [37, 22, 75]. It was also found that a low bone volume fraction (BV/TV - bone volume to total volume) increases the influence of scattering to the total attenuation, but a high BV/TV increases the absorption [22].

As a result it was suggested, that a frequency of 0.5 MHz for applicators with a spherical curved reflector (e.g. electrohydraulic, electromagnetic) or up to 1 MHz for reflectors with a phased array (piezoelectric) should be used. For every frequency above the focus is heavily influenced and should only be used with a phase correction - an uncorrected signal above 1.5 MHz has proved to be unsuitable [37].
The frequency also influences the focussability - a smaller focus can only be achieved

[2]The skull could be described as a low-pass filter which depends on the thickness of the skull [52].

by using a higher frequency [81, 30]. This fact already restricts the choice in the applicator technologies.

This strong frequency dependency could turn out to be a disadvantage for the electrohydraulic shock wave in the transcranial use-case: the piezoelectric and the electromagnetic signals start with a relatively low frequency signal and steepen on the way to its focus to finally generate a shock wave at the focal point. The electrohydraulic on the other hand generates a very high frequency shock wave signal right at the source - and could be far more distorted and absorbed while passing through the bone.

As mentioned before, the skull acts as a secondary focus lens - this restricts the accessible volume in the skull. In Sun et al.[38] it is suggested that only a volume of 8 cm $\times$ 8 cm $\times$ 4 cm (6 cm $\times$ 6 cm $\times$ 3 cm in Clement et al. [30]) can be accessed without significantly reducing the pressure amplitude. Very superficial locations can not be focussed in a controlled manner due to the high scattering.

Despite all of these obstacles it has been shown that it is possible to focus enough energy through the skull to even create lesions in tissue while leaving the skin across the scalp intact using a piezoelectric ultrasound applicator [30]. If a more repeated therapy is suggested or surgery is still advised, a replacement of the cranial bone with a more acoustic transparent material could be suggested to improve the signal transmission [56].

## 4.2 Attenuation Model

Attenuation is the general process of dampening a signal while it is passing through a material. There are several mechanisms which contribute to it: *Absorption* is the loss of energy through friction, which can be observed through a change in temperature [14]. At material interfaces or while passing through heterogeneous media, also *reflection* can be observed, which are caused by sudden changes in the acoustic properties of the material. If the incident angle is not perpendicular to this material change, also *diffraction and scattering* take place; the incident angle differs from the exiting angle, in a heterogeneous medium the wave is often scattered in different directions.

## Absorption

Absorption is caused when the density fluctuations get out of phase with the pressure wave fluctuations. If the wave frequency is low enough, most of the energy can be returned from the material with only being slightly out of phase and the absorption is low as well. At a higher frequency this energy exchange can not keep up and the thermal losses increase [14].
The absorption in this simulation is calculated by using the the power law absorption in the form

$$\alpha = \alpha_0 \, \omega^y, \tag{4.1}$$

where $\alpha$ [dB/cm] is the absorption coefficient, $\alpha_0$ [dB/(MHz$^y$cm)][3] the power law prefactor, $\omega$ the angular frequency and $y$ the power law exponent. For biological tissue the power law exponent is normally between 1 and 2 [52], the absorption coefficient ranges between 0.1 and 60 dB/cm.

This absorption coefficient describes how easily a pressure wave can penetrate a material - with a high coefficient, the wave weakens quickly; for a low value, the wave can penetrate the material easily.

For materials with a negligible shear modulus[4] this model should provide a good accuracy for most soft organic tissues. This is not the case for bone, the simulation is therefore limited to incident angles below a critical angle as will be further discussed in section 6.1

## Reflection

Reflections are created at the interface of two materials with different acoustic impedances; to reduce coupling losses the shock wave has to be applied in a medium with similar physical properties like the human tissue - since the body consists to

[3] for more details see A.3.
[4] The shear modulus describes the ability of a material to support shear stress - i.e. a force parallel to a surface while its opposing surface experiences an opposing force - and therefore to resist transverse deformations. A large shear modulus value indicates a rigid materials, while a small shear modulus value indicates a soft or flexible substance; fluids have a shear modulus of zero.

about 60 % of water, a water-bath or a water-based contact gel similar to the one used in ultrasound coupling is ideal. But there are reflections which cannot be avoided. The skull forms a natural barrier to acoustic waves, shock waves and ultrasound alike. Due to the high differences in the acoustic impedance of human tissue and the dense skull bone a large portion of energy is reflected at the different interfaces as the acoustic waves pass through. As mentioned in [29], most of the attenuation through bone is attributed to reflection and not absorption.

Applying Snell's law in an idealized setup where the shock wave passes normal to the surfaces through the different tissues is used as an approximation to the losses which are to be expected due to reflection. Absorption, refraction, scattering and diffraction depend on the geometry and are not included in this approach.

The transmitted pressure $p_t$ can be calculated by using the incident pressure $p_i$ and the transmission factor $T_p$

$$p_t = T_p * p_i \tag{4.2}$$

with

$$T_p = \frac{2 * Z_2}{Z_1 + Z_2}, \tag{4.3}$$

where $Z$ is the acoustic impedance of the material in front (1) and behind the interface (2). This has to be calculated for each transmission. If a pressure wave has to pass a skull bone in a water bath, the water/skull $T_{p,WS}$ is followed by a skull/water $T_{p,SW}$ interface, which results in

$$p_t = p_i * T_{p,WS} * T_{p,SW}. \tag{4.4}$$

The part which is reflected can be calculated by using the formula

$$R_p = \frac{Z_2 - Z_1}{Z_2 + Z_1} = T_p - 1; \tag{4.5}$$

for the energy and intensity the transmission coefficient is calculated differently:

$$R_i = \frac{(Z_2 - Z_1)^2}{(Z_2 + Z_1)^2} = {R_p}^2 \tag{4.6}$$

$$T_i = \frac{4\,Z_1\,Z_2}{(Z_2 + Z_1)^2} = 1 - R_i \tag{4.7}$$

The reflected part may reflect multiple times in between the different surfaces, but are neglected for this approximation.

In this approximation four layers are included with a total of three interfaces. This extends equation (4.4) to

$$p_t = p_i * T_{Water-Skin} * T_{Skin-Skull} * T_{Skull-Brain}. \tag{4.8}$$

With the transmission coefficients given in table 4.1

Table 4.1: Used materials and their corresponding acoustic impedance $Z$ (see equation 1.2); further material properties can be found in table 4.4.

| Material | $c_0$ [m/s] | $\rho$ [kg/m$^3$] | $Z$ [Ns/m$^3$] |
|---|---|---|---|
| Water | 1482 | 998 | $1479 * 10^3$ |
| Skin | 1590 | 1065 | $1693 * 10^3$ |
| Skull | 2160 | 1500 | $3240 * 10^3$ |
| Brain | 1550 | 1030 | $1597 * 10^3$ |
| Fat | 1450 | 950 | $1378 * 10^3$ |
| Muscle | 1547 | 1050 | $1624 * 10^3$ |
| Air | 343 | 1.2 | 412 |

the maximal transmitted pressure through the layers of the skull can be estimated to be 92.6 %, the transmitted power is about 79.7 % - a loss of at least 20 % in energy is therefore expected. In table 4.2 the influence of each interface is listed. Through measurements of the human skull the anticipated loss should be way higher: a drop of in pressure of $80 - 90$ % and also a widening and shifting of the focus should be expected [74]. One attempt to explain the low value of the approximation is next to to neglected scattering, the low speed of sound assigned to the observed bone and the assumed homogeneity. Latter is particularly significant since - due to the complex bone structure - a lot more interfaces may be introduced.

Table 4.2: Reflection and transmission on selected interfaces, in accordance with [91].

| Interface | Reflected pressure [%] | Transmitted pressure [%] | Transmitted energy [%] |
|---|---|---|---|
| Water - Skin | 6.8 | 106.8 | 99.5 |
| Skin - Skull | 31.4 | 131.4 | 90.2 |
| Skull - Brain | -34 | 66 | 88.5 |
| Water - Air | -99.9 | 0.1 | 0.1 |
| Air - Water | 99.9 | 199.9 | 0.1 |
| Air - Skin | 99.9 | 199.9 | 0.1 |
| Water - Fat | -3.5 | 96.5 | 99.9 |
| Fat - Muscle | 8.2 | 108.2 | 99.3 |
| Muscle - Bone | 33.2 | 133.2 | 89 |

It may be surprising that the transmitted pressure can be higher than the incident pressure, but the energy conservation is not violated since the energy is determined by both the pressure amplitude and the wave velocity.
The negative sign of the reflected pressure is caused by the lower impedance of medium 2, which reflects the incident pressure. In case of a total reflection, like most interfaces between tissue and air, the incident and reflected pressure sum up and the pressure gradient can be twice as high as in a homogeneous medium - which can lead to its destruction [91]. Such interfaces should therefore be avoided.

In figure 4.1 the intensity transmission coefficient for an interface between water to a second medium can be seen; it can be interpreted as a percentage of the energy which is not reflected and passes to the other material. The transmission coefficients are also inversely proportional to the pressure reflection coefficients, and as pointed out before, low coefficients should be avoided for the sake of the integrity of the tissue. At a water/air interface almost 100 % of the sound pressure is reflected and an application to the lung tissue can be quite dangerous, but also a build up of air bubbles in the coupling material can obstruct further transmission [44, 75, 1].

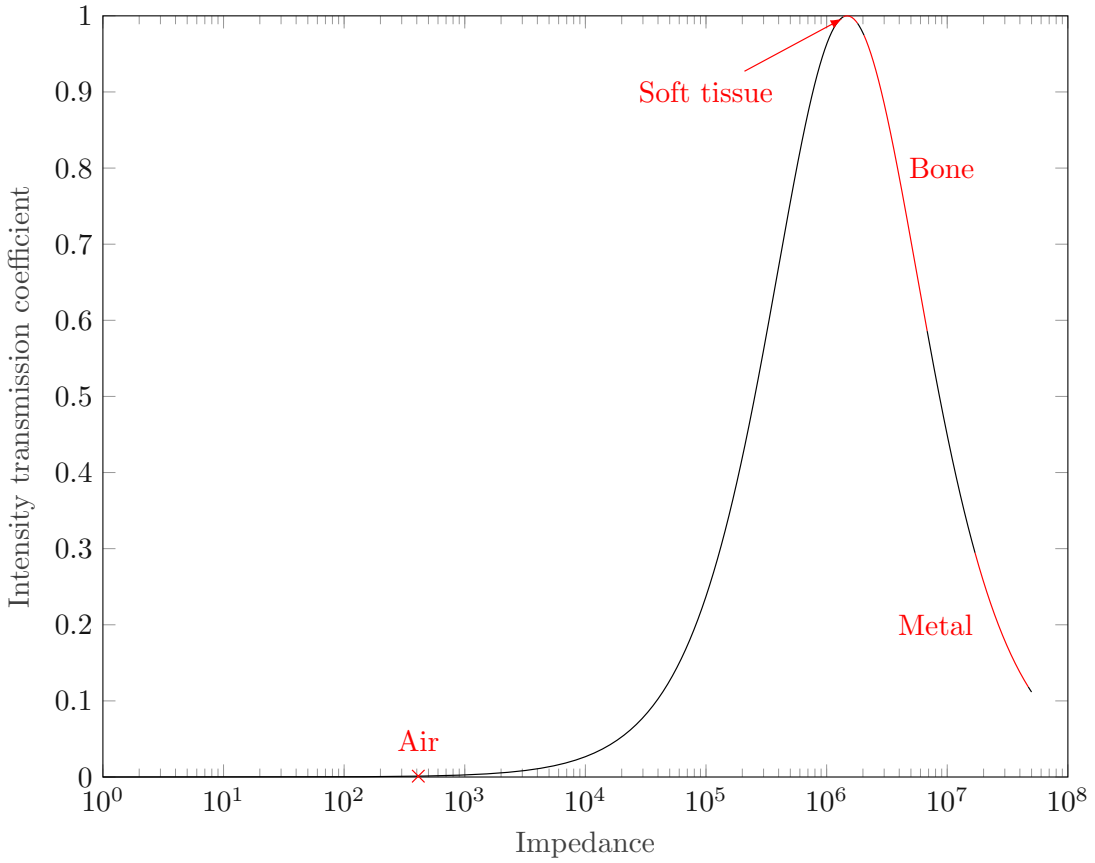


Figure 4.1: Intensity transmission coefficient for an interface between water and a second medium with the shock waves impacting normal to the interface; the marked zones in red show the transmission coefficients for some interfaces often found in real applications.

## Attenuation and Absorption Coefficients

In the literature the names 'absorption coefficient' and 'attenuation coefficient' are often used synonymously, but unfortunately they are not equivalent. While it is hard to find an exact definition for both of them, one could attempt to define them with their literal meaning. The absorption coefficient should include only the thermal losses through material particles and the fine microstructure found in organic tissue [29], the representative volume element (RVE) should be chosen in the correct magnitude of size; the material structure on this level should seem periodic. The attenuation coefficient on the other hand includes all the effects which leads to energy reduction at the measured resolution. Additionally to the absorption on the microscopic level also influences due to the macrostructure of the material are taken into account, therefore also the scattering is considered to some degree.

The thermal absorption coefficient is normally harder to determine and seldomly found in the literature, while the attenuation coefficient is much more common. For a lot of materials both should be interchangeable due to the macroscopic homogeneity of the tissue. For bone on the other hand this is not the case.

The thermal absorption coefficient in skull bone in Pinton et al. [29] was determined using a µCT at a resolution of 10 µm to be 2.7 $\frac{\mathrm{dB}}{\mathrm{MHz}^y\mathrm{cm}}$, the attenuation coefficient is quite a lot higher with values between 10 and 60 $\frac{\mathrm{dB}}{\mathrm{MHz}^y\mathrm{cm}}$, depending on the density values [61, 78, 29]. Low density values are a sign of a low total bone fraction and therefore of spongy bone, which result in more scattering and a higher attenuation. If both coefficients are known, the decision should be made based on the resolution at hand. For a very fine resolution where the macrostructures of the tissues are well visible, the absorption coefficient would be the better pick. On the other hand if the macrostructures can't be resolved appropriately, the attenuation coefficient may be a better choice since the fine structures contributing to the scattering can not be differentiated.

The resolution used in this work is with voxel size of 0.5 mm on the rough side and far closer to the resolution, which were used to create the attenuation values than the absorption coefficients. Therefore in the simulation the absorption coefficients are always replaced by the attenuation coefficients if both are known.

## 4.3 Target Preparation

As target tissue the Data from the Visible Human Project®[5] has been used. The CT data provided originates from a 72 year old male patient with a pixel size of 0.489 mm and slice thickness of 0.5 mm.

The DICOM data format was read into a 3D matrix with the resolution of 0.489 mm× 0.489 mm × 0.5 mm. The CT data was adapted in size to the higher resolution of the simulation using nearest-neighbour interpolation. The grey values provided by the image were then translated into the Hounsfield Unit (HU) with the information provided in the DICOM file.

[5] With Courtesy of the U.S. National Library of Medicine, https://www.nlm.nih.gov/research/visible/getting_data.html.

## Hounsfield Unit

The most common way to define the Hounsfield Unit (HU) is to apply the formula

$$HU = 1000 \frac{\mu - \mu_{water}}{\mu_{water} - \mu_{air}} \tag{4.9}$$

where $\mu$ is the linear attenuation coefficient for incident photons per thickness of the material and $\mu_{water}$ and $\mu_{air}$ the constants for the material air and water. It describes the attenuation of a material in relationship to water and on this basis the HU value can be used to identify the type of the tissue examined. The typical range for soft tissue is -150 to 200, bone can be found to be in the range of 200 to 2000.

## Tissue Clustering

To assign the different tissue parameters to the CT scan the tissues had to be identified first.
The approach to distinguish the layers using only the HU values failed due to the strong heterogeneity and the overlapping HU values of the different soft tissues, the spatial component has to be integrated for the tissue recognition. Attempts to cluster with DBSCAN [6] and to apply a k-means algorithm, both with the HU values included as an input parameter, failed for the same reason. The most reliable method proved to be identifying the bone using the HU values (HU $>$ 235) and declaring all voxels on top as skin, while assigning all voxels below the parameters of the brain (see figure 4.2).

There are also several low HU spots (HU $< -150$) spread in the medium. If the lower HU spots were located outside the skull, it was assumed to be the same material as the rest of the test environment and declared as water. Low HU spots inside the skull are assumed to be blood vessels or spaces where the cerebrospinal fluid would be found. For latter no non-linear parameters are available, and therefore were replaced with the parameters of blood (see figure 4.3).

[6] Density-based spatial clustering of applications with noise.

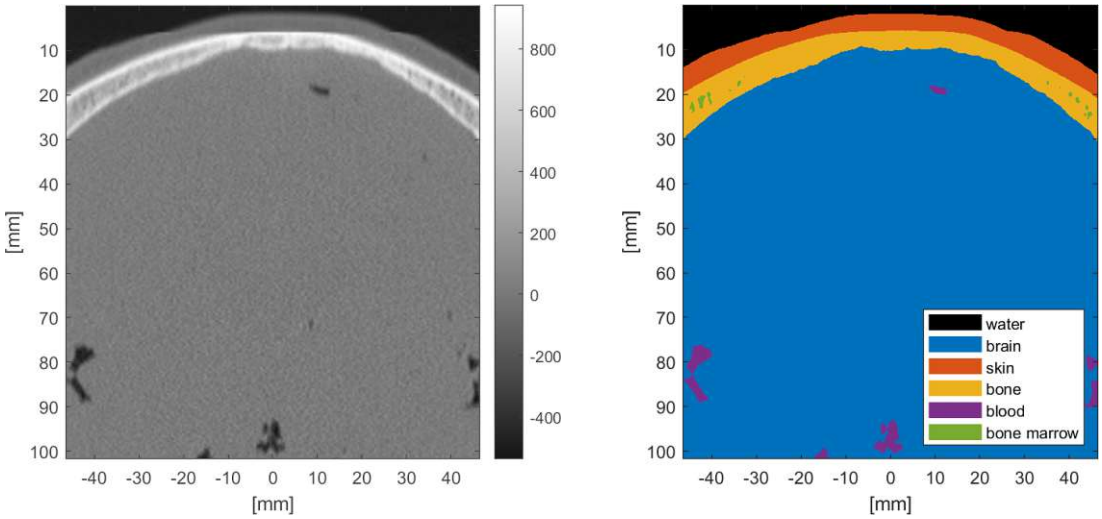


(a) CT, Hounsfield Unit (b) CT, clustered

Figure 4.2: Section of the CT and its clusterization.

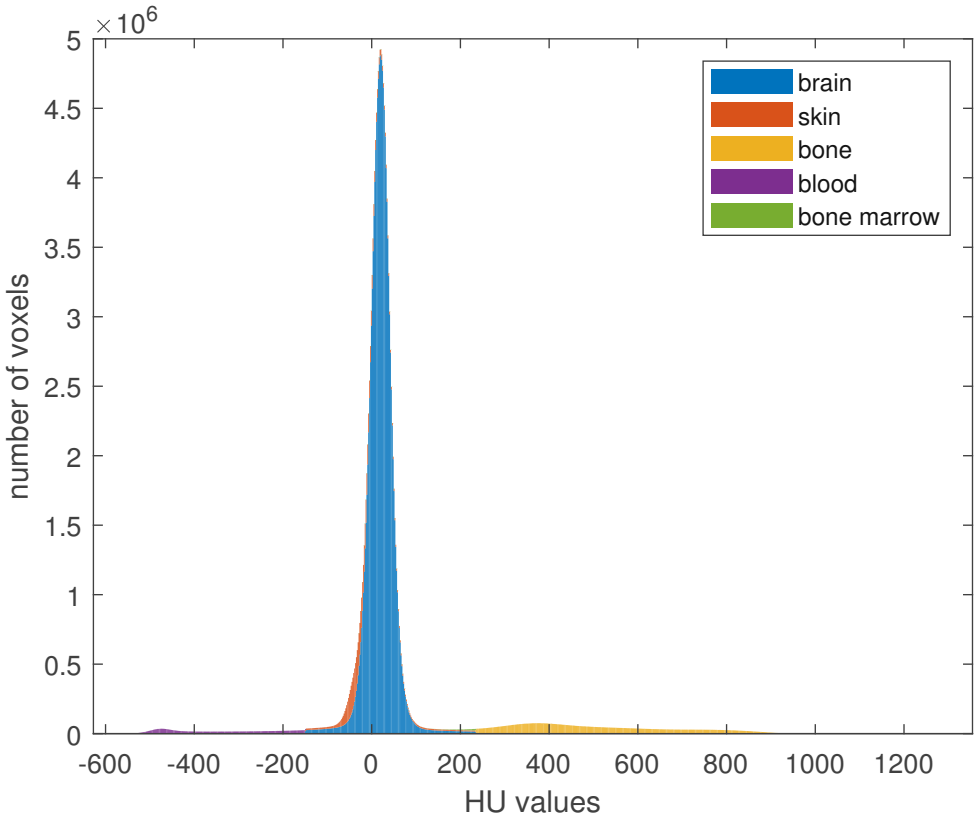


Figure 4.3: A stacked histogram of the CT at hand, clustered in to the defined tissues; a detailed version without the brain can be found in the appendix A.4.

The mentioned HU value of 235 as threshold for bone is based on the density to attenuation calculation - no attenuation values for a density with a lower value has been found. Therefore using this threshold also cavities inside the bone itself were observed. These were assumed to be bone with a very low BV/TV or as bone marrow. Unfortunately, also here no non-linearity parameters are available for this tissue type, but due to the high fat content of bone marrow a mix between bone and fat is assumed.
Those cavities are mostly found on locations outside the acoustic path of the applicator and are not expected to have a big impact on the simulation.

## Tissue Parameters

In order to use the data for simulating the values in the Hounsfield Unit (HU) of the DICOM were translated into density values using the function `hounsfield2density`, which is based on experimental data given by Schneider et al. [86].
This function is based on a different Hounsfield Unit definition

$$HU_{kWave} = 1000 \frac{\mu}{\mu_{water}} \tag{4.10}$$

but since $\mu_{air}$ in 4.9 is negligibly small it can easily converted using

$$HU_{kWave} = HU + 1000. \tag{4.11}$$

This resulted in a heterogeneous distribution in density and speed of sound for bone, brain and scalp tissue (see table 4.3); the low HU spots described in the previous section were filled homogeneously with the parameters for water, blood and bone marrow found in table 4.4, which also includes other types of human tissue and material found in the literature which required for the simulation.

Table 4.3: Density and the longitudinal speed of sound (mean and interval) calculated using the `hounsfield2density` function when applied to the Visible Human Project®.

| Material | $c_0$ [m/s] | $\rho$ [kg/m$^3$] |
|---|---|---|
| **Skin** | 1507 [1361-1702] | 997 [866-1171] |
| **Skull bone** | 1896 [1702-2472] | 1344 [1171-1859] |
| **Brain** | 1544 [1361-1702] | 1030 [866-1171] |

When comparing the values in table 4.3 to table 4.4 a good match in the values for the brain tissue can be observed, and also the values for the scalp seem to be a good fit assuming to be a combination of skin, connective tissue and fat. Only the values used for bone are considerably lower than the typical values found in other studies. It would be normal to assume that the bone density of the skull decreases with age, but according to Obert et al. and Lillie et al. [57, 25] this is not the case in males; only a decrease in female patients could be stated. The patient considered in terms on this study is a male, the low density values were therefore assumed to be caused by the variance between the different individuals.

Unfortunately, not all of the layers mentioned in chapter 4 were also assignable with all of the non-linearity parameters. Either the resolution of the CT was not high enough to be able to distinguish them spatially or the parameters were not available in the literature. The five layers of the scalp were combined into one, all of the bone layers values were assigned by density and also the meninges were neglected. Therefore only three different distinctions for these parameters were made - skin, skull and brain.

The non-linearity parameter $BonA$ for most soft tissue is between 5-11 [13] while solids have a negligible ability to generate non-linearities. The power law exponent $y$ explained in equation (4.1) was chosen to be 1.2 as in [81]. This is due to the limitation in k-wave that the power law exponent can only be specified for the whole volume and not independently for specific regions. In bone almost a linearity of absorption - as discussed in section 4.1 - was assumed for the frequency range at use, for soft tissue a higher value should be assumed - 1.2 seemed to be a good compromise. To increase the accuracy the absorption power law prefactor $\alpha_0$ was calculated again by fitting it with $y = 1.2$ on the range of $0.4 - 3$ MHz. If no power law exponent $y$ was given, a value of 1 is assumed for this fitting process.

Table 4.4: Materials and their acoustic properties found in literature.

| Material | $c_0$[1] [m/s] | $\rho$ [kg/m$^3$] | $\alpha_0$ $[\frac{\text{dB}}{\text{MHz}^y\text{cm}}]$ | y | $\alpha_0, (fitted)$[2] $[\frac{\text{dB}}{\text{MHz}^{1.2}\text{cm}}]$ | $B/A$ |
|---|---|---|---|---|---|---|
| Soft tissue [52] | 1500 | 1000 | 0.43 | - | 0.37 | - |
| Skin [2] | 1590 | 1065 | 1.79 [80] | 0.87 [80] | 1.38 | 7.9 [21] |
| Connective tissue [21] | 1613 | 1120 | 1.57 | - | 1.34 | - |
| Muscle [21] | 1547 | 1050 | 1.09 | - | 0.93 | 7.5 [51] |
| Fat [2] | 1450 | 950 | 0.6 | 1 | 0.51 | 10 |
| Skull bone [52] | 2900 | 1800 | 14.77 | 0.93 | 11.91 | - |
| Brain [2], [80] | 1550 | 1030 | 0.8 | 1.35 | 0.9 | 6.9 |
| Blood [2], [21] | 1584 | 1060 | 0.15 | 1.21 | 0.15 | 6.1 |
| Bone marrow[3] | 1680 | 1150 | 8 | 1.2 | 8 | 6 |
| Water [2], [47] | 1482 | 998 | 2.17e-3 | 2 | 4.24e-3 | 5.2 |
| Degassed water [9] | - | - | - | - | - | 4.8 |
| Air | 343 | 1.2 | 1.62 | - | - | - |
| Steel | 5750 | 8030 | - | - | - | - |
| PVC | 2400 | 1380 | - | - | - | - |

[1] longitudinal speed of sound
[2] $\alpha_0$ with their respective $y$ is fitted to $\alpha = \alpha_0 f^{1.2}$
[3] no data available, but assumed as a mix of fat and bone

## Bone Density and Attenuation Models

As the table 4.3 shows the range of density and speed of sound for bone is considerably wider than for the present soft tissues but the attenuation would be still assumed homogenous as a single value over the whole interval. This is especially important since bone should have the most influence on the total attenuation due to its high acoustic impedance.

The differences between using the heterogeneous values and assuming a homogeneous skull can be quite high, differences of up to 50 % in pressure have been observed [42]. If this approximation has to be made, it is best to use the values of cortical bone and not cancellous bone or the average of the skull for the best result [15].

To test the influence of the bone three different attenuation models were implemented. The following paragraphs discusses the difference between them in more detail.

### Homogeneous Attenuation

This represents the simplest approach. The density and speed of sound were generated by `hounsfield2density`, the absorption power law prefactor value $\alpha_0 = 11.91$ $\frac{\mathrm{dB}}{\mathrm{MHz}^{1.2}\mathrm{cm}}$ according to [52] was assumed as homogenous over the whole density interval.

### Heterogeneous Attenuation according to McDannold et al. [61]

The approaches by McDannold et al. [61] and Pichardo et al. [78] try to map a different attenuation and speed of sound values to each density value on the interval according to an interpolation of experimental data.

For the conversion curve the density values had to be calculated differently. A linear relationship between the Hounsfield units and density was assumed, with HU = -1000 and HU = 57 representing air and soft tissue. Assuming a density of 1.2 kg/m$^3$ and 1030 kg/m$^3$ this resulted in a linear equation of

$$\rho = 0.97\,HU + 975.2. \tag{4.12}$$

The calculated bone density was with a mean of 1460 [1203-2216] kg/m$^3$ higher than the with `hounsfield2density` calculated values in table 4.3. Afterwards the polynomials provided were used to apply the conversions: the sound speed was applied without any further steps, but the attenuation mapping had to be adapted. The curve was determined by using a 660 kHz applicator and was converted to a 1 MHz curve by using the the power law component of 0.93 specified in Mohammadi et al. [52] in accordance to A.3. Afterwards the curve was fitted to a power law exponent of 1.2 on the range of $0.4 - 3$ MHz as well as all the other attenuation parameters. The conversion curves are shown in figure 4.4.

### Heterogeneous Attenuation according to Pichardo et al. [78]

In Pichardo et al. [78] the density values are calculated with a linear correlation of

$$\rho = HU + 1000, \tag{4.13}$$

with the assumptions of an air density of 0 kg/m$^3$ (HU = -1000) and a water density of 1000 kg/m$^3$ (HU = 0). With an average density value of 1502 kg/m$^3$ [1235-2279 kg/m$^3$], the density values also differed here from the ones calculated in table 4.3.

The attenuation coefficient and speed of sound mapping was carried out for several different frequencies, but only the attenuation values at 1 MHz can be used by k-wave as an input. To generate the conversion curve for the speed of sound as before, a 2D interpolation was applied. The attenuation values were interpolated by using a spline interpolation in the dimension of the density, and the $\alpha_0 f^{1.2}$ in the frequency dimension. The resulting values are depicted in figure 4.4.

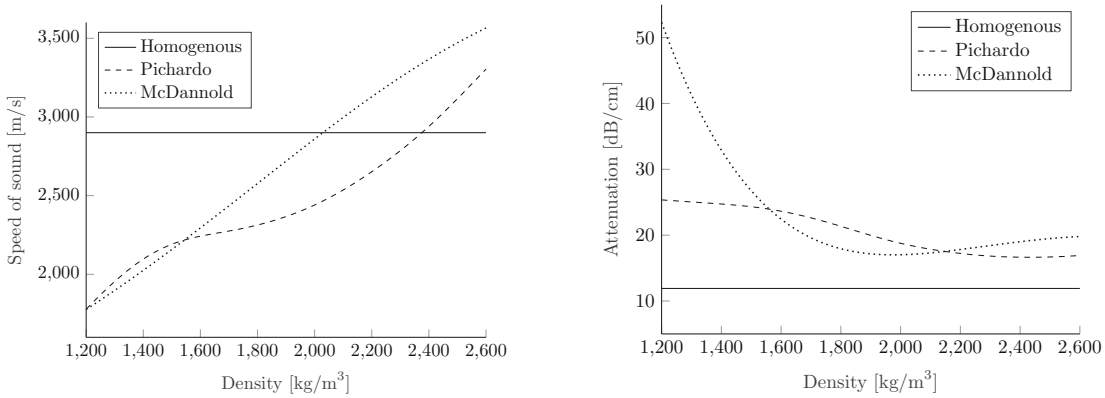


(a) Speed of sound (b) Attenuation

Figure 4.4: Comparison of the speed of sound (a) and attenuation power law prefactor $\alpha_0$ (b) at 1 MHz suggested in [52], [78] and [61].

### Limitations

The density values used in this simulation are in the lower half of the spectrum and atypical. It was decided not to correct the values, and therefore due to the big differences in the attenuation values also different results between the models are expected. Testing the used models on more specimens would be suggested.

From the observations above the power law exponent $y$ presented in (4.1) should be dependent on the density when a heterogeneous material like bone is used and therefore be changed to

$$\alpha = \alpha_0(\rho)\,\omega^{y(\rho)}, \tag{4.14}$$

but since the the simulation uses a single power law coefficient for the whole domain, the heterogeneity is calculated with

$$\alpha = \alpha_0(\rho)\,\omega^{1.2}. \tag{4.15}$$

One has to keep in mind that there could be a difference between 'absorption' and 'attenuation' values. As discussed in 4.2, the use depends on the resolution at hand, and if the exact one is not used, deviations may be possible. The CT of the observed individual is with a voxel size of 0.5 mm on the rough side, a differentiation between the trabecular bone and cortical bone is only recognizable through the low density, the finer structure is not identifiable. The attenuation and not the absorption coefficient has therefore been chosen.
The downside of using the attenuation coefficient is that the resolution at which the coefficient is measured should match the one of the CT. Is this not the case, the additional or removed structures may induce scattering and alter the result.

# 5 Applicators Design

In this chapter the model applicators are presented and afterwards their implementation in MATLAB is discussed.

## 5.1 Model Applicators

The following section tries to gather the information of the different applicators available regarding their focal zone parameters. The dimensions obtained then serve as a template for the applicators used in the simulation.

### EH Applicator

The electrohydraulic applicators are based on the orthogold100 by MTS medical, more precisely on the OP155 (parabolic) and the OE50 (ellipsoid) handpiece. In the data-sheet only the focal position and not the size of the focal zone can be determined [87]; in Porst et al. [32] the focal zone is described as an ellipsoid with a width of $6.9 - 7.9$ mm and a length of $64.6 - 82.3$ mm for the OP155, the OE50 should have a width of $4.7 - 6.7$ mm and a length of $14.3 - 31.3$ mm, depending on the energy settings used. In this setup it is not specified on what measurement the size of the focal zone is based on; the manufacturer describes the focus parabolic reflector as especially 'soft and wide', while the ellipsoidal reflector is applied for a more focussed therapy. The focus length can be estimated to 45 mm and 30 mm respectively.

### EM Applicator

The model for the electromagnetic applicator is the Storz Medical DUOLITH SD1 with the 'Sepia' handpiece. Two different values for the focal zone can be found, a size of $5 \times 5 \times 30$ mm in the data-sheet and a size of $2.8 \times 2.8 \times 34$ mm at 0.55 mJ/mm$^2$ in [32]. It is not specified to which criterion the focal zone was determined, therefore those measurements are assumed to be the -6 dB zone; the focal length is specified as 50 mm.

## PE Applicator

The piezoelectric applicator is modelled on the *Swiss PiezoClast* [84], which has a focal length of 40 mm. The -6 dB zone is specified as an ellipsoid with a width of $1.2-2.8$ mm and a length of $5.0-14.1$ mm, depending on the amount of energy used.

In [89, 70] it is hypothesized that in a spherical applicator (therefore only piezoelectric) the pressure level depends on the focussing angle. Therefore the variable

$$F_{\#} = \frac{F}{2\,a_0} \tag{5.1}$$

was introduced, which represents the focussing strength - with a low number being very focussed and a high number represents a weak focus with a wider focal zone. $F$ is the radius of curvature of the applicator and $a_0$ the opening radius. Applicators with a similar $F_{\#}$ have a similar shape of the focal zone.
Non-linearities are created either over a long distance at a lower pressure or at a shorter distance with higher pressure (see equation (1.20)). This makes applicators with a long focal zone at the same focus length, or with this description, a higher $F_{\#}$, favourable for the generation in shock waves at the same input energy. To compare this effect two piezoelectric applicators with a different $F_{\#}$ are created, one with $F_{\#} = 0.68$ (based on the PiezoClast applicator mentioned above) and $F_{\#} = 0.87$.

According to [69] a piezoelectric applicator with $F_{\#} = 1$ needs to have a radius of above 19 cm to be able to form a fully developed shock wave through the skull with a frequency of 1.2 MHz and below while keeping a the maximal possible energy output of a piezoelectric-element ($40\,\mathrm{W/cm^2}$). Due to the 45 mm focal length restriction it is not possible to adapt the PE applicator to this suggested size. Generating a fully developed shock wave through the bone with the presented settings would therefore probably not be possible, on the other hand the definition of a shock in the presented paper seems to be rather strict and could probably not be achieved with the resolution used in this simulation.

## Applicator Comparison

In figure 5.1 a comparison of the listed focal zone sizes can be found; if multiple values are specified, the average is taken. As mentioned before, the focal size is to be interpreted as qualitative information simply due to the lack of data. A summary

with the aperture and focal length as reference is listed in table 5.1.

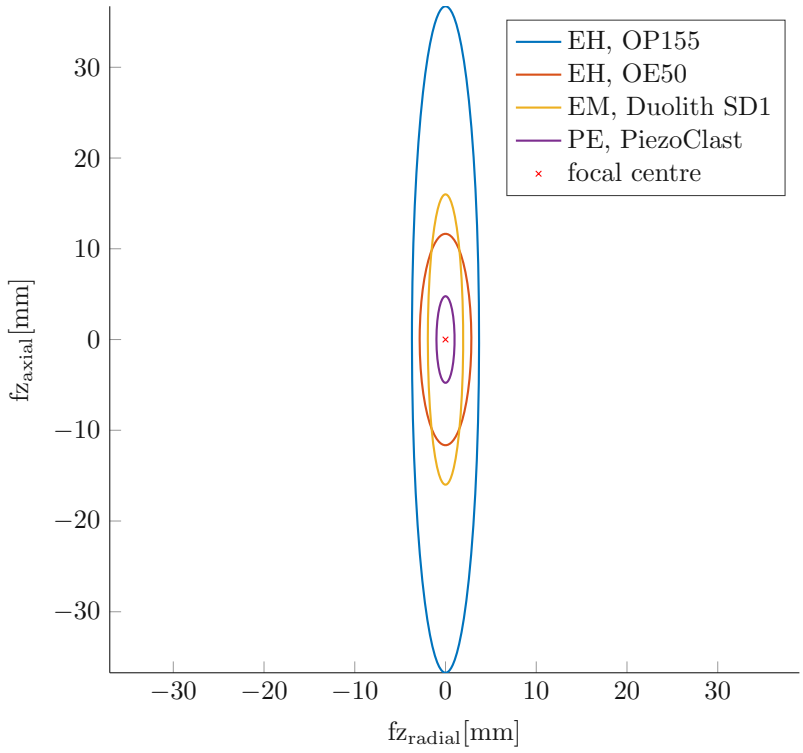


Figure 5.1: Comparison of the longitudinal sections of the -6 dB pressure focal zones provided by the manufacturers for the model applicators; $fz_{radial}$ shows the width of the focal zone in the radial direction, $fz_{axial}$ shows the length in the axial around the central focus point.

Table 5.1: Comparison of the model applicators focal zone $fz$, with their aperture and focal length as reference.

| Material | $fz$ Length [mm] | $fz$ Width [mm] | Focal Length [mm] | Aperture [mm] |
|---|---|---|---|---|
| MTS OE50 | 23.3 | 5.7 | ~ 30 | ~ 45 |
| MTS OP155 | 73.45 | 7.4 | ~ 45 | ~ 50 |
| DUOLITH SD1 'Sepia' | 32 | 3.9 | 50 | ~ 45 |
| PiezoClast | 9.55 | 2 | 45 | 100 |

The different applicators can therefore be categorized in the highly focussed piezoelectric applicators, the moderately focussed applicators like the EM and the ellipsoidal EH applicator, and the very wide focussing paraboloid EH reflector.

### Limitations

Unfortunately, the values provided by the manufacturers are often not informative enough. Most of the time only the energy flux density is given, the maximum pressure is hardly ever specified. The position of the focal lobe depends on the the energy setting; furthermore, it may be hard to find a closer specification on how the focal distance and size of the focal zone is defined. The parameters are measured in a controlled environment, often submerged in a water bath and not in a simulated application situation - but the zones may vary significantly due to the inhomogeneities in the human body [65].
It's partly due to a number of different factors, but above all it is due to the insufficient description of the individual products that it is hard to reconstruct and compare the applicators.

## 5.2 Applicators Design and Implementation

Applicators in studies are often defined as a 2D source [23]. To reproduce the characteristics of each applicator it was decided to remodel the three different applicator types in 3D.

Five applicators are used in this comparison, which are based on the existing shock wave applicators presented in section 5.1, but were adapted to a focal length[1] of 45 mm. The PE applicators were calculated due to their simple geometry, as well as the ellipsoidal EH applicator; the other two paraboloid reflectors were optimized at 10 MPa using a voxel resolution of 0.35 mm; at this pressure level the non-linearities should be rather small, and the geometrical focus close to the actual focus. At higher pressure levels the focal zone will shift further away, partly to the non-linearities and partly to the fact that in the reflectors the angle of reflection is larger than the incident angle. This gap increases when pressure and incident angles get higher [8].
To avoid overlapping source points a single pixel thick layer was used as a source, which prevents smoothing of the sound wave [23]. All of the resulting geometrical details of each applicator used in this simulation can be found in the Appendix A.5.

[1]Distance from the applicators surface to the point with the highest pressure in the focal zone

## Ray Tracing

For most of the applicators the data needed to reconstruct them is either incomplete or it has to be adapted according to the focal length restriction. A linear increase in size is often not possible due to the complexity in the geometry of the reflector; the focus zone would shift not as expected, or its shape would distort or increase disproportionately. To avoid these side effects, two ray tracing programmes were created.

### Analytical Approach

The analytical ray tracing is only used for the electromagnetic applicator where the initial shock wave can be approximated with a cylindrical and not a spherical spreading and the reflector is based on a differentiable function. The goal is to find the most fitting parabola in the form $y = \frac{x^n}{p} + b$. The parabola is forced through two points, one at the aperture of the reflector, and the other one at the base of the coil. The equation system is still underdetermined, which forces one variable to be chosen. Since the exponent $n$ is the hardest to calculate the ray tracing is then completed for a range of $n$ to find its best fit.
As only rays radial to the coil core are considered, with these restrictions an exact intersection of the shock rays and the reflector can be calculated. Using the first derivative at these points of the parabola the incident angles can be determined and also the reflected angles can be calculated. The incident points of the reflected rays and the main axis are then used to compare to the focal zone provided by the manufacturer assuming a Gaussian distribution.

### Numerical Approach

The numerical approach is more universal than the analytical approach, the position and the angle of the source-rays can be chosen freely. The intersection of the pressure rays and the parabola are calculated by subtracting the line equation $y = m*x+c$ of the pressure ray from the parabola $y = \frac{x^n}{p} + b$ and determining the point where the sign changes. At this point the tangent of the parabola is determined numerically with the first derivation $f'(x) = \frac{f(x+h)-f(x-h)}{2\,h}$ and the reflected ray can be calculated assuming that the angle on the incident and the reflected ray are the same. As before only the variable $n$ is changed to find the best fit of the focal zone.

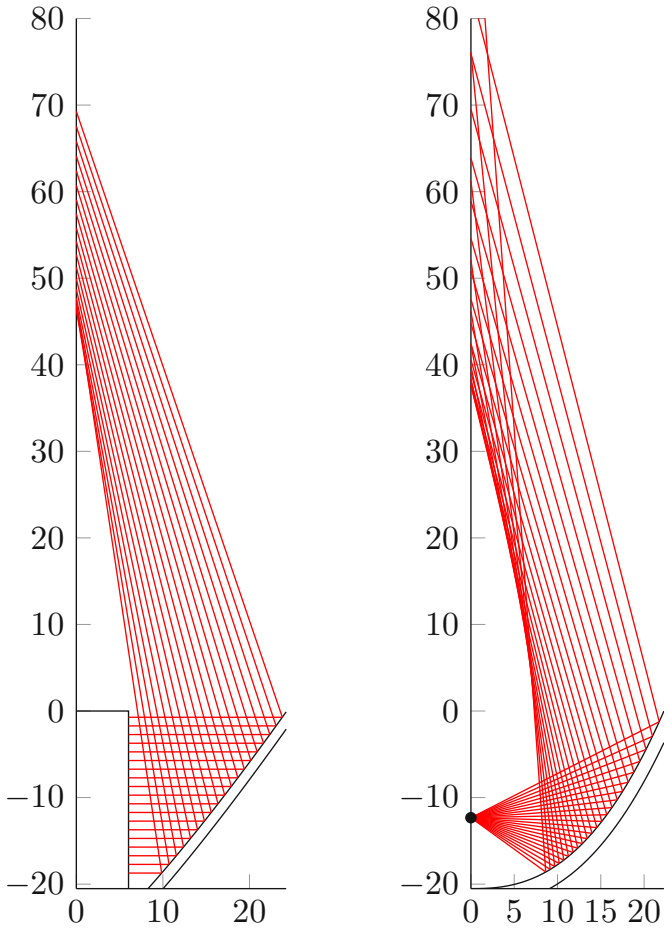


(a) analytical raytracing (b) numerical raytracing

Figure 5.2: The analytical (a) and the numerical (b) ray-tracing with a electromagnetic applicator and a electrohydraulic applicator. The distribution of the intersections of the rays with the y-axis are used to compare the focal zones with the model applicators, the number of rays for this process is largely increased.

### Limitations

The difference in the incident and reflected angle for higher pressures as pointed out before was not included in these calculations, neither could non-linearities be implemented in this ray tracing script. While this tool is not able to calculate a complete accurate positioning, it was very helpful to adjust the focal centre and the size of the focal zone.

## EH Applicator

Both of the used EH applicators are based on the shock wave devices produced by MTS Medical UG [58]. There are two different types of reflectors available for this type of shock wave generation. The first applicator type features a reflector shaped by a parabola, the second uses the natural property of a ellipsoid to have two focal points: if the source is positioned in one of them, the signal is reflected to the second focal point.

The ellipsoidal reflector was composed out of two ellipsoids which are used to create a shell and after truncating them at the determined size, the source sphere was placed in one of the determined foci.
The paraboloid reflector was implemented in MATLAB by using the determined parabola and rotating it around the central axis.
As a source a small sphere with a radius of 0.5 mm is used, which floats at the point of generation; the steel electrodes were not included in the simulation - the holes in the reflector that were intended for this purpose were therefore filled with PVC instead of steel to reduce the reflection at this section to stay closer to the original applicator.

## EM Applicator

The EM applicator is based on the Storz Duolith F-SW handpiece 'SEPIA' [82], the reconstruction is based on geometric measurements and the information provided in the operation manual [83]. The determination of the exact parabola function used in the reflector turned out to be non-trivial since already small deviations have a significant impact on the focus position. Using the implemented ray-tracing with the analytical approach the focal distance was adapted to the targeted 45 mm.

The reflector based on the parabola was generated similarly to the EH applicator using the rotational symmetry. While the material composition of the coil at the core could not be determined, it showed to have no significant influence for the simulation if either PVC or steel was used.
Lamb waves, which are oscillations generated by the membrane being fixed to the applicator, were neglected in this simulation [23].

### PE Applicator

Due to the flexibility of the piezoelectric elements in size and in positioning, the easiest and most controlled way to build a reflector is by arranging them on a sphere [85, 84]. The size and position of the focal zone can be determined by the radius of the sphere and the angle of the circular segment. The applicators were therefore created by removing a circular indent from a volume of metal and paving the surface with source-voxels. The size of the single piezoelectric elements, the arranging and the spacing due to the restrictions in the production were neglected.

## 5.3 Input Signal

The input signal is the signal created at the source of the respective applicator. Due to the difference in the physical generation of it, no universal input signal can be chosen, it has to be customized manually for each of the technologies. This results in three different input signals which had to be elaborated. For the EH and the EM applicator pressure measurements, created at the Laurenz-Böhler Institute (LBI), recorded at different positions served as a base for the reconstruction, while for the PE applicator measurements found in several papers and data sheets of manufacturers were used.

First of all, the type of input signal had to be chosen: k-wave provides the option to use a velocity and a pressure source[2]. Both are calculated at the staggered grid points and additionally to achieve a symmetry in the reflector the source voxel had to be adjusted manually. A distance of one or more voxel had to be maintained from the closest reflector material to prevent that the source is not defined inside the metal; only due to this implementation any unnecessary transmission interface can be avoided. After testing only the pressure source showed to be symmetric enough for further use.

The input signals are non-periodic and show sharp gradients which results in high frequency components if translated to the frequency space. The grid size limits the frequency range and as a result, the Fourier series is truncated and a non-sufficient amount of Fourier coefficients are left to describe the signal. The produced signal can show oscillations, especially close to steep jumps in its gradient. This phenomenon is

[2]The use of a pressure source can be interpreted as an injection of mass in free space.

called *Gibbs-Phenomenon*, and is especially visible in the case of an electrohydraulic simulation due to its sharp gradients [49].
To reduce the appearance of these oscillations the input signals were smoothed in the frequency domain with a Kaiser Window, applying the included `filterTimeSeries`, or while in the time domain a cosine function was applied [81].

The best way to avoid these problems is by choosing an input function which resembles the original input while keeping the frequency range as small as possible - which is unfortunately hard to achieve manually. In the closer selection there was a truncated and dampened sinus

$$f_{in}(t) = sin(2\,\pi\,f\,t)\,e^{d\,f\,t} \tag{5.2}$$

and a combination of different Gaussian curves

$$f_{in}(t) = \sum_i a_i\; e^{-\frac{1}{2}\left(\frac{x-b_i}{c_i}\right)^2}. \tag{5.3}$$

Eventually the Gaussian combination was picked due to the ease of use and manipulation, and the rare occurrence of oscillations described by the Gibbs phenomenon due to the naturally smooth transitions of the signal.

The pressure amplitude had to be adapted with the voxel size, though. Changing the resolution also changes the amount of source points and therefore the pressure generated. Another factor, which had to be counteracted, too, is the geometrical decay. While a 1D simulation shows no decay (except the absorption), in 2D and 3D there is a decay due to the cylindrical and spherical spreading. As a result the initial pressure was not only adapted to the number of source points, but also to the geometrical spreading with $\frac{1}{sqrt(radius)}$ for the cylindrical waveform in 2D and $\frac{1}{radius}$ for the spherical wavefront in 3D for an easy switch between a lower and a higher resolution [49].

As mentioned above in section 5.2, all the applicators were adapted to the same focal distance, but also the output signal had to be made comparable as well. Since the characteristic signal shape has to be maintained, either their energy flux density or the pressure has to be matched.
Matching the signals of the different applicators in one attribute results in a large deviation in the other. The exact effects of the different parameters on the human

tissue are mostly unknown, but in stone comminution the average positive pressure showed to have the biggest correlation, while the energy showed to have less impact[3] [63]. Adapting for the average pressure with varying signals was hard to achieve, therefore it was decided to match all the signals to the same maximal pressure levels instead.

The target value of the maximal pressure was then chosen to be 20 MPa, which is 5 MPa less than the value suggested in Beisteiner et al. [74] for brain stimulation. A higher pressure value would show more non-linearities, but would call for an even higher resolution due to the grid size restrictions explained in section 6.1. Regarding the safety of the use of shock waves in the brain, in Beisteiner et al. [74] a threshold of 0.25 $mJ/mm^2$ at 4 Hz with a maximal peak pressure of 25 MPa is suggested, but below 40 MPa no lesions have been observed.
The exact settings for the following applicators are described in the appendix A.6.

### EH Applicator

The EH signal is generated as described in section 2.1 by the rapid expansion of a plasma, followed by the collapse of the thereby generated bubble. To implement this steep gradient in the pressure rise a piecewise function was used. The first rise was generated by a Gaussian function with a very small standard deviation, at the the maximum it was interrupted and continued with a Gaussian with a bigger standard deviation. The measurements taken at the LBI, as well as in Coleman et al. [7] served as a model for the reconstruction.

### EM Applicator

Measurements of the EM applicator outside the focal region and close to the membrane describe the signal as a sinusoidal shape [7, 4]. This could be confirmed with measurements taken at the LBI. With a combination of three Gaussian curves an input signal similar to a damped sinus was generated. The advantage of using Gaussian curves is that almost no filtering is needed for a smooth transition.

### PE Applicator

The signal of the PE applicator was assumed similarly to the EM source, but the tensile components were more pronounced. Depending on the physical dampening

[3]It was hypothesised is that the quasi static tensile failure strength of the stone has to be exceeded.

the 'trail' of smaller oscillations can be quite prominent but were not taken into account in this simulation. The signal is based on the measurements provided in Sternecker et al. [46] and several other sources [64, 73, 72, 79, 7].

### Input Signal Comparison

In figure 5.3 the input signals are depicted schematically. The input signals are easily distinguishable and show different properties. The implemented piezoelectric signal shows a prominent tensile peak before and after the main compressive wave. The EM input signal also shows a tensile peak before and after, but it is not as distinct as the PE signal and is asymmetric. The EH signal just consists of a steep rising and slow falling compressive component with no implemented tensile parts.

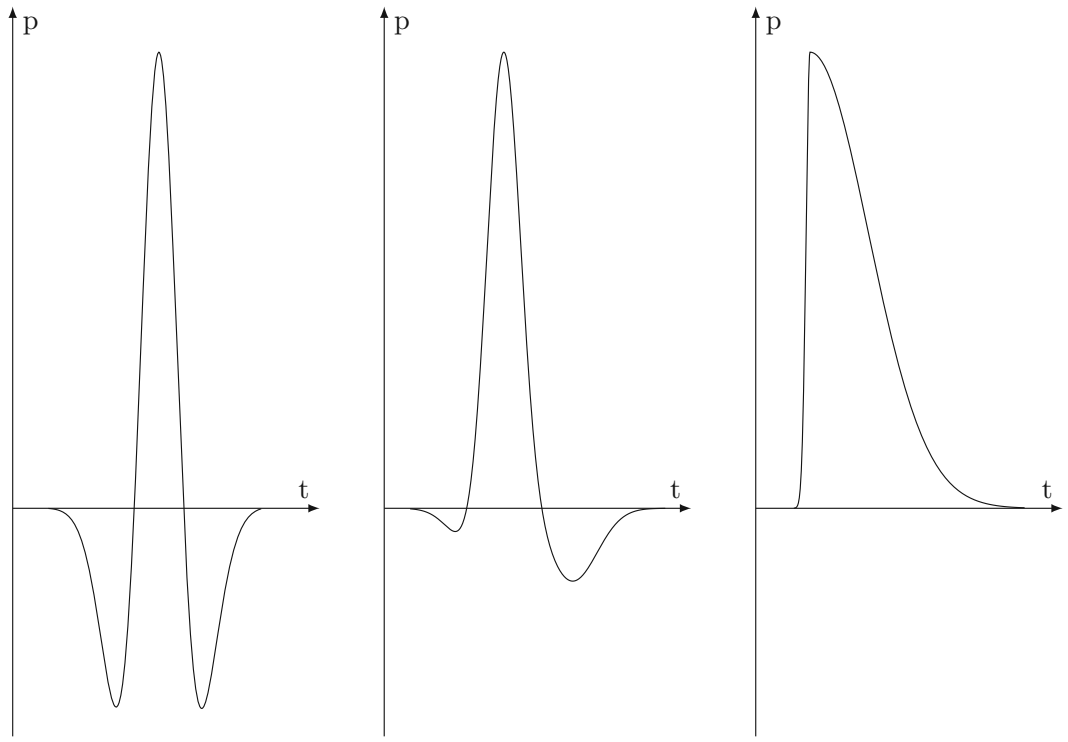


(a) PE (b) EM (c) EH

Figure 5.3: The schematic input signals at the source voxels for the different applicator technologies, the settings used are found in the appendix A.6.

The implemented signals may not correspond to the reality at the source point, the energy in the tensile and compressive part should sum up to zero in a case with no dissipation and no net particle movement; but the used input signals result in a

good agreement in the vicinity to the focal point. Close up measurements are rarely available and only generable by partly dismantling the head of the applicator, which is usually not feasible.

Applying a Fourier analysis on the presented input signals results in the curves visible in figure 5.4. It is hard to determine a dominant frequency, except for the PE signal which shows a clear frequency bump at around 600 kHz. In general the assumption is made that the EM applicator shows the lowest frequency composition, followed by the PE applicator. The EH signal is the one with the highest frequency components, the pre-filtering of the signal to prepare it for the grid is tougher on it than on the other two signals, which show a clear decay before the 4 MHz threshold.

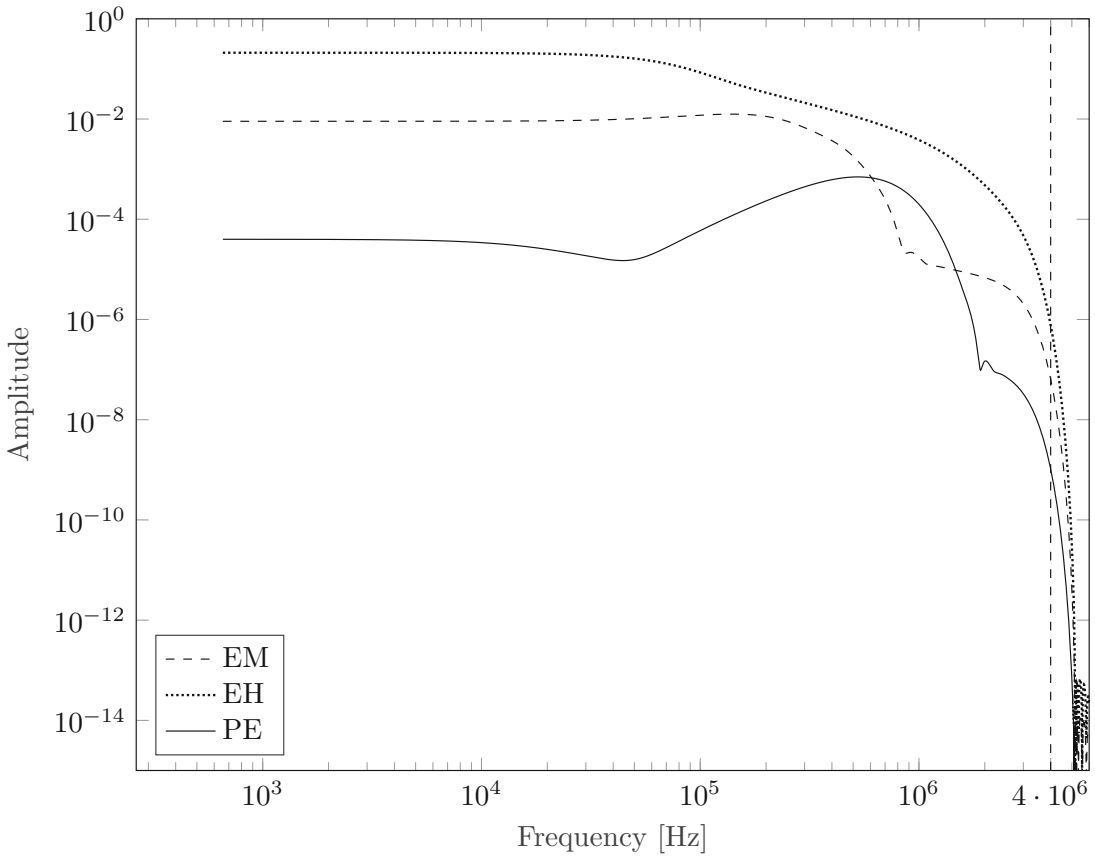


Figure 5.4: Fourier analysis for the input pressure signals of the simulations with the cut-off frequency of 4MHz.

The Fourier analysis can be used as a prediction for the behaviour of the simulation. The high pressures used should shift the spectral weight to the right - which is possible for the PE and the EM, as the grid supports a higher frequency; the EH

signal on the other hand is already on its limit, a shift to a higher frequency spectrum can not properly be displayed.

## 5.4 Phase Correction

Phase correction is a method which can be used in some piezoelectric applicators to synchronize the single piezoelectric elements according to the obstacle properties, in this case the skull, that all of the elements signals arrive at the same time. This should improve the signal form, energy and pressure at the focal point. As this technique requires a CT and needs to be recalculated for every change in position, at the moment it is only feasible in stationary devices (eg. ExAblate [76]).
By creating a simulation with a CT of the patient's skull - where the source is applied in the target region of the brain, and the piezoelectric elements act as sensors - the phase difference introduced by the irregular shape of the skull can be simulated. Keeping in mind these facts, the signal of each element is adapted accordingly[4] [43, 81, 39]. In Sun et al. [38] an increase of pressure by 95 % was possible to achieve applying this technique, but even in the corrected attempt the signal amplitude was still only 9 % of the pressure amplitude in an empty water bath.

In this model the source voxels were not divided into single piezoelectric elements, but the phase correction was implemented for each voxel separately. As a result, the simulation's outcome should be better than a real case scenario, since one PE element would consist of multiple source voxels. The implementation was done by creating a simulation where all the source voxels and the sensor voxels were swapped while the CT is present. The recorded signals at the applicator were then compared to generate a time shift for each voxel by using the maximal pressure peak as a reference. In other words, for each source voxel a time delay is calculated based on what medium is between the source and the focal centre.
This process was only calculated for the PE applicator with $F_{\#} = 0.87$, whereas the source signal and its input amplitude was left unaltered.

[4] Only works for applicators where each element can be controlled separately.

# 6 Shock Wave Simulation

The shock wave simulation was carried out by using the open source k-Wave toolbox[1].

## 6.1 k-Wave Toolbox for Matlab

k-Wave is a MATLAB toolbox developed by Bradley Treeby and Ben Cox (University College London), while the C++ version of the simulation was contributed by Jiri Jaros (Brno University of Technology). Its focus lies on the propagation of acoustic waves in heterogeneous media while taking account cumulative non-linear effects to the second order. This makes it especially useful for simulations of ultrasound waves for the biomedical use.
The toolbox is based on the k-space pseudo-spectral method (also called k-space method), which is based on the Fast Fourier Transformation (FFT). This makes it possible to use a much coarser grid than a classical finite difference and finite element simulation where at least six to ten grid points per element have to be used for a reliable result. In this case, according to the Nyquist theorem, only two grid points have to be used. This reduces the amount of grid points in a 3D simulation by at least a factor of $3^3$, which even allows this type of simulation to be calculated on a moderately strong desktop PC without disregarding its accuracy.

### Simulation Grid

The simulation is based on a staggered grid, which means that the velocity and pressure are spatially stored slightly off place than the remaining variables. While this is an option to reduce discretization errors, it can be more difficult to handle simulations which require symmetry.
As mentioned before, the grid size of the simulation depends on the maximal calculable frequency which is to be achieved [10]. This is due to the Nyquist-Shannon sampling theorem, which states that at least two grid points per wavelength (PPW $= \lambda/\Delta x$) are required. Since the wavelength $\lambda_i$ in a material can be calculated using

[1] http://www.k-wave.org/

its speed of sound $c_i$ and the frequency of the wave $f$ with

$$\lambda = \frac{c_i}{f}, \tag{6.1}$$

the simulations frequency is limited by the the grid size dx and the material with the lowest speed of sound $c_{min}$:

$$f_{max} = \frac{c_{min}}{2\,\Delta \mathrm{x}}. \tag{6.2}$$

To provide a reliable comparison all the simulations have to be calculated with the same grid size dx to rule out an advantage for smaller reflectors which could be calculated with a higher resolution as the non-linearities could become more visible. As described in section 1.4 the non-linearities are created by higher frequency harmonics. The grid therefore has not only to be fine enough to cover the input signal, but also the high frequency components which are generated during the wave propagation.

Another prerequisite for the grid size is the smallest prime factor of the resolution - the smaller it is, the faster the simulation is running. It was therefore tried to use only grid sizes with prime factors of 2 and 3. This is especially important with the use of a computational centre since every simulation has a limited runtime. Using a a GTX 1070 with grid size of $512 \times 256 \times 256$, with the smallest prime factors of $2 \times 2 \times 2$, the simulation time accumulates to around 38 minutes, a switch to the slightly smaller domain of $511 \times 255 \times 255$ with the smallest prime factors of $73 \times 17 \times 17$ increases the simulation time to 112 minutes.

Limited by the size of the reflectors and the computational power, a domain size of $1024 \times 648 \times 648$ for the final simulation is chosen with a voxel size of 0.17 mm, which shows a feasible simulation time with its smallest prime factors of $2 \times 3 \times 3$.

According to Robertson et. al [43] there are several numerical errors which require certain settings for reliable numerical results:

- **medium discontinuity**
  At medium interfaces reflection occur; to depict them properly and achieve an energy transmission error of less than 10% (corresponding to a 95% reconstruction of pressure) between soft tissue and bone a PPW of at least 4.3 is necessary.

- **staircaising**
  Staircasing is an effect which arises if a continuous geometric model is translated into a Cartesian grid - it will be approximated in a stair-stepped manner. To obtain an error $\leq$10% in the intensity amplitude caused by a medium interface in 2D at least 6 PPW would be needed, while no real relationship between the angle and error should be observed. If the staircasing effect is generated by a double medium interface (soft tissue - bone - soft tissue) even 20 PPW would be required.

Surprisingly, in a convergence model in 3D where all numerical errors are included 6 PPW seem to be sufficient for $\leq$10% intensity error; it is suggested that the staircaising is reduced in 3D geometry [43].
The listed effects mainly influence the pressure amplitude and not the location, latter does not vary more than 50% of the wavelength and is suggested to be solely due to the misregistration of source points [43]. Therefore, for spatial targeting a low resolution approach may be sufficient.

With the mentioned resolution in this simulations only frequencies below 4 MHz fulfil the 2 PPW requirement and are depicted. As visible in figure 5.4, the EH applicators show the highest input frequency are therefore affected the most by this restriction. Due to the low-pass properties of the skull bone, the propagation of higher frequency components is restricted and numerical disturbances are mostly expected in the water bath without the skull present where the non-linearities can evolve without constraints. On the other hand, with the skull as obstacle, the 6 PPW requirement suggested for a medium interface is only fulfilled for a frequency below 1.3 MHz, which is again affecting the EH applicators the most, in this case influencing the signal amplitude instead of causing numerical disturbances. Additionally, the provided CT has a resolution of only 0.5 mm $\times$ 0.5 mm $\times$ 0.5 mm which is interpolated to the grids resolution. Staircasing errors therefore can not be prevented for higher frequencies in the simulation at hand, which may influence the intensity error.

## Perfectly Matched Layer

Due to the periodic nature of the k-space method of k-wave, waves exiting at one side of the domain reappear again at its opposite side. To avoid this a perfectly matched layer (PML) is introduced, which provides sufficient absorption while not reflecting

it back into the medium. Therefore a PML thickness of 10 voxels in every direction is chosen, which is a typical value for 3D [49]. An advantage in the simulation at hand is that the runtime is not long enough to be very susceptible for this type of error.

### Time Step and Stability

A way to control the time step size is by the Courant-Friedrichs-Lewy (CFL) number, which is defined as the distance ratio a wave can travel in one time step:

$$\mathrm{CFL} = \frac{c\,\Delta t}{\Delta x} = \frac{PPW}{PPP}, \tag{6.3}$$

with the speed of sound of the medium $c$, the grid size $\Delta x$ and the time step $\Delta t$. In other words, it is the ratio of the distance the wave can propagate in one time step to the distance between the grid points. Another way to express it would be the relationship of grid points per wavelength (PPW) to temporal points per period (PPP $= 1/(f\Delta t)$) [43]. To provide stability, this ratio should be smaller than one $CFL \leq 1$, since any changes in the grid should be registered by its closest neighbour and not jump between grid points.

The CFL number in this case was set to 0.3. Choosing a higher value was not possible due to another stability reason: To provide the highest accuracy, a reference speed has to be chosen, which should be the speed of sound of the observed medium [49]. If the reference speed is set higher, a phase error can occur which increases with the speed of sound difference of the reference value to the observed medium. The drawback is that the time step has to be decreased, otherwise the phase error may blow up, and with the other used settings a CFL number of more than 0.3 would decrease its stability. A smaller value would probably be preferable, though, because of the strong heterogeneity of the medium, but the wall-time of the server used for the calculation does not allow a longer simulation. Increasing the time-step increases also the simulation duration linearly. A short comparison for the EH applicator with a CFL value of 0.2 was made, but no differences could be observed, though.

One has to keep in mind that the same CFL number in a spectral method will produce a much coarser time step than finite element simulation due to the difference in grid size as discussed in section 6.1, but will still provide a similar accuracy [11].

### Record Probe

To make the simulation as comparable as possible with a real life application, the sensor was adapted to the size of a needle-type hydrophone and the signal was averaged over a circle of voxels with the radius of 0.25 mm. Several recordings were made along the applicators central axis around the focal centre to have as many measurements as possible. Also the minimum and maximum pressure at each point in the medium was recorded. This ensured a comparison of the size and shape of the focal zone.

### Limitations

In a normal application the reflector would be applied manually with a liquid or gel filled stand-off to determine the distance, with air as the surrounding material. In comparison to the organic tissue, air has a low speed of sound of only 343 m/s and would thereby decrease the stability of the simulation. In an ideal case, air should not be present in the shock wave pathway, therefore the setup is reduced to the materials of the reflector and the organic tissue which should be observed, while the rest of the domain is filled with water. Air bubbles, which could be trapped in a real therapy in the ultrasound gel or between the hair, were therefore neglected as well, but can reduce coupling in therapy dramatically.

The k-wave simulation needs to set a reference speed of sound with a heterogeneous medium to reduce a phase error and satisfy its stability conditions. Normally the reference speed is set to the highest speed of sound in the domain, but by this the error in other parts of the domain increases. Unfortunately, this simulation contains a variety of materials with a wide range of speed of sounds: While organic tissue has a speed of sound close to water of around 1500 m/s, the skull bone can have a speed of sound up to 3000 m/s, only to be topped by the reflector made of steel with around 5600 m/s. To ensure the highest precision in the target region, these reference values should match the speed of sound of that region. The time steps $dt$ have to be adapted to comply with the stability criterion. This increases the calculation time, while preserving a low error in the target region, but reducing the accuracy in regions with a big difference in speed of sound to the chosen reference value.

With a high pressure and a medium discontinuity, errors could arise which could

produce high frequencies; these would result from the reflection at the skull, and the steep changes in medium properties could introduce Gibbs phenomena in the pressure field [43].

Another limitation is the power law absorption which was used in the simulation. While being accurate in soft organic tissue, the shear modulus of bone would have to be taken into account. In k-wave a solver that accounts for shear waves is implemented; unfortunately, this version is only available in the MATLAB and not as CUDA or C++. Due to the time restriction on the server a smaller domain size and therefore a lower resolution would be needed, where the non-linearities are no longer properly depictable due to the loss in high frequency components.
The only way to bypass this is to apply the shock waves normal to the bone surface. As shown in Treeby et al. [12] the shear waves are negligible below a critical angle of around 34° to the normal vector of a surface. In another study [77] it was determined that the critical angle depends on the density and structure of the bone, and a critical angle of between 30° to 45° was observed.
While no obvious occurrence of a critical angle is observed, due to the curvature and heterogeneity of the skull and the large area where the shock waves penetrate the bone, it may not be possible to completely avoid the generation of shear waves; running this setup with shear waves included could improve its accuracy - a deviation of 15% in the pressure amplitude, focal volume size and location has been reported [42].

The signals which were used to reconstruct the applicators are recorded with a variety of different sensors. In older studies often PVDF needle sensors were used, which have a slow rise time and moreover underestimate the tensile component. This is due to the low adhesion to water and potential cavitation at the surface can occur - which may even erode the hydrophone [75]. Sensors with optic fibre are now accounted for as state of the art, and while they are not able to measure low pressures precisely [44, 36], they have a smaller area and a better adhesion to water.

## 6.2 Simulation Settings

The MATLAB K-wave tool offers different ways of simulating the domain: One could turn to 2D and 3D, as well to axisymmetric (rotational symmetry) simulations.
Each of the simulation methods mentioned has its advantages and disadvantages.

## 2D Simulation

The 2D simulation is the fastest and easiest way to simulate, but unfortunately the least realistic of the options mentioned. It assumes that the provided layer is repeated at infinitum above and below; a point given in 2D would be an infinite long cylinder in 3D instead of a sphere. The target also receives the signal from the sources in the layers above and below, even after the signal should have ended. This approximation is not sufficient and was therefore only used for testing purposes, a comparison between the different simulation types are demonstrated in figure 6.1.

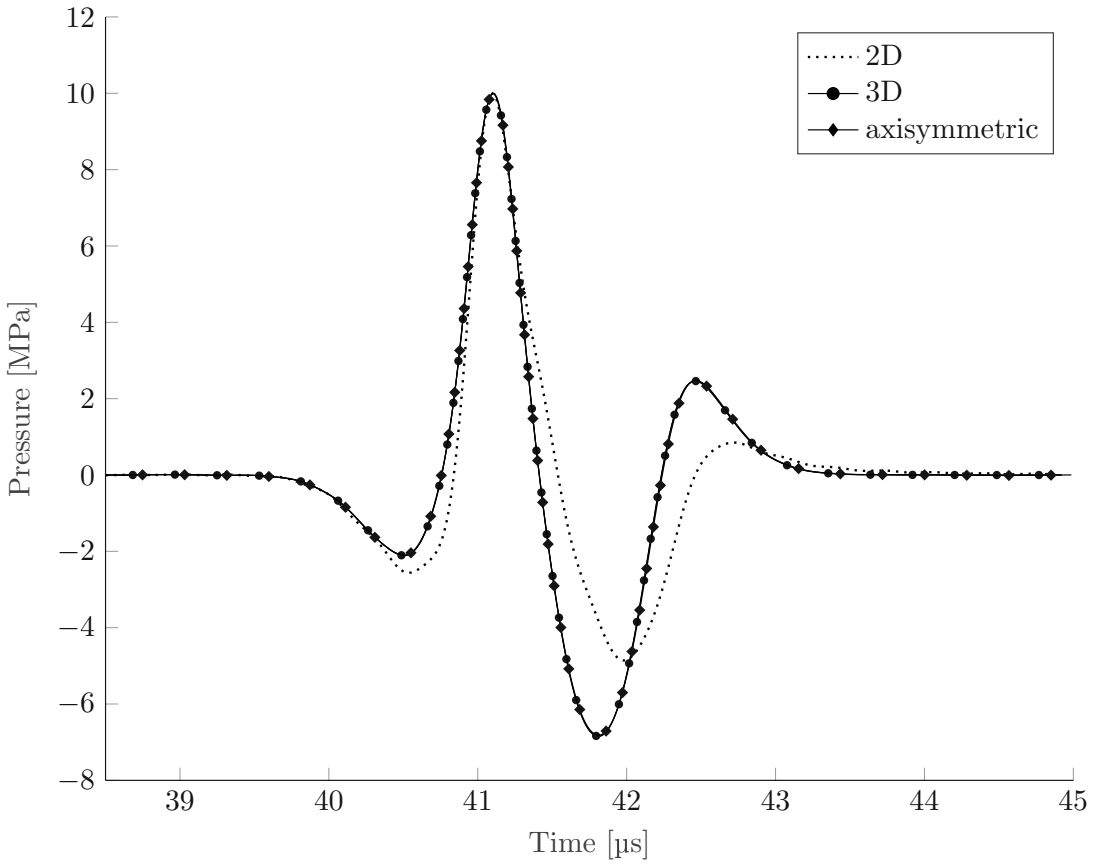


Figure 6.1: A comparison of the different simulation options using the Piezo reflector in a empty water bath with a voxel size of 0.25 mm. The axisymmetric and the 3D simulation are fairly similar, while the differences of the 2D simulation are clearly visible.

## Axisymmetric Simulation

An axisymmetric simulation would be acceptable for the free field simulations; while slower than 2D, it would be still faster than 3D while providing a similar result.

To apply it on the skull, the tissue would need to be simplified in a manner to be axisymmetric, the reflectors used in this simulation could all be adapted easily because of their rotational symmetric nature. Another limitation would be that only a medium with a power law coefficient of 2 is supported, therefore it was decided not to pursue this approach any further.

### 3D Simulation

The 3D simulation provides the highest accuracy, but also at a great computational cost. Every increase in size by the factor $f$ increases the computational effort by $f^3$. While a grid of about $512 \times 256 \times 256$ is perfectly feasible on a GTX 1070 with 8 GB of memory, a simulation in the size of $1024 \times 648 \times 648$ requires a memory of over 60 GB, which can only be handled by expensive hardware accelerators such as the NVIDIA A100 with 80 GB ($\approx$ 12500 \$). Instead of performing the calculation on a GPU, an Intel Server at the Center for High Performance Computing (CHPC) in Utah with 64 GB of RAM was chosen.

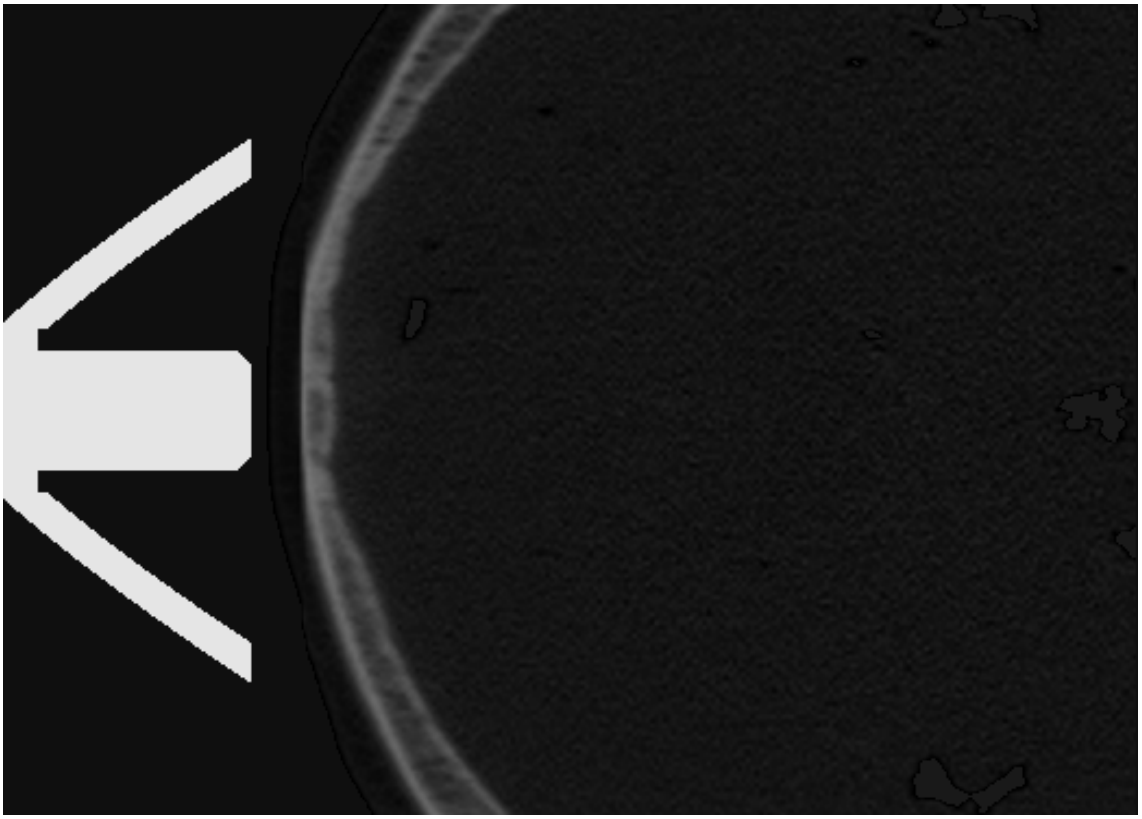

Figure 6.2: Section of the setup with the CT and the EM applicator.

### CHPC - Center for High Performance Computing

To use k-wave on the server an input file has to be created which is then executed by the C++ binary provided by the k-wave tool. This workflow can be carried out in a single file using the SLURM workload manager.
First, the cluster has to be selected, followed by the necessary requirements for a node. All of the clusters have a fixed wall time of 72 h, which means the job gets aborted if the computation exceeds this limit. Therefore, a full node is requested, with at least 64 GB of RAM to be able to process the size of the 3D volume. To be able to prepare the input file and execute the binary, several modules have to be loaded (MATLAB `R2018b, intel, spider fftw, impi, hdf5`, and if GPUs are used also `CUDA`). After that a *.h5* file can be created using MATLAB which is then processed by the mentioned C++ optimized version of k-wave. The average computation time with $1024 \times 648 \times 648$ grid and a CFL $= 0.3$ on a INTEL XEON E5-2670 v2 (10 CPU cores) is about 30 h.

## 6.3 Evaluation Methods

In order to compare the ability to create shock waves through the skull bone the resulting signals were evaluated by using the maximal pressure, the gradient $\frac{\Delta p}{\Delta t}$ between 20 % and 80 % of the maximal pressure of the signal and the resulting PII, but also its frequency.

### Frequency Analysis

A quick estimation of the frequency of the signal can be performed by using the 'zero crossing frequency'. While for a low pressure ultrasound device using a sine wave it is matching with the actual frequency, for non-linear waves it is just a very rudimental approximation. Due to the shift of frequencies into the higher harmonics as described in section 1.4, a fast Fourier transformation (FFT) has to be applied to get the actual frequency values.

For the FFT the signals are cropped only to the main shock wave to avoid influences by the later recorded scattered pressure waves. Due to the nature of the shock wave

the signal is very short and non periodic - which results in a poor FFT resolution

$$R_{FFT} = \frac{f_s}{N}, \tag{6.4}$$

with $N$ as the number of data points of the input signal and $f_s = \frac{1}{dt}$ the frequency of the data points. Increasing the resolution of the frequency spectrum is only possible if the pressure signal is recorded over a longer period of time (increasing $N$), or the time steps $dt$ are reduced even further. The latter was not possible due to computational restrictions, the former can be even achieved without increasing the computing time by 'zero padding' the signal before applying the FFT, as the observed signal is only a short peak and not periodic. This technique interpolates the data in the frequency spectrum by adding zeros to the original signal for a better read-out. Each observed signal was padded with ten times of its length.

# 7 Evaluation

The goal of this chapter is to demonstrate the pressure distribution in the brain and assess the influence of the skull and the attenuation models applied on the different applicators. Both the resulting focal zone and the pressure signal in the focal centre are being studied.

## 7.1 Simulation in the Water Bath

To compare the influence of the skull, reference simulations in the water bath without any obstacles are created for each applicator. As indicated in section 5.2, the focus point was set by using a lower resolution and a lower pressure. Afterwards the pressure was increased to 20 MPa without re-adjusting the focal point again, even if it is possible for the focal points to be displaced differently depending on the used applicator. This is due to the inclusion of higher frequency components and different reflection angles at the metal reflectors. This decision is based on the high computational cost at the higher resolution and the complexity of the applicators, which makes the adaptation process a tedious task with many repetitions.

### Scalar Parameters

The maximal pressure of all the applicators was optimized to be 20 MPa with a deviation of less than 10 % at the focal centre, the other parameters strongly vary between the different technologies. The $\mathrm{p}_{+,max}$ and $\mathrm{p}_{-,max}$ listed in table 7.1 are the maximum and minimum occurring pressure in the water. The translation value $d_A$ represents the focal shift from the predefined centre located 45 mm from the applicator surface, the values $d_x$ and $d_y$ are the focal shift in the x-y plane. In figure 7.1 (and similarly in all the other pressure signal plots) the recorded curve is the signal along the applicators axis with the highest pressure; no translations in the x-y plane were taken into account. The gradient $\frac{\Delta p}{\Delta t}$ and the PII are calculated using their respective curve.

Table 7.1: The maximum and minimum pressure, gradient and energy flux density in a water bath obtained by numerical simulation for the different technologies. The last column represents the translation from the geometric focus centre in the direction of the axis $d_A$ and the x-y plane $d_x$, $d_y$.

| Applicator | $p_{+,max}$ [MPa] | $p_{-,max}$ [MPa] | $\frac{\Delta p}{\Delta t}$ [Pa/s] | PII [mJ/mm$^2$] | $d_A$/ $d_x$/ $d_y$ [mm] |
|---|---|---|---|---|---|
| EH, parabolic | 21.25 | -1.94 | 1.62e+14 | 0.0438 | 2.72/0.17/0.17 |
| EH, elliptical | 20.09 | -1.48 | 1.11e+14 | 0.0418 | 1.36/0.00/0.00 |
| EM | 19.04 | -11.92 | 3.61e+13 | 0.1990 | 3.28/0.17/0.17 |
| PE, $F_\# = 0.68$ | 21.82 | -12.59 | 8.01e+13 | 0.1236 | -0.17/0.00/0.00 |
| PE, $F_\# = 0.87$ | 21.47 | -10.79 | 9.86e+13 | 0.1020 | 0.34/0.00/0.00 |

As displayed in table 7.1 and in figure 7.1 the energy transported with the EH applicators is a fraction of the other technologies. A reason for that may be the high frequency which needs the pressure to be higher to increase the energy. The EH signal is also distorted due to numerical disturbances, which are a sign of a resolution that is too low to be able to support the occurring frequencies. While using the same input signal shape, a difference between the parabolic and the ellipsoidal applicator signal could be still observed. This may partly be due to the larger focal zone of the parabolic applicator which requires a three times larger pressure scaling factor to be applied on the input signal to reach the target pressure of 20 MPa. Increasing the input pressure generally also increases the proportion of higher frequencies resulting in a poorer performance even if the resolution is kept the same.

The EM applicator shows the lowest gradient while having the highest PII; this is due to its long duration and low base frequency.

Both of the PE signals show very similar properties, some slight variations are found, though. The applicator with the $F_\# = 0.87$ shows a higher gradient, but a lower tensile pressure and PII. This would coincide with the theory presented in section 5.2 which states that an applicator with a higher $F_\#$ generates a steeper gradient, but at the cost of a higher energy loss. Another reason could also be slight variations in the input signal: the shape is the same, but the amplitude is not.

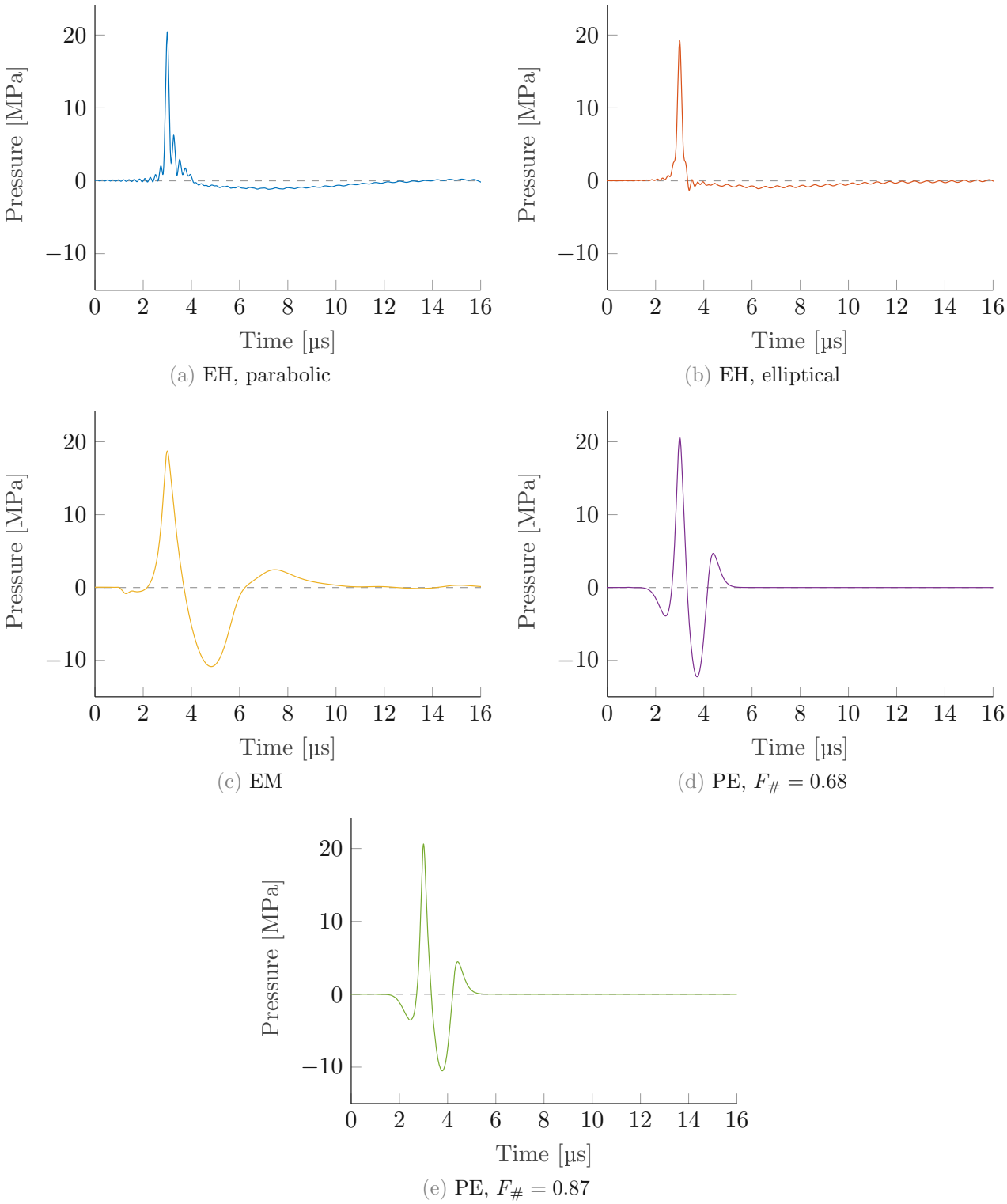


(a) EH, parabolic

(b) EH, elliptical

(c) EM

(d) PE, $F_{\#} = 0.68$

(e) PE, $F_{\#} = 0.87$

Figure 7.1: Pressure signals of the simulations in the water bath along the axis in the respective focal centre; for a better overview the time axis was adjusted to the same interval.

A look at the Fourier analysis of the signal in figure 7.2 substantiates the mentioned numerical disturbances: the PE and EM signals have a natural decay before they reach the cut-off frequency of 4 MHz, the resolution is sufficient to depict their properties. However, the EH signal shows a rapid decay after it reaches this threshold; due to the computational restrictions no improvements were possible to avert it. These disturbances show an effect on all the parameters. This casts doubt on the question whether the simulation of the EH applicator in the water bath is feasible at this resolution. In figure 7.2 also the to the area of the resulting signals normalized Fourier spectra of the input signals is depicted[1]. This makes it possible to visualise the in section 1.4 described and anticipated frequency shift.

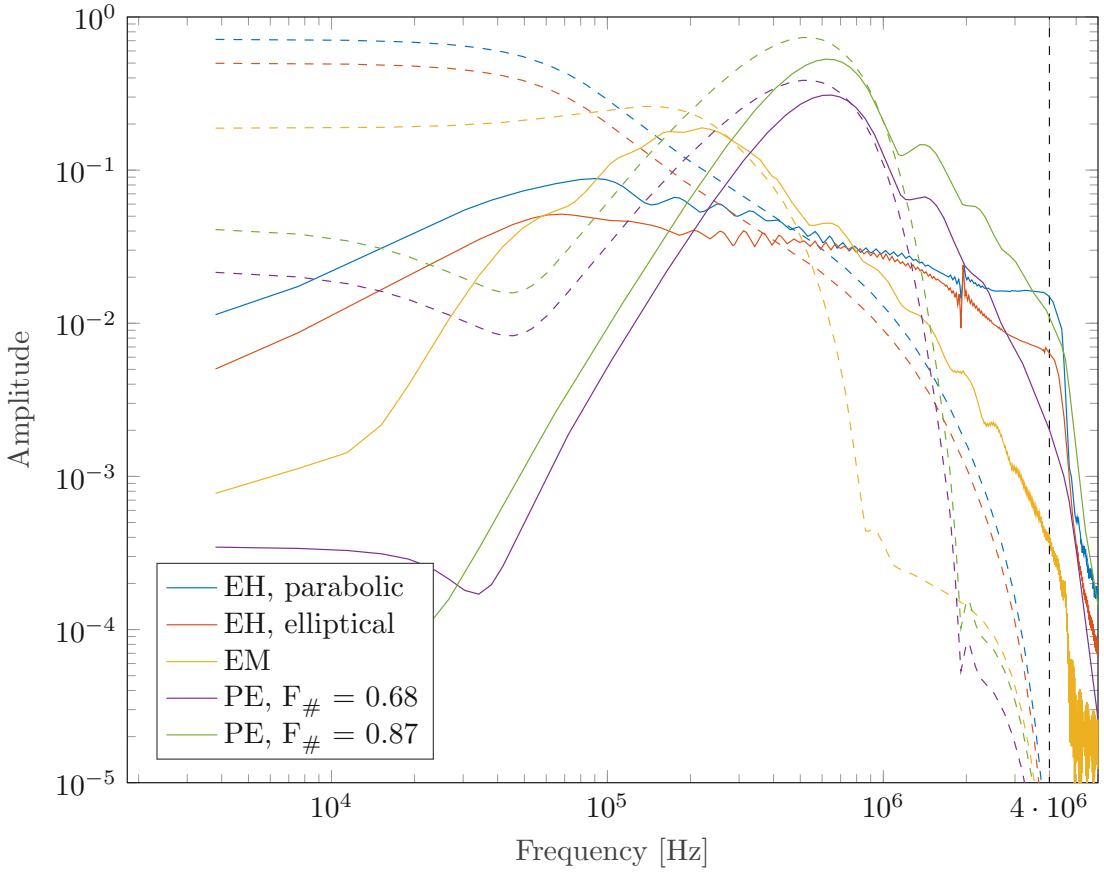


Figure 7.2: Fourier analysis for the pressure signals of the simulations in the water bath in the respective focal centre (solid), and the respective normalized input signals (dashed), with the cut-off frequency of 4 MHz.

[1]The normalization was necessary due to the difference in magnitude between the signals.

## Focal Zone

In figure 7.4 a longitudinal section of the maximal pressure reached during the simulation is illustrated. These figures can be used to calculate the dB zones and for a comparison with -6 dB zone of the model applicators in figure 5.1 an idealization in the form of an ellipsoid is generated in figure 7.3 (see appendix A.7 for the non idealized zone shape). Due to the scaling and partly remodelling of most of the reflectors only a qualitative comparison is possible.

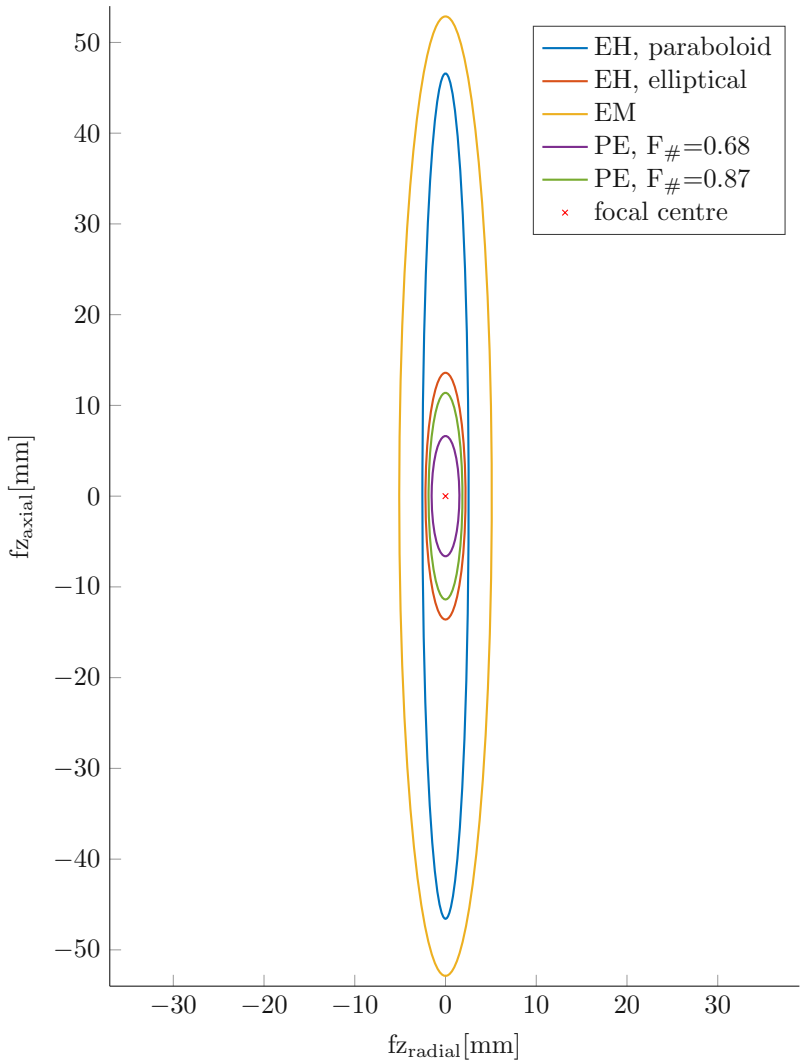


Figure 7.3: Comparison of the longitudinal sections of the -6 dB pressure focal zones calculated by the simulation for the different applicators; $fz_{radial}$ shows the width of the focal zone in the radial direction, $fz_{axial}$ shows the length in the axial direction around the central focus point. The translations of the focal zones are neglected.

The most noticeable difference is the size of the two parabolic applicators, namely the EM and the EH with the parabolic reflector. It seems that the assumptions made for the reflector function were too vague to come close to their model applicator. The second EH applicator with the elliptical reflector and the two PE applicators on the other hand behaved as expected, providing a small focal zone. The differences in length discussed in section 5.2 due to the different $F_{\#}$ have been confirmed; the applicator with the smaller $F_{\#}$ produces a longer focal zone.
It is worth mentioning that due to a randomly switching position of the plasma spark in the EH applicators the displayed focal zones are rather idealized, in a real application the focal zone would jump with every new ignition and be deformed - the focal zone provided by the manufacturer and the simulated one are therefore assumed to be the 'average' focal zone.

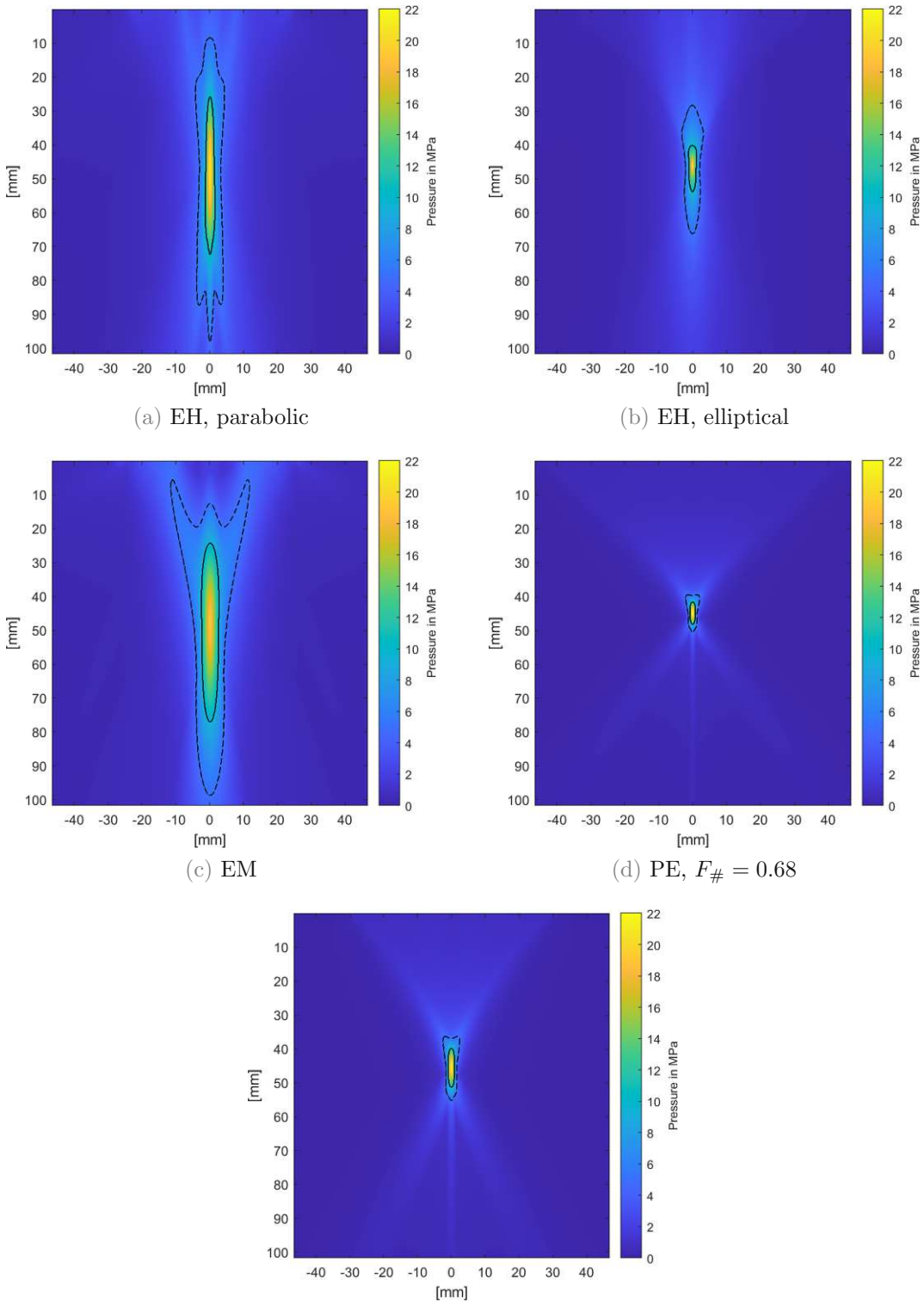


(a) EH, parabolic

(b) EH, elliptical

(c) EM

(d) PE, $F_{\#} = 0.68$

(e) PE, $F_{\#} = 0.87$

Figure 7.4: Longitudinal section of the maximal pressure reached in an empty water bath; the dashed line and the solid line represent the 5 MPa and -6 dB zone respectively.

## 7.2 Simulation with the CT

In this section the different attenuation models of the bone are compared, as the attenuation values for the soft tissue are kept the same. As visible in figure 7.5 the differences in the attenuation models do not only change the amplitude, but also some deviations in the gradients are visible. As anticipated, the models with a higher attenuation generate a greater dampening effect. This results in only minor changes in the frequency spectra between the models (see Appendix A.9). Due to the higher speed of sound in bone the pressure signals arrive sooner than in the empty water bath. For a better comparison of the signal shapes, all the signals were aligned manually, and the time differences between the empty water bath simulation and the different attenuation models are listed in table 7.2. The discrepancy between the different technologies are possibly due to the various apertures and the propagation pathway.

Table 7.2: The time gap of the maximal pressure between the water bath and the different attenuation models.

| Applicator | Homogeneous [µs] | Pichardo [µs] | McDannold [µs] |
|---|---|---|---|
| EH, parabolic | -1.92 | -2.78 | -2.79 |
| EH, elliptical | -4.44 | -5.91 | -5.36 |
| EM | -3.81 | -6.56 | -6.56 |
| PE, $F_{\#} = 0.68$ | -4.03 | -5.38 | -4.92 |
| PE, $F_{\#} = 0.87$ | -4.02 | -4.94 | -4.96 |

In table 7.3 the most important parameters for each attenuation model are listed. In comparison to the simulation in the water bath (see table 7.1), almost all properties are dampened in one way or another: The maximal and minimal pressure is lower, but the loss was not as bad as anticipated: Depending on the applicator, the pressure only reaches 50 % of the values simulated in the empty water bath, instead of the expected $80 - 90$ % [74]. The tensile pressure component is generally less affected than its compressive counterpart; in some cases even a gain has been observed.

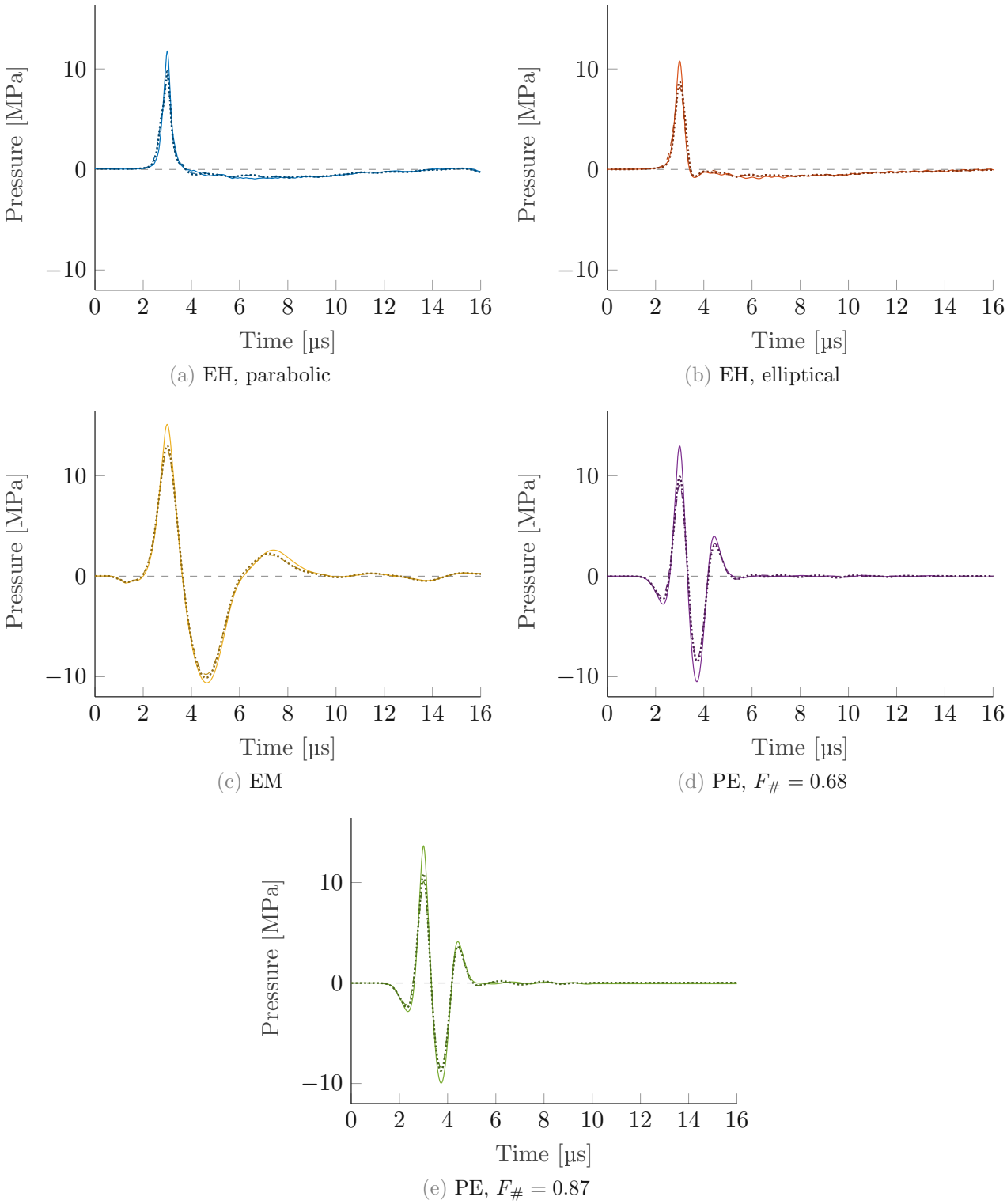


(a) EH, parabolic

(b) EH, elliptical

(c) EM

(d) PE, $F_{\#} = 0.68$

(e) PE, $F_{\#} = 0.87$

Figure 7.5: Pressure signals of the simulations for the different attenuation models (solid line = Homogenous, dashed line = McDannold [61], dotted line = Pichardo [78]) along the axis closest to the respective shifted focal centre. The latter two are mostly overlapping and almost undistinguishable. For a more adequate comparison all of the signals were aligned manually, the measured time delays are listed in table 7.2.

Table 7.3: The maximum and minimum pressure, gradient and energy flux density of the simulation with the CT applying the different attenuation models for the different technologies. The last column represents the translation in the direction of the axis $d_A$ and the x-y plane $d_x$, $d_y$ from the geometric focus centre.

*(a)* Homogenous attenuation coefficient

| Applicator | $p_{+,max}$ [MPa] | $p_{-,max}$ [MPa] | $\frac{\Delta p}{\Delta t}$ [Pa/s] | PII [mJ/mm$^2$] | $d_A$/ $d_x$/ $d_y$ [mm] |
|---|---|---|---|---|---|
| EH, parabolic | 18.10 | -2.41 | 3.03e+13 | 0.0284 | -4.08/-0.34/0.85 |
| EH, elliptical | 14.32 | -1.29 | 2.89e+13 | 0.0255 | -4.08/-0.34/0.68 |
| EM | 16.63 | -12.00 | 2.28e+13 | 0.1784 | -4.37/-0.17/0.85 |
| PE, $F_\# = 0.68$ | 13.36 | -10.81 | 3.99e+13 | 0.0735 | -3.4/0.00/0.00 |
| PE, $F_\# = 0.87$ | 15.35 | -10.50 | 4.54e+13 | 0.0717 | -4.25/-0.34/0.51 |

*(b)* McDannold et al. [61]

| Applicator | $p_{+,max}$ [MPa] | $p_{-,max}$ [MPa] | $\frac{\Delta p}{\Delta t}$ [Pa/s] | PII [mJ/mm$^2$] | $d_A$/ $d_x$/ $d_y$ [mm] |
|---|---|---|---|---|---|
| EH, parabolic | 15.43 | -4.14 | 1.59e+13 | 0.0222 | -4.08/-0.34/1.19 |
| EH, elliptical | 12.18 | -1.34 | 1.69e+13 | 0.0184 | -4.08/-0.34/0.85 |
| EM | 14.91 | -10.76 | 1.73e+13 | 0.1494 | -4.37/-0.17/1.02 |
| PE, $F_\# = 0.68$ | 9.76 | -8.83 | 2.46e+13 | 0.0427 | -4.25/-0.17/0.34 |
| PE, $F_\# = 0.87$ | 12.97 | -9.55 | 2.84e+13 | 0.0469 | -4.42/-0.17/0.68 |

*(c)* Pichardo et al. [78]

| Applicator | $p_{+,max}$ [MPa] | $p_{-,max}$ [MPa] | $\frac{\Delta p}{\Delta t}$ [Pa/s] | PII [mJ/mm$^2$] | $d_A$/ $d_x$/ $d_y$ [mm] |
|---|---|---|---|---|---|
| EH, parabolic | 17.07 | -3.71 | 1.78e+13 | 0.0234 | -4.08/-0.34/1.02 |
| EH, elliptical | 13.18 | -1.53 | 2.36e+13 | 0.0200 | -4.08 -0.34 0.85 |
| EM | 15.30 | -11.13 | 1.83e+13 | 0.1572 | -4.37/-0.17/1.02 |
| PE, $F_\# = 0.68$ | 10.50 | -9.16 | 2.90e+13 | 0.0473 | -5.27/0.17/0.17 |
| PE, $F_\# = 0.87$ | 13.91 | -10.06 | 3.23e+13 | 0.0528 | -5.27/0.00/0.68 |

The gradient of the signal has also become smaller, but the EH applicators are affected the most. Even if the numerical disturbances are greatly reduced due to the skull, which acts as a low-pass filter (see figure 7.2), the result is still surprising: the gradient is of the same magnitude as the other technologies. Assuming that the numerical disturbances do not influence the simulation with the CT, it seems

that the skull balances out the advantage of the EH technology, i.e., the shock wave being present already at the point of generation.
The PII of almost all applicators is reduced, with the EM applicator being able to maintain the most energy flux density while propagating through the skull. Apart from its low main frequency it is assumed that its big focal zone helps maintain the energy at its core: With a small focal zone each interference on the propagating path scatters the shock wave and reduces the energy in the focal spot. If the focal zone is of a considerable size, some of the scattered waves are replaced by others. While this may reduce the size and shape of the focal zone, the area around the focal spot is still fairly energetic.

The displacement of the focal zone is similar in all cases, therefore it is assumed that the skull introduces a systematic translation which barely depends on the attenuation coefficient. As described in section 4.1, the skull acts as an acoustic lens and moves the focus closer to the skull. It is also fascinating to detect that the differences in displacement between the different applicators in the water bath are almost compensated by the skull. In other words, smaller differences in the focal length show almost no influence in the focus shift, the skull re-focusses them being an acoustic lens. Changing the position and incident angle of the applicators on the other hand should influence the positioning of the focus spot.

Examining the maximum pressure map on the same position as before (see figure 7.6) we may conclude, that additionally to the focus shift, the applicators hardly retain their focal zone shape (also visible in the dB zones, see appendix A.8). Especially the applicators with a smaller focal zone show a visible distortion, a uniform pressure distribution can not be maintained. The position of the skull is clearly visible due to a pressure build-up in the bone, the biological impact of this is unclear and should be subject to future research.

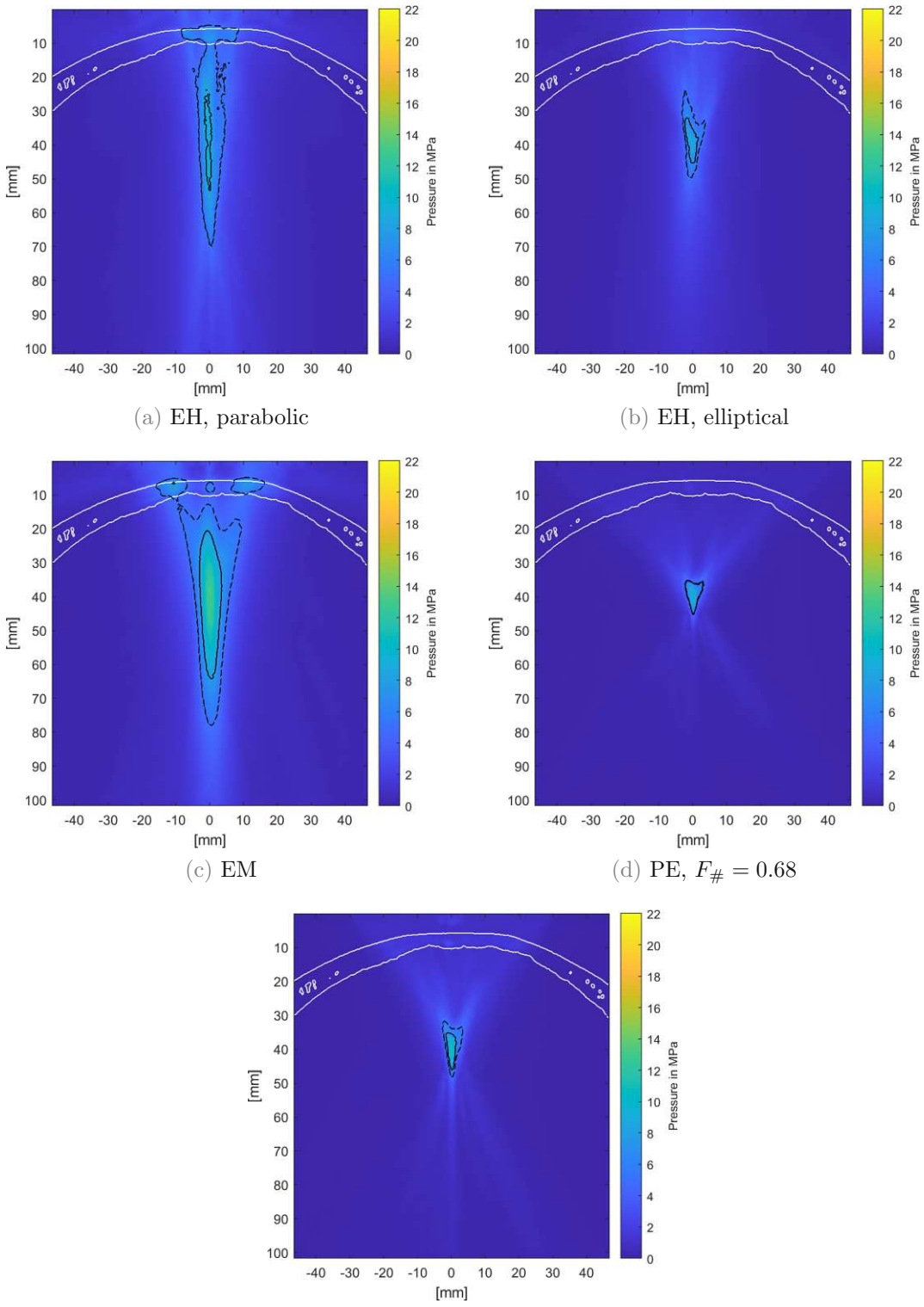


(a) EH, parabolic

(b) EH, elliptical

(c) EM

(d) PE, $F_{\#} = 0.68$

(e) PE, $F_{\#} = 0.87$

Figure 7.6: Longitudinal section of the maximal pressure in the CT, using the Pichardo [78] attenuation model; the dashed line and the solid line represent the 5 MPa and -6 dB zone respectively.

## 7.3 Propagation Influence of the Skull

While being different, the differences in the attenuation models are not large enough to compare all of the attenuation models with the empty water bath to show the influence of the bone. The model suggested by Pichardo et al. described in section 4.3 has been chosen since its seems to be a compromise between the other two models.

In figure 7.7 the signals of the water bath simulations are compared with the CT by using the attenuation model by Pichardo et al., in table 7.4 the properties are shown in more detail. Most of the differences are attributed to the skull as its dampening properties and non-linearity parameters are by a factor greater than the ones associated with the soft tissue.

Table 7.4: In this chart the results of the simulation between the empty water bath and the water bath with the CT by using the attenuation coefficient suggested by Pichardo et al. are being compared.

| Applicator | $p_{+,max}$ [%] | $p_{-,max}$ [%] | $\frac{\Delta p}{\Delta t}$ [%] | PII [%] |
|---|---|---|---|---|
| EH, parabolic | 80.3 | 191.2 | 10.9 | 53.4 |
| EH, elliptical | 65.6 | 103.4 | 21.3 | 47.8 |
| EM | 80.4 | 93.4 | 50.7 | 79.0 |
| PE, $F_{\#} = 0.68$ | 48.1 | 72.8 | 36.2 | 38.3 |
| PE, $F_{\#} = 0.87$ | 64.8 | 93.2 | 32.8 | 51.8 |

The introduction of the skull as an obstacle can be described as an attenuation mechanism which reduces the pressure and energy, but also acts as a low-pass filter reducing the gradients.
Especially the EH applicators show big variations; the chances are that the properties of the EH applicators are not comparable at the resolution used; while the simulation with the skull included show less disturbances with less visible oscillations of the signal, the simulation in the water bath calls for a higher resolution to be considered faithful.

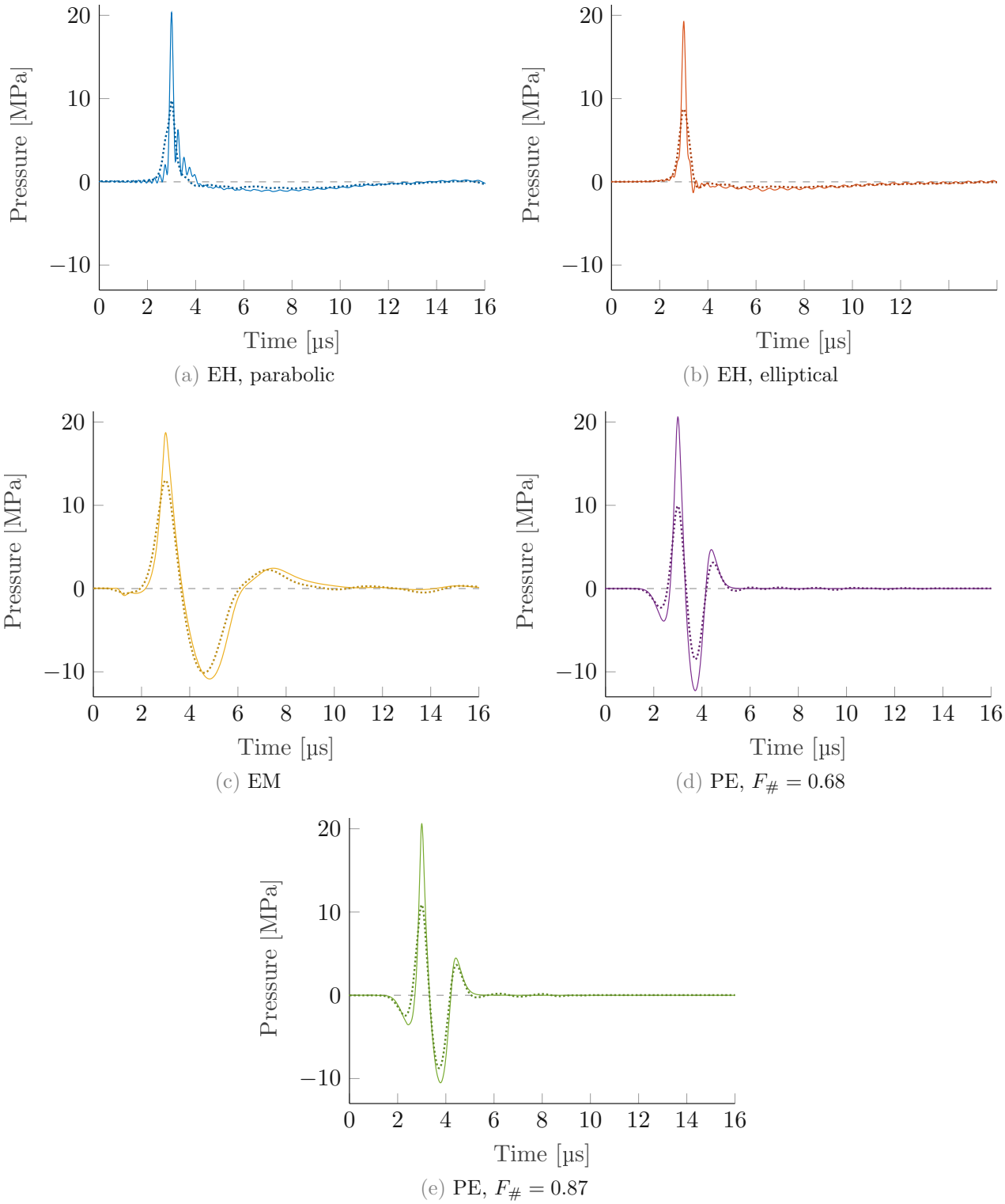


(a) EH, parabolic

(b) EH, elliptical

(c) EM

(d) PE, $F_{\#} = 0.68$

(e) PE, $F_{\#} = 0.87$

Figure 7.7: Pressure signals of the simulations in the empty water bath (solid) compared to the CT with the attenuation model by Pichardo [78] (dotted) along the axis closest to the respective focal centre. For a more adequate comparison all of the signals were aligned manually, the measured time delays are listed in table 7.2.

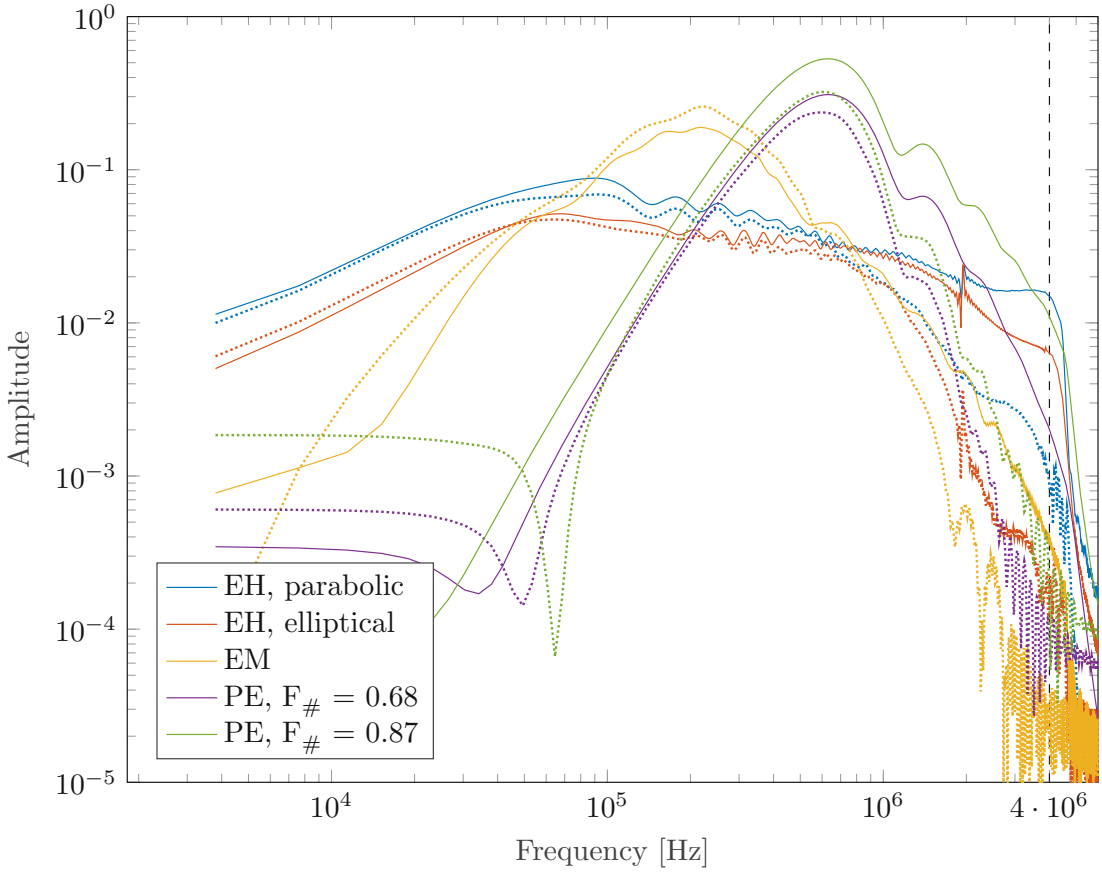


Figure 7.8: Fourier analysis for the pressure signals of the simulations in the empty water bath (solid) compared to the CT with the attenuation model by Pichardo [78] (dotted) along the axis closest to the respective focal centre, with the cut-off frequency of 4 MHz.

The differences between the two setups are also very visible in the frequency spectrum (see figure figure 7.8): a general dampening of higher frequencies can be observed, and a steep fall-off above the $500-600$ kHz region can be identified. The EH applicators are the most affected by this, since a significant part of their frequencies are above 1 MHz, while the EM and PE applicator show a distinct main frequency peak of about 200 kHz and 600 kHz respectively.

As discussed in section 4.1 a maximal frequency of 500 MHz is suggested for the penetration of a skull bone, and a fall-off in the simulation with the skull above this frequency can be detected. On the other hand, this fall-off could also be explained with a lack of resolution: it is possible that the simulation is not precise enough to feature material changes properly, and that a higher PPW is necessary as discussed in section 6.1. It also seems that the bigger the focal zone is in the water bath, the

better it maintains its parameters. As analysed before in 7.2, it is assumed that with a bigger focal zone the loss of a few focussed pressure waves does not influence the result as much since they are replaced by other scattered waves. This would explain the minor pressure losses and the frequency amplitude gain in the EM applicators and partly the differences between the two PE applicators as well. The advantage of longer focal zones, that was analysed in section 5.2 may also have an impact on the result.

Applying the shock wave in a focussed manner to destroy tissue may be difficult, only a therapy of a wider area would be possible without any further strategies.

## 7.4 Phase Correction Method

One of these strategies would be the phase correction method as explained in section 5.4. Phase correcting the PE applicator with $F_{\#} = 0.87$ using the Pichardo attenuation model leads to a significant improvement (see figure 7.9 and table 7.5).

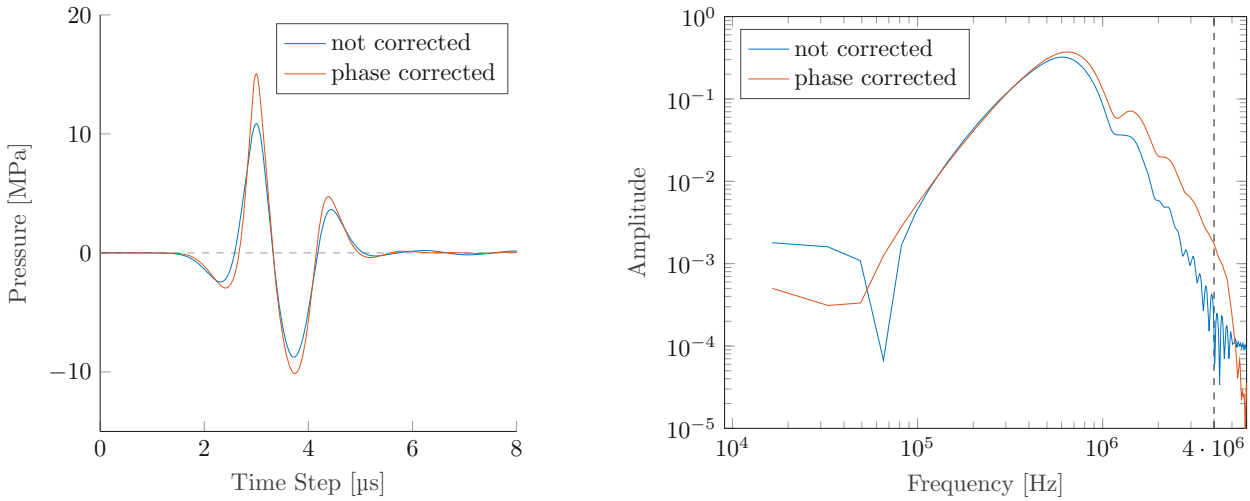


(a) signal pressure

(b) frequency spectrum

Figure 7.9: Comparison of the pressure signals and their frequency spectrum for the non-corrected and the phase corrected PE applicator.

Table 7.5: Comparison of the PE applicator with $F_{\#} = 0.87$ with and without the phase correction method; the empty water bath simulation serves as a reference.

| Applicator | $p_{+,max}$ [MPa] | $p_{-,max}$ [MPa] | $\frac{\Delta p}{\Delta t}$ [Pa/s] | PII [mJ/mm$^2$] | $d_A$/ $d_x$/ $d_y$ [mm] |
|---|---|---|---|---|---|
| Water bath | 21.47 | -10.79 | 9.86e+13 | 0.1020 | 0.34/0.00/0.00 |
| Phase correction | 15.54 | -10.29 | 5.98e+13 | 0.0762 | 0.17/0.00/0.00 |
| Non-corrected | 13.91 | -10.06 | 3.23e+13 | 0.0528 | -5.27/0.00/0.68 |

Due to the phase correction the maximal pressure amplitude is improved, and more higher frequencies components present at the focal centre. This results in a significant steeper gradient, but also in a higher preserved PII, while the focal centre is even closer to the actual geometric centre than the PE simulation in the water bath (see table 7.5).

The focal zone differences are clearly evident in the pressure zone plot (see figure 7.10). While the phase corrected simulation shows more asymmetry than the base simulation in the water bath (see figure A.7, (e)), it can definitely be seen as an improvement compared to the non-corrected PE applicator.

As pointed out before, phase correction requires a CT of the individual and an applicator with individually controllable piezoelectric elements. On top of that, an exact positioning of the applicator is needed, which makes an additional positioning device indispensable if a handheld applicator is used.

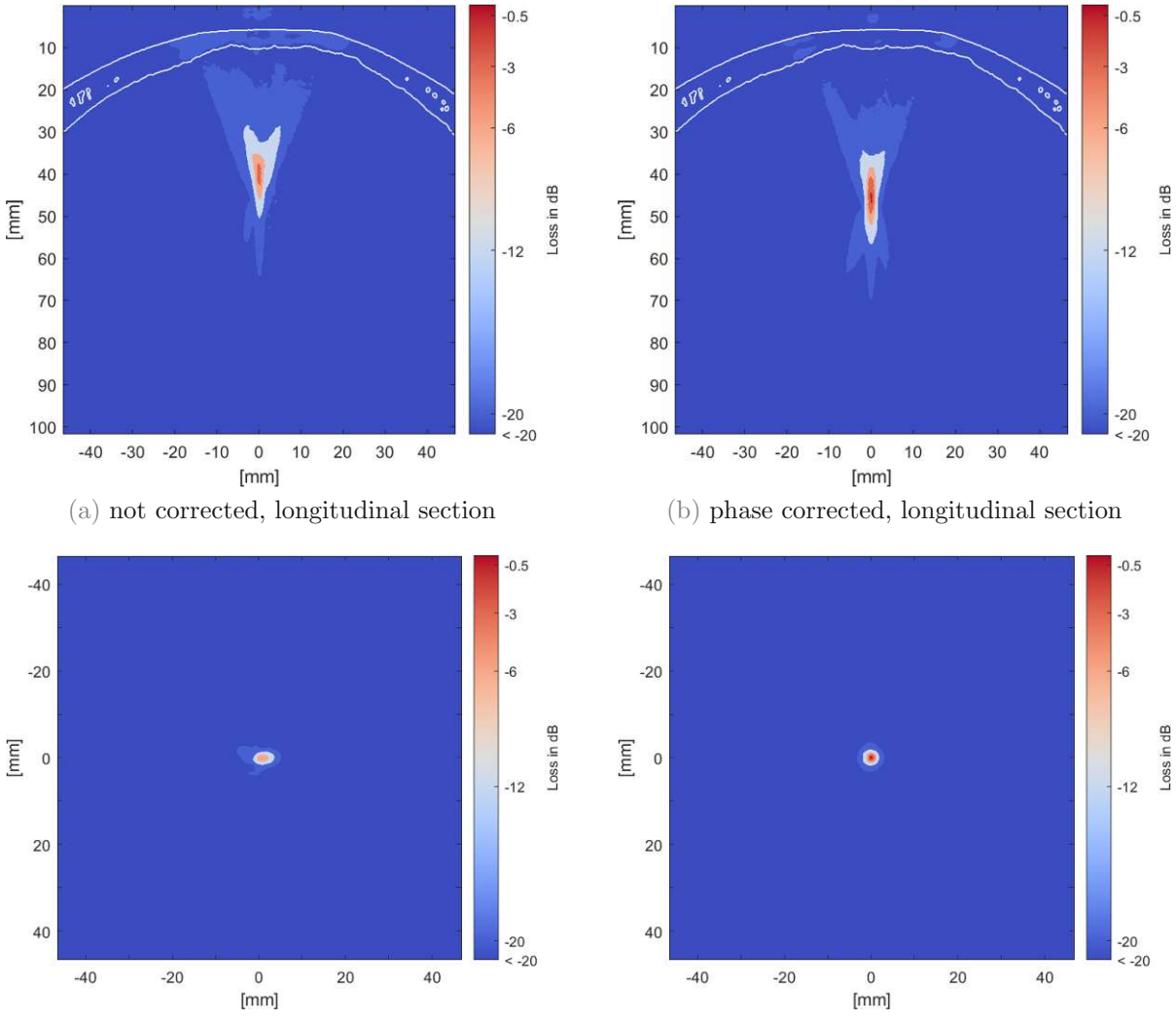


(a) not corrected, longitudinal section

(b) phase corrected, longitudinal section

(c) not corrected, cross section

(d) phase corrected, cross section

Figure 7.10: Comparison of the dB zones for the non-corrected and the phase corrected simulation with the CT.

## 7.5 Summary

In this closing summary the most evident results should be highlighted:

- numerical disturbances are visible in the EH signal, caused by the inability of the grid to support higher frequencies;
- the PII of the implemented applicators vary, with the EM applicator having the highest energy flux density, and the EH applicators the lowest;
- the gradient of the EH might be the steepest, but due to numerical disturbances the simulation is probably unreliable;
- the gradient of the EH is attenuated the most by the skull due to the high frequencies - the skull is acting as a low-pass filter, but possibly the grid is also not able to properly resolve the high frequencies;
- a shift to the higher frequency range in the PE applicators becomes apparent when a higher $F_{\#}$ is used; if the same input signal is used, this results in a lower transported energy due to higher losses with an increased frequency and a steeper gradient;
- the different technologies have a clearly distinguishable Fourier spectrum; the EM and PE applicator show a main frequency peak with a clear fall-off above a certain frequency; the EH has a very wide frequency range without a determinable main frequency;
- as anticipated, the skull acts as an acoustic lens, the focal point is shifted closer to the bone - the actual position is only predictable with a simulation, and without a phase correction not every area of the brain can be reached;
- a bigger focal zone may be favourable to maintain a stable signal at the focal centre - the scattering induced by the skull may have a less effect due to the refocussing of previously unfocussed pressure waves;
- the different attenuation models can affect the pressure and energy properties of the signal, but less so on its pressure distribution and on its focal shape;
- phase correction for the PE applicator comes with an overall increase in pressure, energy and a steeper gradient, while having no focal centre shift. This results in an improved focal zone shape.

# Conclusion

The aim of this study was to reproduce different shock wave applicator technologies and observe the influence of the skull on shock wave propagation in the brain using the MATLAB toolbox k-Wave. In order to examine the differences three different attenuation models were selected and their influence on the focal zone and the pressure signal at its centre was investigated.

It was possible to illustrate differences in the applicators technologies and their behaviour while passing through the skull, although the simulation is restricted in its resolution due to the computational power. Especially the EH applicator is difficult to simulate due to its reliance on high frequency components that resulted in visible numerical disturbances - it is advisable to increase the resolution even further. Moreover, applicators with a bigger focal zone and a low frequency spectrum seem to have an advantage in maintaining the maximal pressure and energy. This is due to the fact to that the skull acts as a low-pass filter, and a wide focal zone is more forgiving with scattered rays. These properties mainly apply to the observed EM applicator, which would thereby be recommended for a transcranial therapeutic application.
In addition to the frequency influence, the skull acts as an acoustic lens, which shifts the focal centre according to its curvature and introduces a systematic error which occurs in all technologies observed. Therefore for a destructive use a more refined control is needed, which is only possible in a PE applicator with individually addressable piezoelectric elements. Additionally the size of the focal zone of PE applicators can be easily reduced by changing its $F_{\#}$, on the downside this also reduces its ability to produce a steep shock wave.

The three different attenuation models observed proved to have a significant impact on the maximal pressure and on its parameters connected like PII and pressure gradient, but only a minor effect on displacement and frequency spectrum. To calculate only the position and shape of the focal zones the attenuation model has a minor effect, for calculating the actual pressure magnitude, the PII and the gradient a better understanding of the dependency of the attenuation of bone to the resolution of the CT is needed.

# A Appendix

## A.1 Taylor Series

The Taylor series delivers an approximation of a function $f(x)$ in a certain radius $r$ at a value $a$:

$$f(x) = f(a) + \frac{f'(a)}{1!}(x-a) + \frac{f''(a)}{2!}(x-a)^2 + \frac{f^{(3)}(a)}{3!}(x-a)^3 + \dots . \tag{A.1}$$

The chosen value $x$ should be in the interval $[(a-r) \leq x \leq (a+r)]$, the accuracy and the radius depend on the function which is expanded and the number of polynomials used.

As mentioned in section 1.3 the function $f = p(\rho)$ should be expanded around the value $a = 0$. This leads to

$$f = p(\rho) = p(0) + \frac{1}{1!}\left(\frac{d\,p}{d\,\rho}\right)_0 (\rho) + \frac{1}{2!}\left(\frac{d^2\,p}{d\,\rho^2}\right)_0 (\rho)^2 + \frac{1}{3!}\left(\frac{d^3\,p}{d\,\rho^3}\right)_0 (\rho)^3 + \dots .$$

Due to its definition in (1.5), $p(0)$ equals to 0:

$$p(\rho) = \frac{\rho_0}{1!}\left(\frac{d\,p}{d\,\rho}\right)_0 \left(\frac{\rho}{\rho_0}\right) + \frac{\rho_0^2}{2!}\left(\frac{d^2\,p}{d\,\rho^2}\right)_0 \left(\frac{\rho}{\rho_0}\right)^2 + \frac{\rho_0^3}{3!}\left(\frac{d^3\,p}{d\,\rho^3}\right)_0 \left(\frac{\rho}{\rho_0}\right)^3 + \dots .$$

With the definition of

$$A = \rho_0 \left(\frac{d\,p}{d\,\rho}\right)_0 , \; B = \rho_0^2 \left(\frac{d^2\,p}{d\,\rho^2}\right)_0 , \; C = \rho_0^3 \left(\frac{d^3\,p}{d\,\rho^3}\right)_0 , \tag{A.2}$$

the final equation is

$$p(\rho) = \frac{A}{1!}\left(\frac{\rho}{\rho_0}\right) + \frac{B}{2!}\left(\frac{\rho}{\rho_0}\right)^2 + \frac{C}{3!}\left(\frac{\rho}{\rho_0}\right)^3 + \dots . \tag{A.3}$$

## A.2 Power Series

Any polynomial function can be developed as power a series around a centre, for example the exponential function

$$e^x = exp(x) = \sum_{n=0}^{\infty} \frac{x^n}{n!}. \tag{A.4}$$

This is also possible for the root function

$$\sqrt{1+x} = 1 + \frac{1}{2}x - \frac{1}{2*4}x^2 + \frac{1*3}{2*4*6}x^3 \ldots , \tag{A.5}$$

with $-1 \leq x \leq 1$.

In the case of equation (1.17):

$$\begin{aligned} c &= v + \sqrt{{c_0}^2(1 + \frac{B}{A}\frac{v}{c_0})} \\ &= v + c_0\sqrt{1 + \frac{B}{A}\frac{v}{c_0}} \\ &= v + c_0\left(1 + \frac{1}{2}\frac{B}{A}\frac{v}{c_0}\right) \\ &= c_0 + \left(1 + \frac{B}{2\,A}\right)v. \end{aligned} \tag{A.6}$$

As mentioned before, $\frac{B}{A}\frac{v}{c_0}$ should be in the interval $[-1, 1]$. In soft tissue *BonA* values are $< 11$ therefore the particle velocity in water has to be less than 150 m/s to fulfil this requirement. With equation (1.13) the particle velocity in water for a wave of 100 MPa can be estimated to be less than 70 m/s.

## A.3 Attenuation Unit Conversion

The unit for absorption often differs from source to source. The simulation software used requires an input in the form of [dB/(MHz$^y$ cm)]. The following section discusses some example conversions.

- [dB/(kHz$^y$km)]
  While converting units one has to keep in mind that the frequency is exponentiated with the power law exponent, which has to be included:

$$\frac{\text{dB}}{\text{kHz}^y\,\text{km}} = \frac{1}{10^5 * 0.001^y}\,\frac{\text{dB}}{\text{MHz}^y\,\text{cm}}. \tag{A.7}$$

- [Np/(MHz$^y$ cm)]
  A frequently used absorption unit is Neper [Np]. While decibel uses the logarithm with a base of 10, Neper uses the natural logarithm instead:

$$ln\left(\frac{F_1}{F_2}\right)\,\text{Np} = 20\,lg\left(\frac{F_1}{F_2}\right)\,\text{dB}. \tag{A.8}$$

  To convert a variable from Np to dB it has to be multiplied with

$$1\,\text{Np} = \frac{20}{ln(10)}\,\text{dB} \approx 8.686\,\text{dB}. \tag{A.9}$$

- [Np/((rad/s)$^y$ m)]
  Neper is often used in combination with rad/s instead of MHz:

$$\frac{\text{Np}}{(\text{rad/s})^y\,\text{m}} = \frac{20}{ln(10)\,(2\,\pi\,10^6)^y\,10^2}\,\frac{\text{dB}}{\text{MHz}^y\,\text{cm}}. \tag{A.10}$$

## A.4 Tissue Histogram

A more detailed histogram without the brain, which takes up a large part of the histogram and makes the other tissues almost indistinguishable. The sharp borders are due to the introduced HU thresholds to properly differentiate between the tissue interfaces.

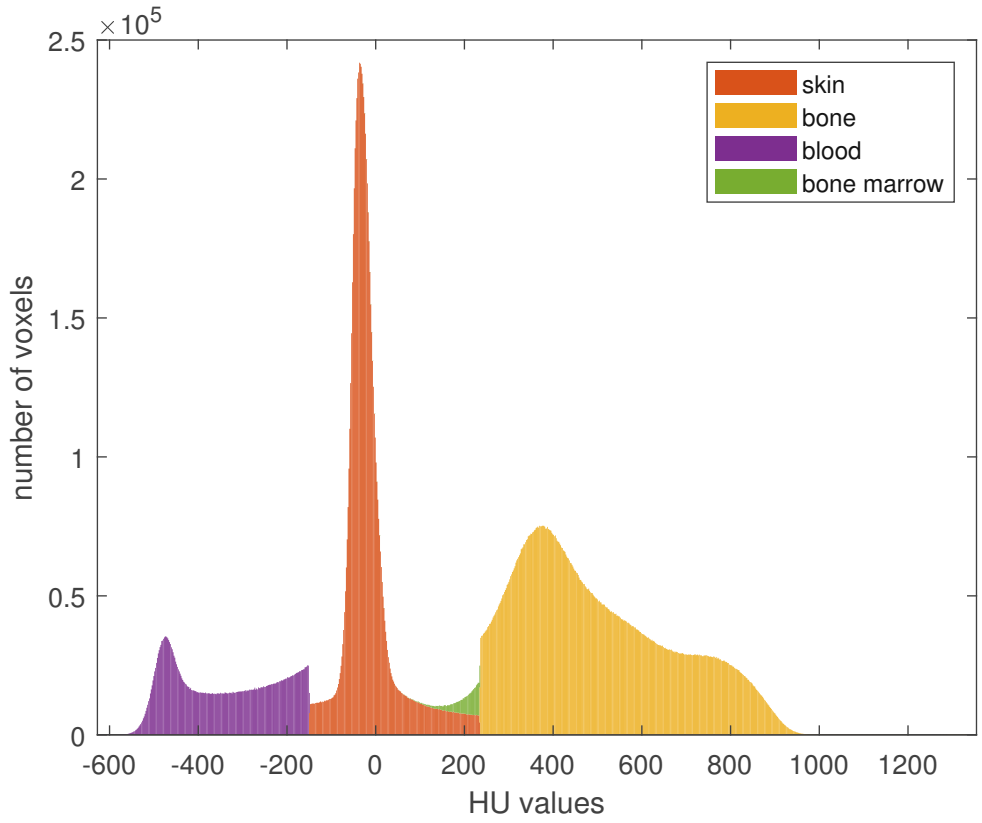


Figure A.1: A detailed histogram without the brain for a better overview.

## A.5 Used Applicators

### Ellipsoidal EH Applicator

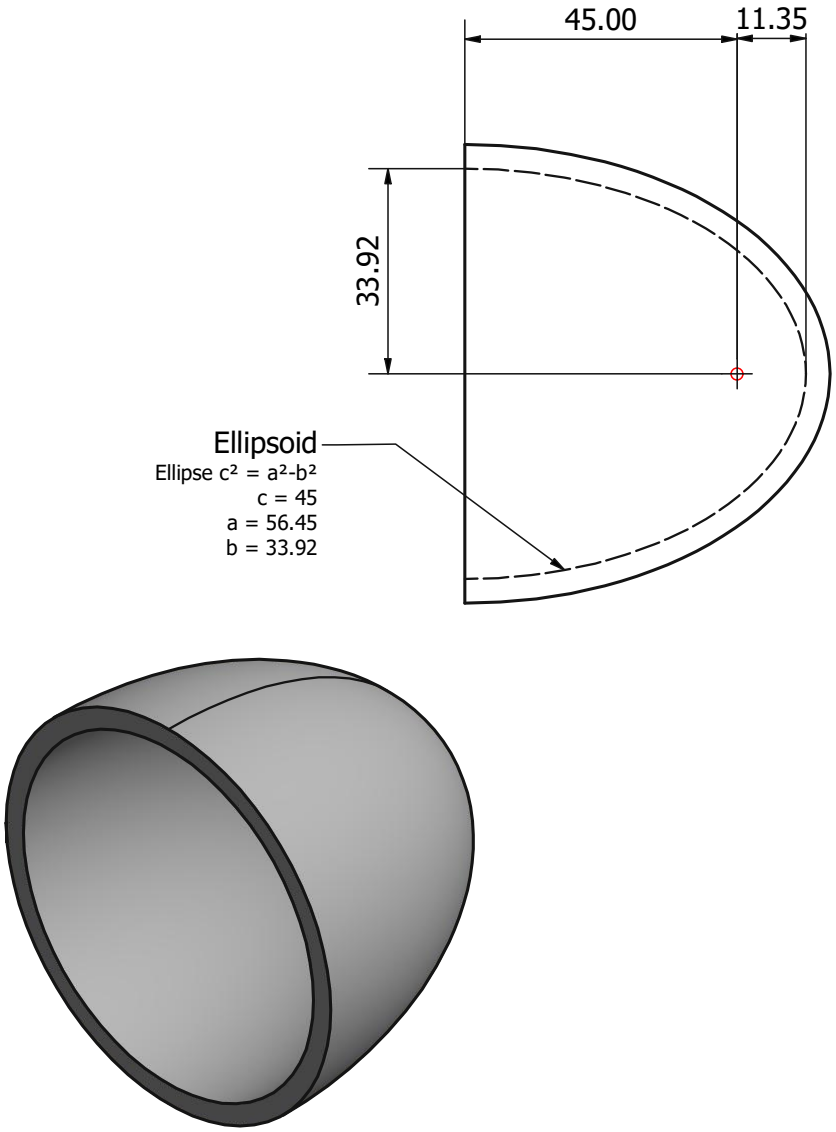


Figure A.2: Drawing of an ellipsoidal EH applicator.

## Paraboloid EH Applicator

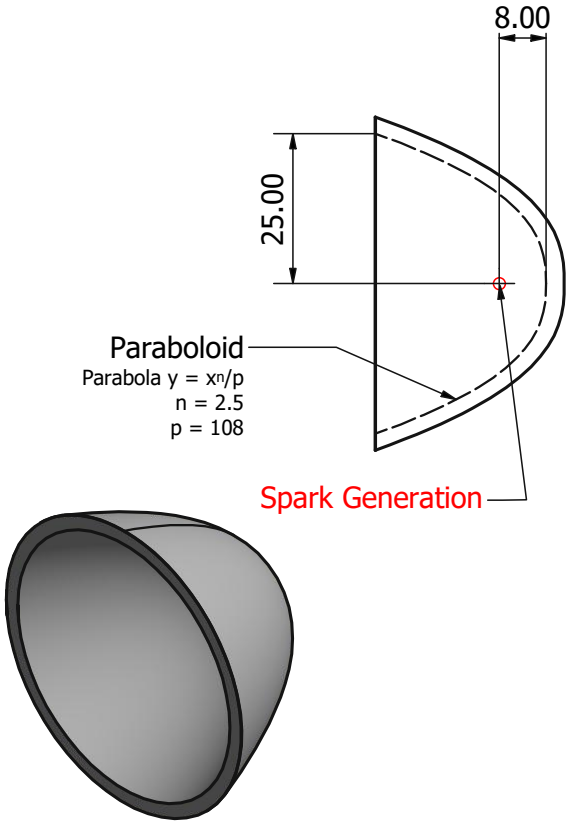


Figure A.3: Drawing of a paraboloid EH applicator.

## EM Applicator

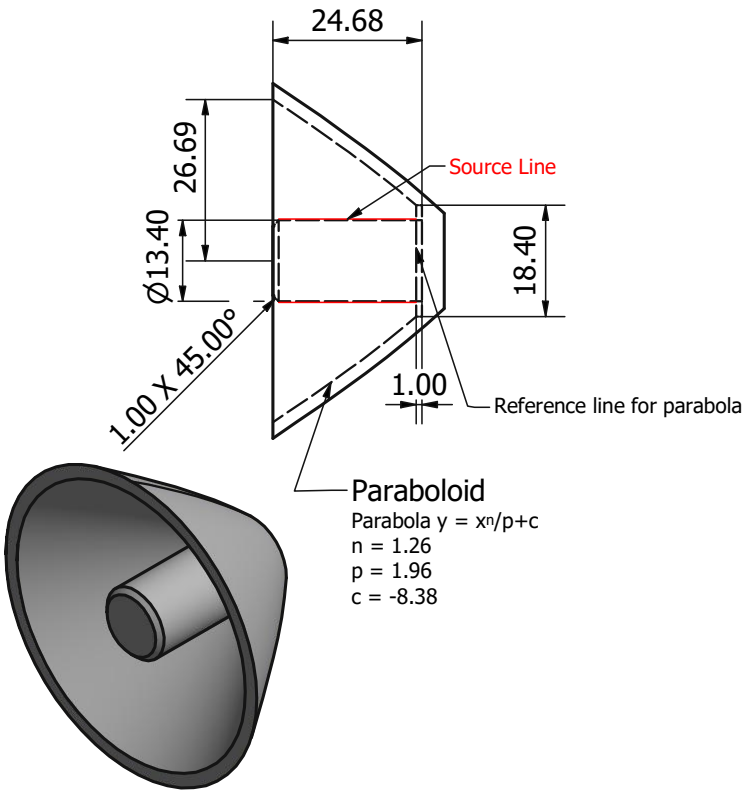


Figure A.4: Drawing of a EM applicator.

## PE Applicator with $F_{\#} = 0.68$

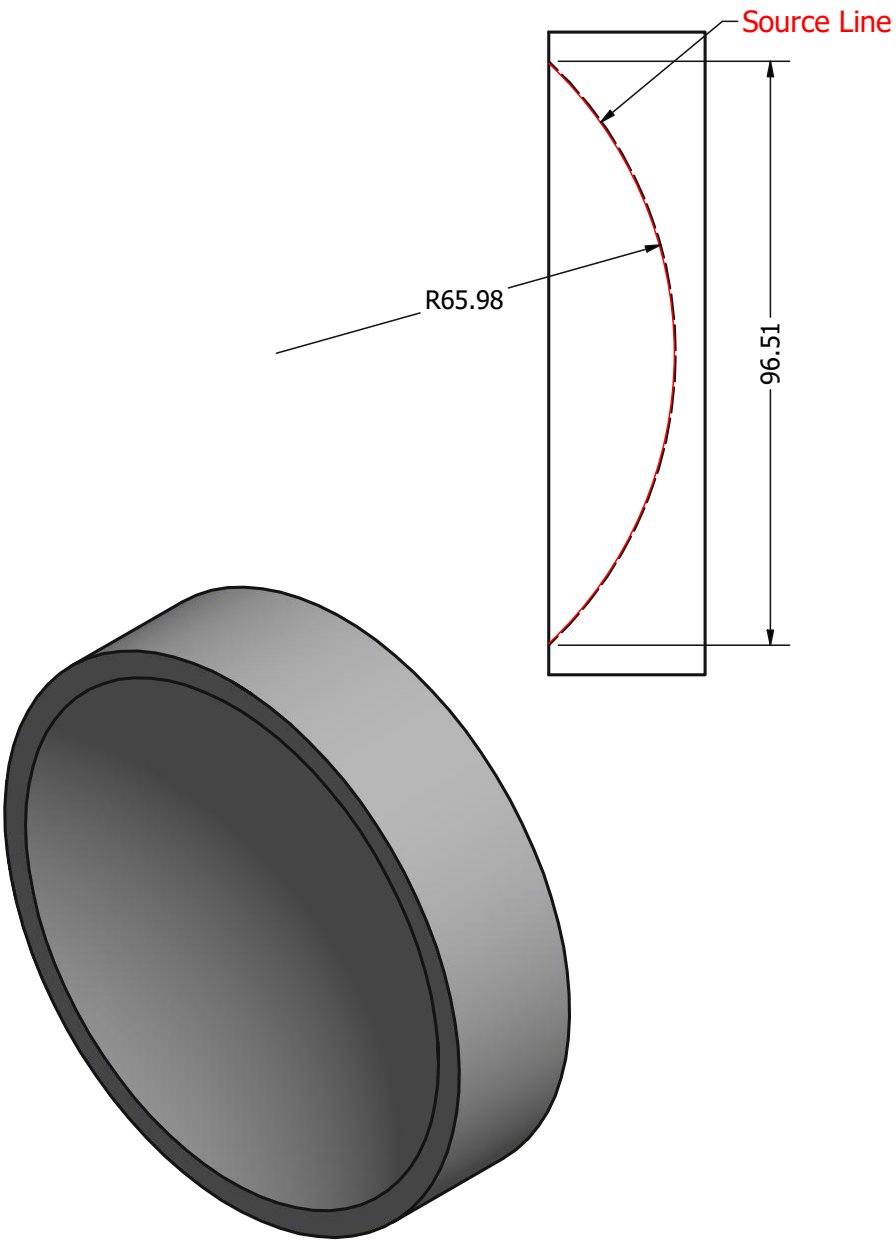


Figure A.5: Drawing of PE applicator with $F_{\#} = 0.68$.

## PE Applicator with $F_{\#} = 0.87$

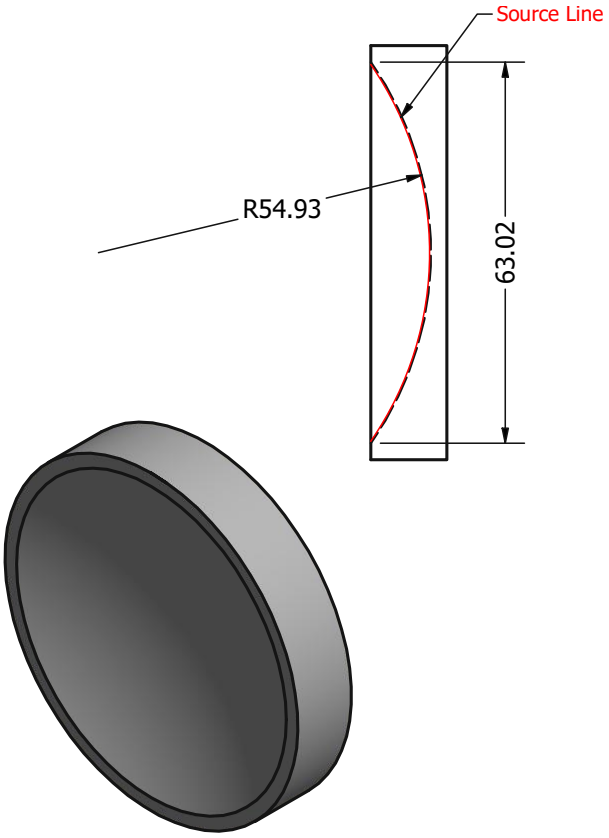


Figure A.6: Drawing of a PE applicator with $F_{\#} = 0.87$.

## A.6 Input Signals

In the following subsections the signals used are described in detail. After generation the signals are scaled pressure-wise to reach the aimed pressure levels, their duration remains unaffected during this process; since the amplitude is very dependent on the resolution and number of source points, the input amplitude is not specified.

### Input Signal for the EH Applicator

The EH signal is composed out of two Gaussian curves using a piecewise function combined at their maxima. For the rising part of the shock wave a Gaussian curve with a small sigma is used, the falling part is a Gaussian curve with a greater sigma. According to equation (5.3) the first curve uses the parameter a = 1, b = 3e-6 and c = 2.55e-07, for the second curve the parameters a = 1, b = 3e-6 and c = 3.8e-06 are used.

### Input Signal for the EM Applicator

In contrast to the signal of the EH applicator, the EM signal is a sum of multiple Gaussian curves with the following parameters of the equation 5.3:

| Curve number | $a$ | $b$ | $c$ |
|---|---|---|---|
| 1 | -0.11 | 1.88e-6 | 0.87e-6 |
| 2 | 1 | 2.84e-6 | 0.65e-6 |
| 3 | -0.15 | 5.52e-6 | 0.95e-6 |

### Input Signal for the PE Applicator

The PE input signal is similar generated as the EM signal, the parameters vary though:

| Curve number | $a$ | $b$ | $c$ |
|---|---|---|---|
| 1 | 1 | 2.5e-6 | 0.3666e-6 |
| 2 | 0.5833 | -142.8e-6 | 41.5425e-6 |
| 3 | 0.0934 | 2.45e-6 | 0.5855e-6 |
| 4 | -0.8292 | 2.45e-6 | 0.5102e-6 |
| 5 | -0.0014 | 0.42e-6 | 0.7057e-6 |

## A.7 Pressure Zones in the Empty Water Bath

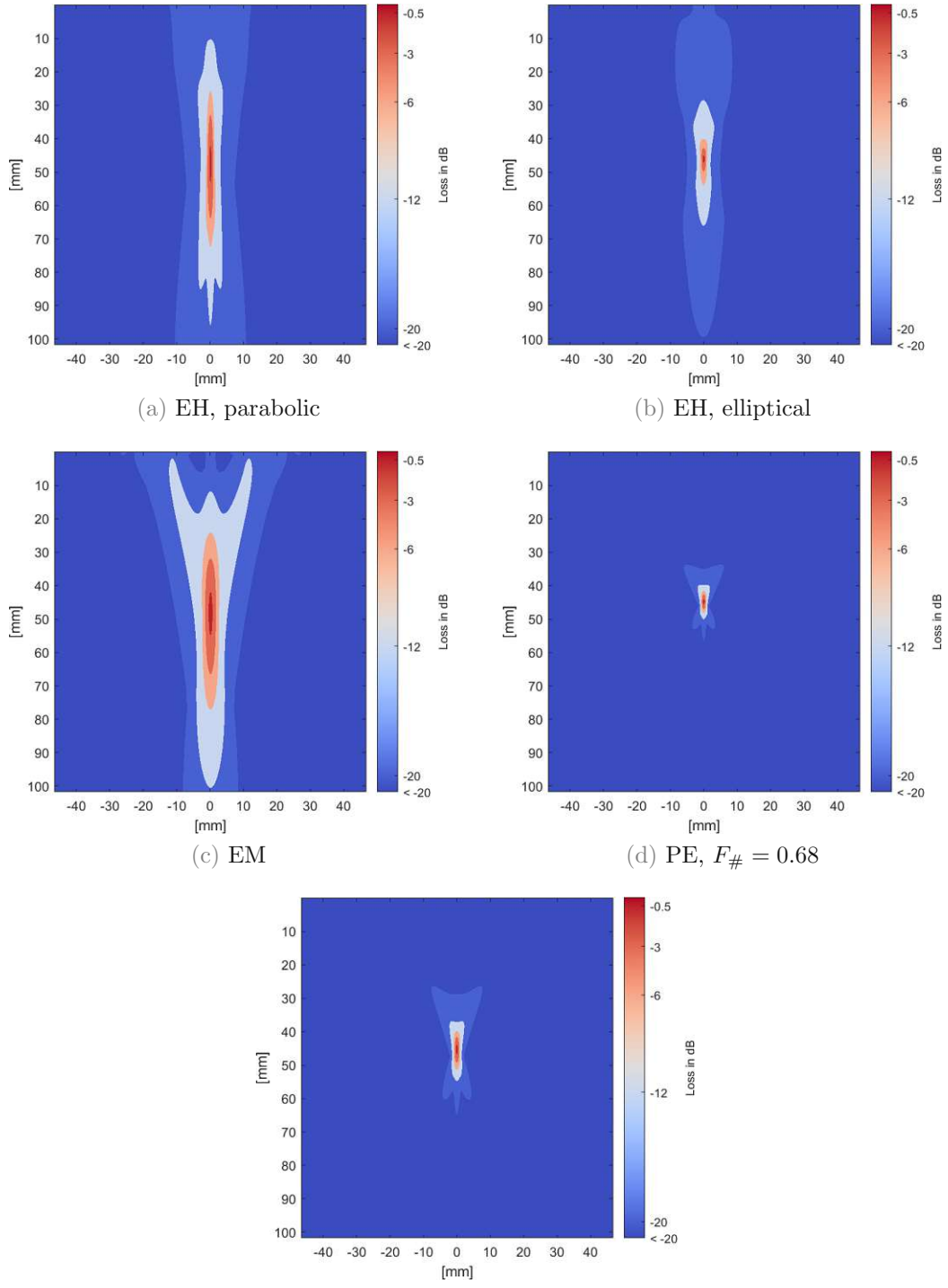


(a) EH, parabolic

(b) EH, elliptical

(c) EM

(d) PE, $F_{\#} = 0.68$

(e) PE, $F_{\#} = 0.87$

Figure A.7: Longitudinal section of the pressure zones in an empty water bath.

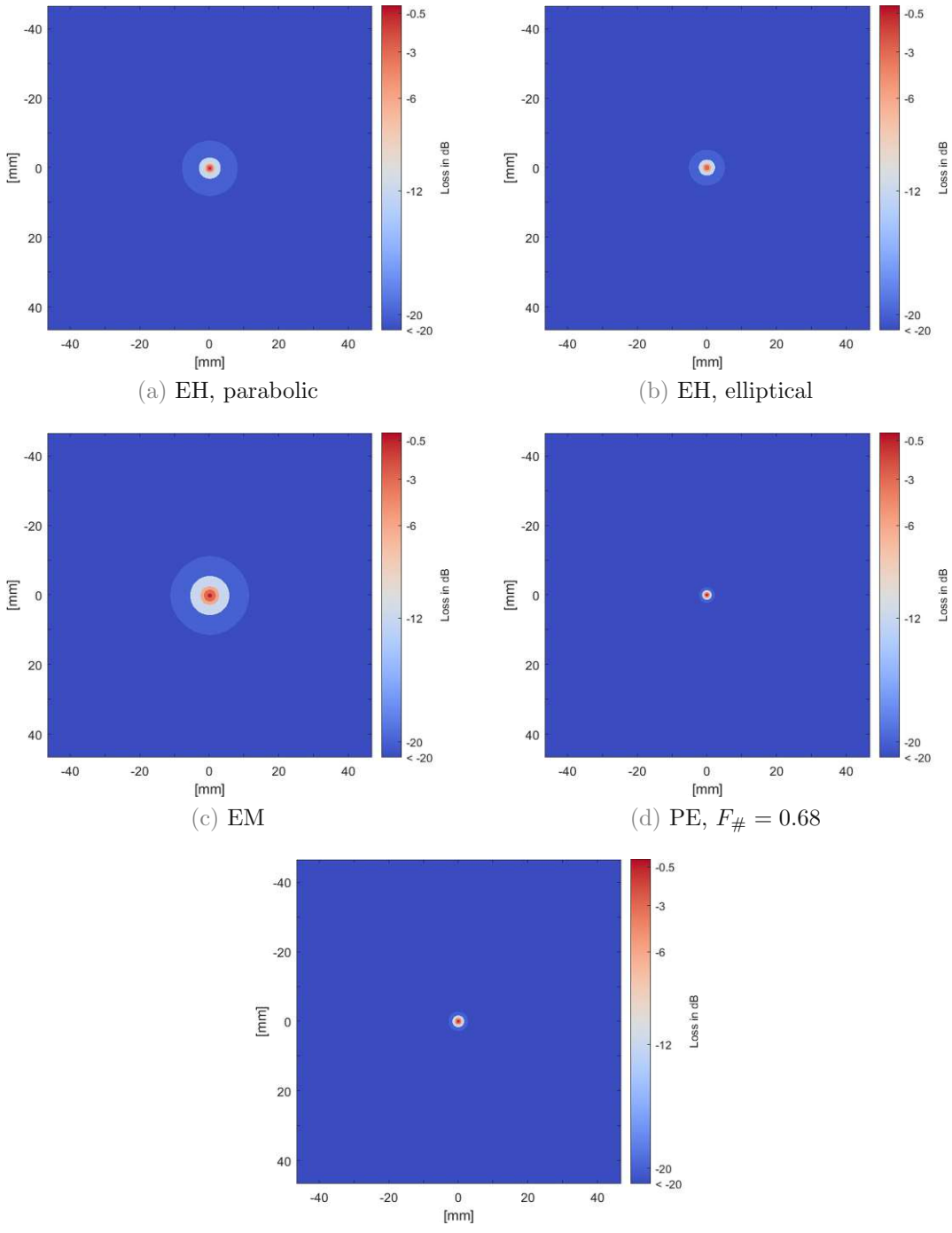


(a) EH, parabolic

(b) EH, elliptical

(c) EM

(d) PE, $F_{\#} = 0.68$

(e) PE, $F_{\#} = 0.87$

Figure A.8: Cross section of the pressure zones in an empty water bath.

## A.8 Pressure Zones with the CT

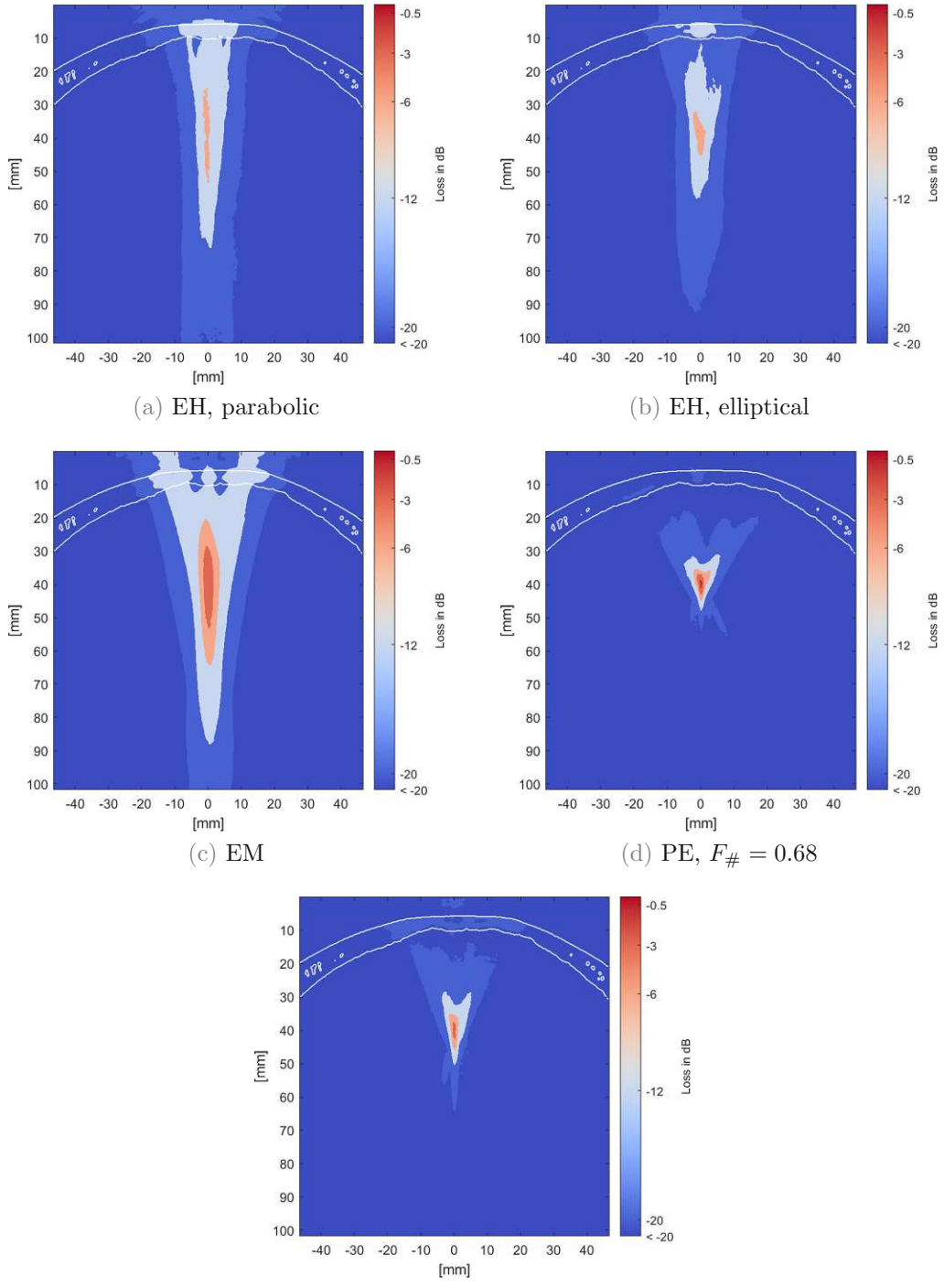


(a) EH, parabolic

(b) EH, elliptical

(c) EM

(d) PE, $F_{\#} = 0.68$

(e) PE, $F_{\#} = 0.87$

Figure A.9: Longitudinal section of the pressure zones with the CT, using the Pichardo [78] attenuation model.

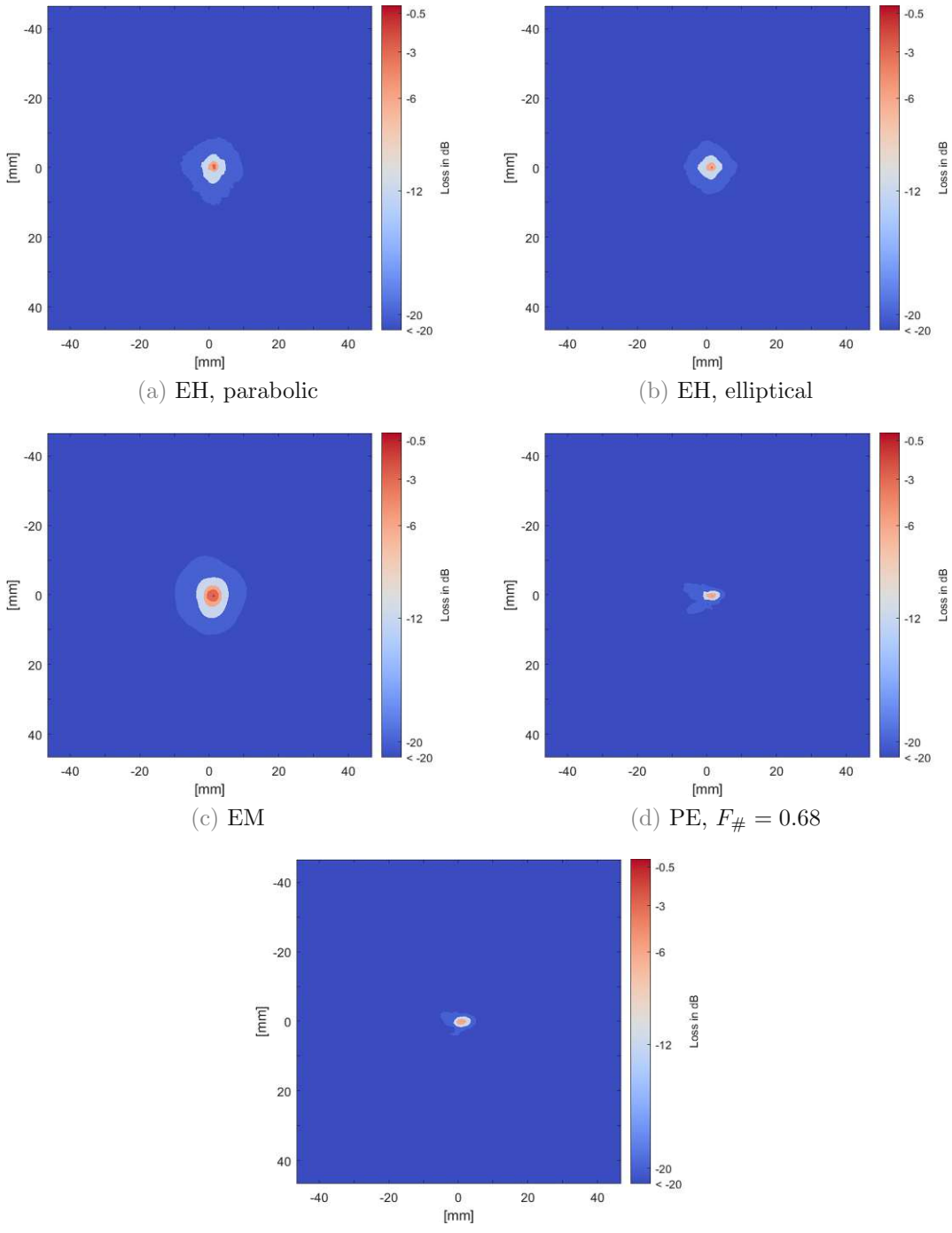


(a) EH, parabolic

(b) EH, elliptical

(c) EM

(d) PE, $F_{\#} = 0.68$

(e) PE, $F_{\#} = 0.87$

Figure A.10: Cross section of the pressure zones with the CT, using the Pichardo [78] attenuation model.

## A.9 Attenuation Models Result

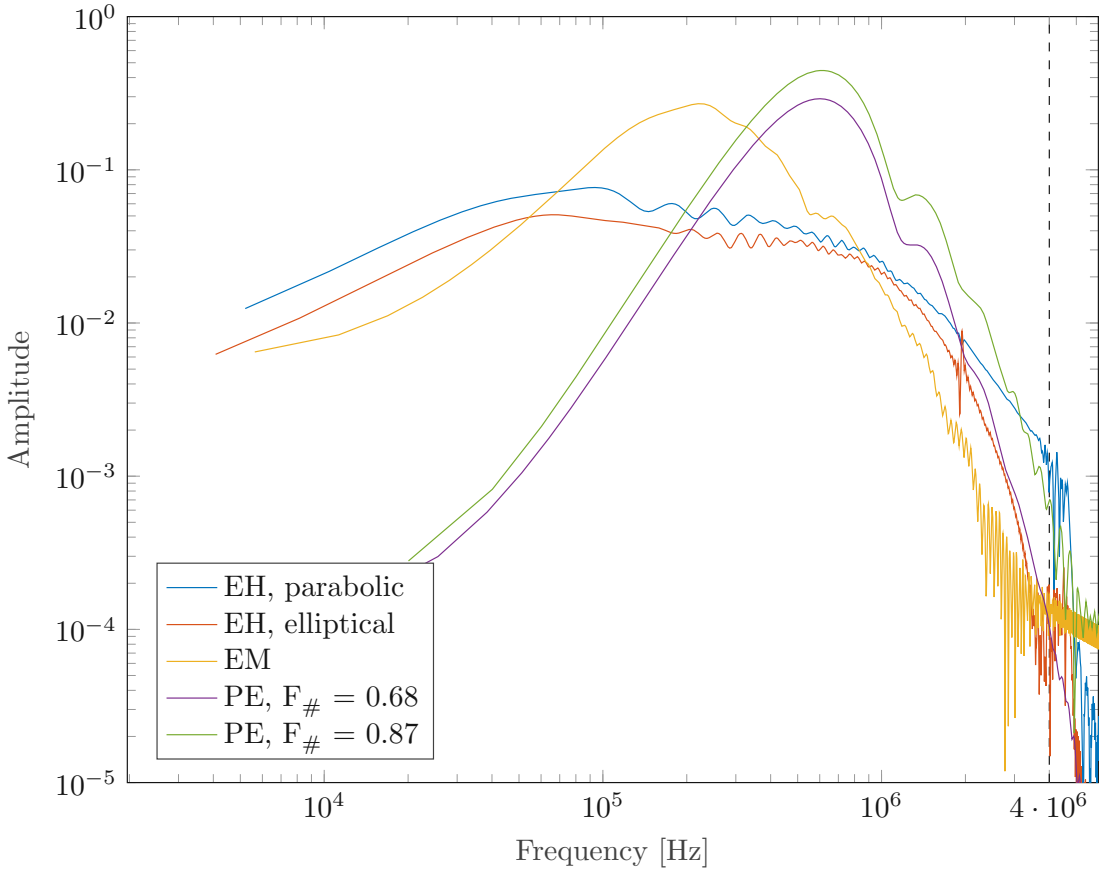


Figure A.11: Frequency spectra of the pressure signals presented in figure 7.5 of the simulations with the homogenous skull attenuation coefficients on the applicators axis closest to their respective focal centre, with a cut-off frequency of 4 MHz.

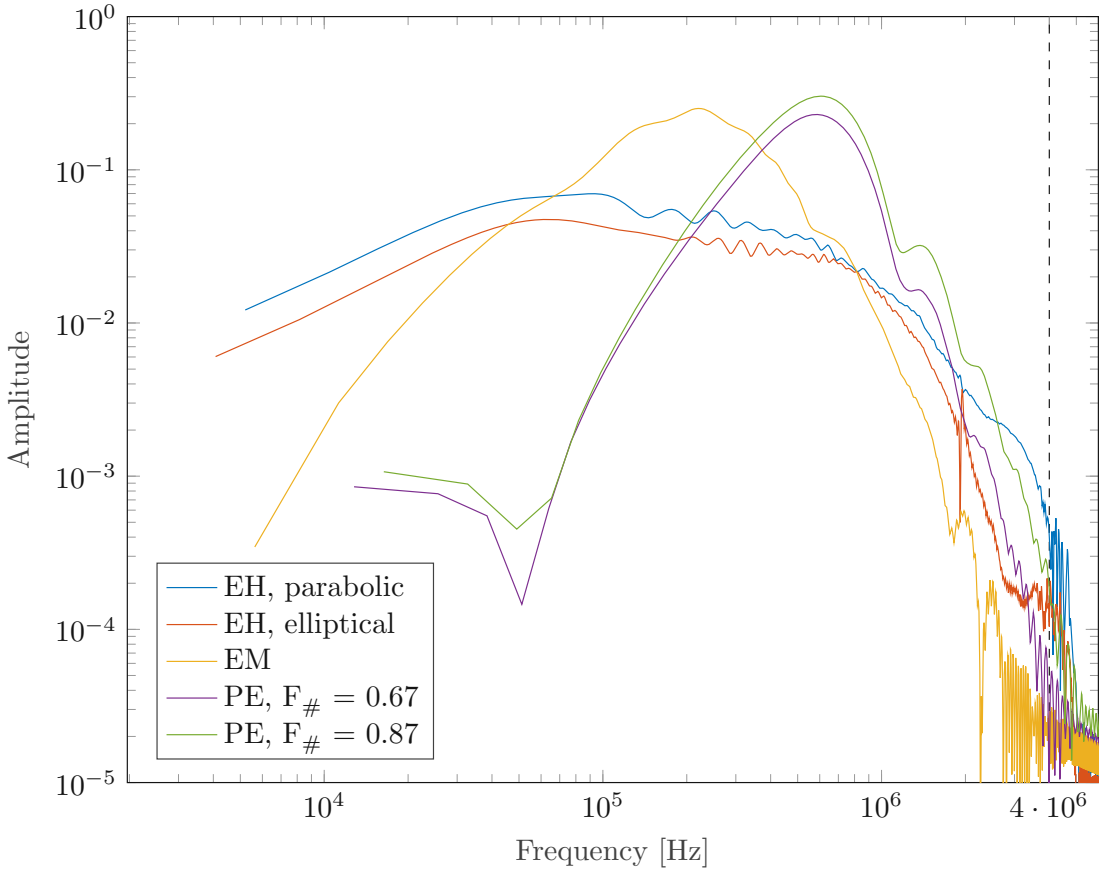


Figure A.12: Frequency spectra of the pressure signals presented in figure 7.5 of the simulations with the attenuation model according to Mcdannold et al. [61] on the applicators axis closest to their respective focal centre, with a cut-off frequency of 4 MHz.

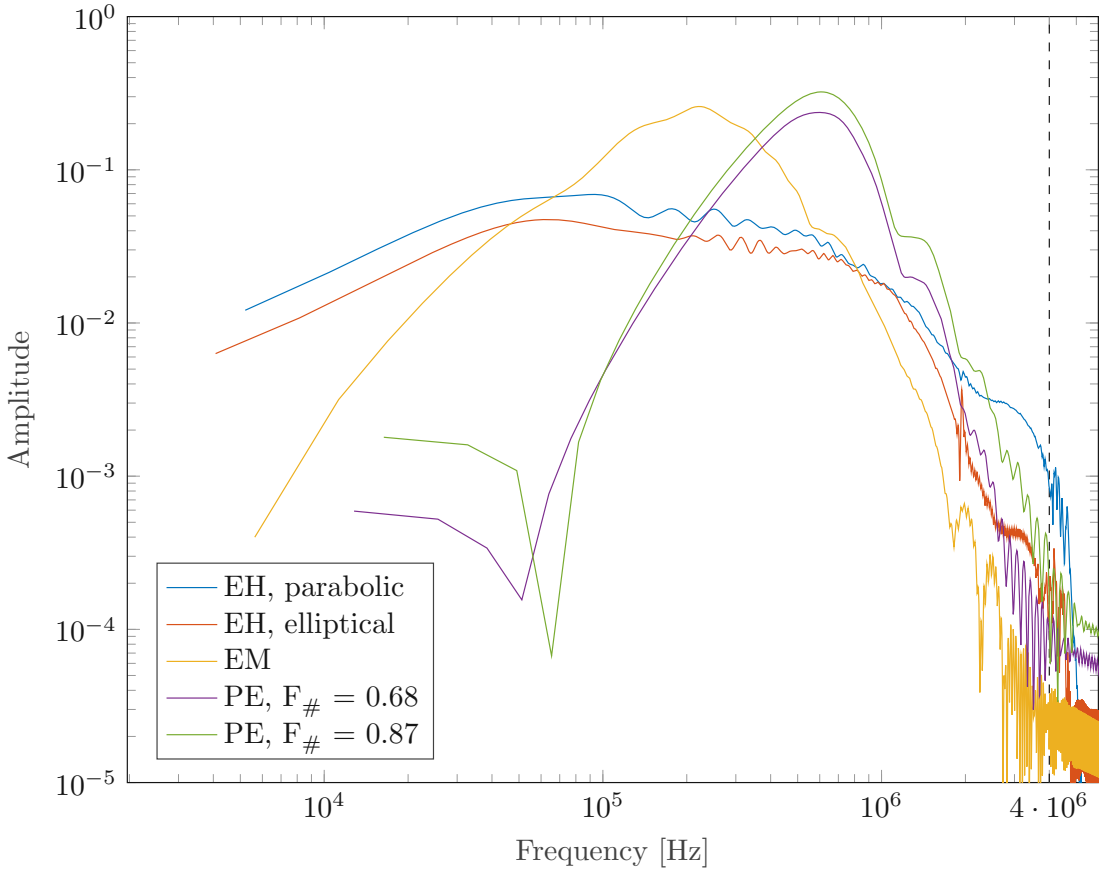


Figure A.13: Frequency spectra of the pressure signals presented in figure 7.5 of the simulations with the attenuation model according to Pichardo et al. [78] on the applicators axis closest to their respective focal centre, with a cut-off frequency of 4 MHz.

# Books

[2] Haim A. *Basics of Biomedical Ultrasound for Engineers*. Wiley, 2010. ISBN: 978-0-470-46547-9.

[6] Pierce AD. *Introduction to its Physical Principles and Applications*. Springer, 1981. ISBN: 978-3-030-11213-4.

[8] Loske AM. *Medical and Biomedical Applications of Shock Waves*. Springer, 2017. ISBN: 978-3-319-47568-4.

[14] Bamber J. C. "Attenuation and Absorption". In: *Physical Principles of Medical Ultrasonics*. John Wiley & Sons, Ltd, 2004. Chap. 4, pp. 93–166. ISBN: 9780470093979.

[24] Paulsen E and Waschke J. *Duale Reihe: Anatomie*. Elsevier, 2017. ISBN: 978-3-437-44023-6.

[28] Aumüller G, Aust G, Engele J, Kirsch J, Mayerhofer A, Mense S, Reißig D, Salvetter J, Schmidt W, Schmitz F, Schulte E, Spanel-Borowski K, Wennemuth G, Wurzinger LJ and Zilch H G. *Duale Reihe: Anatomie*. Thieme, 2014. ISBN: 978-3-13-136043-4.

[31] Kuttruff H. *Physik und Technik des Ultraschalls*. Hirzel Verlag, 1988. ISBN: 3-7776-0427-5.

[59] G. Müller and M. Möser. *Handbook of Engineering Acoustics*. Springer Berlin Heidelberg, 2012. ISBN: 9783540694601.

[65] Wess O. "Physics and Technique of Shock Wave Lithotripsy (SWL)". In: Oct. 2012, pp. 301–311. ISBN: 978-1-4471-4383-3.

[75] Cleveland RO and McAteer JA. "Physics of Shock-Wave Lithotripsy". In: *Smith's Textbook of Endourology*. John Wiley & Sons, Ltd, 2012. Chap. 49, pp. 527–558. ISBN: 9781444345148.

[91] Siebert W and Buch M. *Extracorporeal Shock Waves in Orthopaedics*. Springer, 1998. ISBN: 978-3-540-63092-0.

# Articles

[1] Grisey A, Yon S, Letort V and Lafitte P. "Simulation of high-intensity focused ultrasound lesions in presence of boiling". In: *Journal of Therapeutic Ultrasound* 4 (Dec. 2016).

[3] Maxwell A, Sapozhnikov O, Bailey M, Crum L, Xu Z, Fowlkes B, Cain C and Khokhlova V. "Disintegration of tissue using high intensity focused ultrasound: two approaches that utilize shock waves". In: *Acoustics Today* 8.4 (2012).

[4] Neisius A, Smith NB, Sankin G, Kuntz NJ, Madden JF, Fovargue DE, Mitran S, Lipkin ME, Simmons WN, Preminger GM and Zhong P. "Improving the lens design and performance of a contemporary electromagnetic shock wave lithotripter". In: *Proceedings of the National Academy of Sciences* 111.13 (2014), E1167–E1175. ISSN: 0027-8424.

[5] Weihs A, Fuchs C, Teuschl A, Hartinger J, Slezak P, Mittermayr R, Redl H, Junger W, Sitte H and Rünzler D. "Shock Wave Treatment Enhances Cell Proliferation and Improves Wound Healing by ATP Release-coupled Extracellular Signal-regulated Kinase (ERK) Activation". In: *Journal of Biological Chemistry* (Aug. 2014).

[7] Coleman AJ and John ES. "A survey of the acoustic output of commercial extracorporeal shock wave lithotripters". In: *Ultrasound in Medicine & Biology* 15.3 (1989), pp. 213 –227. ISSN: 0301-5629.

[9] Sturtevant B, Pantea C and Sinha D. "Determination of the Acoustic Nonlinearity Parameter in Liquid Water up to 250 degrees C and 14 MPa". In: *IEEE International Ultrasonics Symposium, IUS* (Oct. 2012), pp. 285–288.

[10] Treeby BE. "Modeling nonlinear wave propagation on nonuniform grids using a mapped k-space pseudospectral method". In: *IEEE Transactions on Ultrasonics, Ferroelectrics, and Frequency Control (Volume: 60 , Issue: 10 , Oct. 2013)* (2013).

[11] Treeby BE and Cox BT. "Modeling power law absorption and dispersion for acoustic propagation using the fractional Laplacian". In: *The Journal of the Acoustical Society of America 130, 610 (2011)* (2010).

[12] Treeby BE and Saratoon T. "The contribution of shear wave absorption to ultrasound heating in bones: Coupled elastic and thermal modeling". In: (2015), pp. 1–4.

[13] Leif Bjørnø. "Introduction to Nonlinear Acoustics". In: *Physics Procedia* 3 (Jan. 2010), pp. 5–16.

[15] Jiang C, Li D, Xu F, Li Y, Liu C and Ta D. "Numerical Evaluation of the Influence of Skull Heterogeneity on Transcranial Ultrasonic Focusing". In: *Frontiers in Neuroscience* 14 (2020), p. 317. ISSN: 1662-453X.

[16] Perez C, Chen H, Matula TJ, Karzova M and Khokhlova VA. "Acoustic field characterization of the Duolith: measurements and modeling of a clinical shock wave therapy device." In: *The Journal of the Acoustical Society of America* (2013).

[17] Slezak C, Rose R, Jilge JM, Nuster R, Hercher D and Slezak P. "Physical Considerations for In Vitro ESWT Research Design". In: *International Journal of Molecular Sciences* 23.1 (2022). ISSN: 1422-0067.

[18] Shin CH, Pahk KJ, Kim SH, Kim H and Oh SJ. "73P - Boiling histotripsy-induced mechanical ablation modulates tumour microenvironment by promoting immunogenic cell death of cancers". In: *Annals of Oncology* 30 (2019). Abstract Book of the 44th ESMO Congress (ESMO 2019) 27 September – 1 October 2019, Barcelona, Spain, pp. v20–v21. ISSN: 0923-7534.

[19] Connor CW, Clement GT and Hynynen K. "A unified model for the speed of sound in cranial bone based on genetic algorithm optimization". In: *Physics in Medicine and Biology* 47.22 (2002), pp. 3925–3944.

[20] Darrow DP. "Focused Ultrasound for Neuromodulatio". In: *Neurotherapeutics : the journal of the American Society for Experimental NeuroTherapeutics, 16(1)* (2019), pp. 88–99.

[21] Mast DT. "Empirical relationships between acoustic parameters in human soft tissues". In: *Acoustics Research Letters Online* 1.2 (2000), pp. 37–42.

[22] Bossy E, Laugier P, Peyrin F and Padilla F. "Attenuation in trabecular bone: A comparison between numerical simulation and experimental results in human femur". In: *The Journal of the Acoustical Society of America* 122.4 (2007), pp. 2469–2475.

[23] Martin E, Ling YT and Treeby BE. "Simulating Focused Ultrasound Transducers Using Discrete Sources on Regular Cartesian Grids". In: *IEEE Transactions on Ultrasonics, Ferroelectrics, and Frequency Control* 63.10 (2016), pp. 1535–1542.

[25] Lillie EM, Urban JE, Lynch SK, Weaver AA and Stitzel JD. "Evaluation of Skull Cortical Thickness Changes With Age and Sex From Computed Tomography Scans". In: *Journal of Bone and Mineral Research* 31.2 (2016), pp. 299–307.

[26] Wise ES, Robertson JLB, Cox BT and Treeby BE. "Staircase-free acoustic sources for grid-based models of wave propagation". In: (2017), pp. 1–4. ISSN: 1948-5727.

[27] Fry FJ. "Transkull transmission of an intense focused ultrasonic beam". In: *Ultrasound in Medicine & Biology* 3.2 (1977), pp. 179 –184. ISSN: 0301-5629.

[29] Pinton G, Aubry JF, Bossy E, Muller M, Pernot M and Tanter M. "Attenuation, scattering, and absorption of ultrasound in the skull bone". In: *Medical Physics* 39.1 (2012), pp. 299–307.

[30] Clement GT, Sun J, Giesecke T and Hynynen K. "A hemisphere array for non-invasive ultrasound brain therapy and surgery". In: *Physics in Medicine and Biology* 45.12 (2000), pp. 3707–3719.

[32] Porst H. "Review of the Current Status of Low Intensity Extracorporeal Shockwave Therapy (Li-ESWT) in Erectile Dysfunction (ED), Peyronie's Disease (PD), and Sexual Rehabilitation After Radical Prostatectomy With Special Focus on Technical Aspects of the Different Marketed ESWT Devices Including Personal Experiences in 350 Patients". In: *Sexual Medicine Reviews* 9.1 (2021), pp. 93–122. ISSN: 2050-0521.

[33] Everding J, Roßlenbroich S and Raschke MJ. "Ultraschall und Stoßwelle in der Pseudarthrosentherapie". In: *Trauma und Berufskrankheit* (2017).

[34] Lautz J, Sankin G and Zhong P. "Synergistic interaction between stress waves and cavitation is important for successful comminution of residual stone fragments in shock wave lithotripsy". In: *The Journal of the Acoustical Society of America* 130.4 (2011), pp. 2538–2538.

[35] Pemberton J. "Extra-corporeal shock wave lithotripsy". In: *Postgraduate Medical Journal (1987) 63* (1987).

[36] Staudenraus J and Eisenmenger W. "Fibre-optic probe hydrophone for ultrasonic and shock-wave measurements in water". In: *Ultrasonics* 31.4 (1993), pp. 267 –273. ISSN: 0041-624X.

[37] Sun J and Hynynen K. "Focusing of therapeutic ultrasound through a human skull: a numerical study". In: *J Acoust Soc Am.* 104(3 Pt 1) (1998 Sep), pp. 1705–15.

[38] Sun J and Hynynen K. "The potential of transskull ultrasound therapy and surgery using the maximum available skull surface area". In: *The Journal of the Acoustical Society of America* 105.4 (1999), pp. 2519–2527.

[39] Thomas J and Fink MA. "Ultrasonic beam focusing through tissue inhomogeneities with a time reversal mirror: application to transskull therapy". In: *IEEE Transactions on Ultrasonics, Ferroelectrics, and Frequency Control* 43.6 (1996), pp. 1122–1129.

[40] Freund JB, Colonius T and Evan AP. "A cumulative shear mechanism for tissue damage initiation in shock-wave lithotripsy." In: *Ultrasound in medicine & biology* ().

[41] Wang JC and Zhou Y. "Shifting the Split Reflectors to Enhance Stone Fragmentation of Shock Wave Lithotripsy". In: *Ultrasound in Medicine & Biology* 42.8 (2016), pp. 1876 –1889. ISSN: 0301-5629.

[42] Mueller JK, Ai L, Bansal P and Legon W. "Numerical evaluation of the skull for human neuromodulation with transcranial focused ultrasound". In: *Journal of Neural Engineering* 14.6 (2017).

[43] Robertson JLB, Cox BT, Jaros J and Treeby BE. "Accurate simulation of transcranial ultrasound propagation for ultrasonic neuromodulation and stimulation". In: *The Journal of the Acoustical Society of America* 141.3 (2017), pp. 1726–1738.

[44] Dietz-Laursonn K, Beckmann R, Ginter S, Radermacher K and de la Fuente M. "In-vitro cell treatment with focused shockwaves-influence of the experimental setup on the sound field and biological reaction". In: *Journal of therapeutic ultrasound* (2016).

[45] Hynynen K and Sun J. "Trans-skull ultrasound therapy: the feasibility of using image-derived skull thickness information to correct the phase distortion". In: *IEEE transactions on ultrasonics, ferroelectrics, and frequency control* 46.3 (1999), 752—755. ISSN: 0885-3010.

[46] Sternecker K, Geist J, Beggel S, Dietz-Laursonn K, de la Fuente M, Frank HG, Furia JP, Milz S and Schmitz C. "Exposure of zebra mussels to extracorporeal shock waves demonstrates formation of new mineralized tissue inside and outside the focus zone." In: *Biology open* (2018).

[47] Wang K, Teoh E, Jaros J and Treeby BE. "Modelling nonlinear ultrasound propagation in absorbing media using the k-Wave toolbox: experimental validation". In: (2012), pp. 523–526.

[48] Yoon K, Lee W, Croce P, Cammalleri A and Yoo SS. "Multi-resolution simulation of focused ultrasound propagation through ovine skull from a single-element transducer". In: *Physics in Medicine & Biology* 63.10 (2018).

[50] Pahk KJ, Gélat P, Kim H and Saffari N. "Bubble dynamics in boiling histotripsy". In: *Ultrasound in Medicine & Biology* 44 (Sept. 2018).

[51] Bjørnø L. "Characterization of biological media by means of their non-linearity". In: *Ultrasonics* 24.5 (1986), pp. 254–259. ISSN: 0041-624X.

[52] Mohammadi L, Behnam H, Tavakkoli J and Avanaki M. "Skull's photoacoustic attenuation and dispersion modeling with deterministic ray-tracing: Towards real-time aberration correction". In: *Sensors* 19.2 (2019), p. 345.

[53] Reynolds LF, Kroczak T and Pace KT. "Indications and contraindications forshock wave lithotripsy and how to improveoutcomes". In: *Asian Journey of Urology (2018)* (2018).

[54] Bailey M, Khokhlova V, Sapozhnikov O, Kargl S and Crum L. "Physical mechanisms of the therapeutic effect of ultrasound (a review)". In: *Acoustical Physics* 49.4 (July 2003), pp. 369–388.

[55] Daffertshofer M, Gass A, Ringleb P, Sitzer M, Sliwka U, Els T, Sedlaczek O, Koroshetz WJ and Hennerici MG. "Transcranial Low-Frequency Ultrasound-Mediated Thrombolysis in Brain Ischemia". In: *Stroke* 36.7 (2005), pp. 1441–1446.

[56] Gutierrez M, Penilla E, Leija L, Vera A, Garay J and Aguilar G. "Novel Cranial Implants of Yttria-Stabilized Zirconia as Acoustic Windows for Ultrasonic Brain Therapy". In: *Advanced Healthcare Materials* 6 (Nov. 2017), p. 1700214.

[57] Obert M, Kubelt C, Schaaf T, Dassinger B, Grams A, Gizewski ER, Krombach GA and Verhoff MA. "Aging adult skull remains through radiological density estimates: A comparison of different computed tomography systems and the use of computer simulations to judge the accuracy of results". In: *Forensic Science International* 228.1 (2013), 179.e1–179.e7. ISSN: 0379-0738.

[60] Haffner N, Antonic V, Smolen D, Slezak P, Schaden W, Mittermayr R and Stojadinovic A. "Extracorporeal shockwave therapy (ESWT) ameliorates healing of tibial fracture non-union unresponsive to conventional therapy". In: *Injury* 47.7 (July 2016), pp. 1506–1513.

[61] McDannold N, White JP and Cosgrove R. "Elementwise approach for simulating transcranial MRI-guided focused ultrasound thermal ablation". In: *Physical Review Research* 1.3 (2019).

[62] Reinhardt N, Dietz-Laursonn K, Janzen M, Radermacher K, Bach C and de la Fuente M. "Experimental setup for evaluation of cavitation effects in ESWL". In: *Current Directions in Biomedical Engineering* 4.1 (2018).

[63] Smith N and Zhong P. "Stone comminution correlates with the average peak pressure incidenton a stone during shock wave lithotripsy". In: *Journal of Biomechanics 45* (2012).

[66] Wess O. "Physikalische Grundlagen derextrakorporalen Stoßwellentherapie". In: *Journal für Mineralstoffwechsel & Muskuloskelettale Erkrankungen* 11.4 (2004), pp. 7–18.

[67] Patel P, Huang C, Molina M and Ramasamy R. "Clinical trial update on shockwave therapy and future of erectile function restoration". In: *International Journal of Impotence Research* 31.3 (2019), pp. 206–208.

[68] Pouget P, Frey S, Ahnine H, Attali D, Claron J, Constans C, Aubry JF and Arcizet F. "Neuronavigated Repetitive Transcranial Ultrasound Stimulation Induces Long-Lasting and Reversible Effects on Oculomotor Performance in Non-human Primates". In: *Frontiers in Physiology* 11 (2020), p. 1042. ISSN: 1664-042X.

[69] Rosnitskiy P, Gavrilov L, Yuldashev P, Sapozhnikov O and Khokhlova V. "On the possibility of using multi-element phased arrays for shock-wave action on deep brain structures". In: *Acoustical Physics* 63.5 (Sept. 2017), pp. 531–541.

[70] Rosnitskiy P, Yuldashev P and Khokhlova V. "Effect of the angular aperture of medical ultrasound transducers on the parameters of nonlinear ultrasound field with shocks at the focus". In: *Acoustical Physics* 61.3 (2015), pp. 301–307.

[71] Rosnitskiy P, Yuldashev Petr, Sapozhnikov O, Gavrilov L and Khokhlova V. "Simulation of nonlinear trans-skull focusing and formation of shocks in brain using a fully populated ultrasound array with aberration correction". In: *The Journal of the Acoustical Society of America* 146.3 (2019), pp. 1786–1798.

[74] Beisteiner R, Matt E, Fan C, Baldysiak H, Schönfeld M, Philippi Novak T, Amini A, Aslan T, Reinecke R, Lehrner J, Weber A, Reime U, Goldenstedt C, Marlinghaus E, Hallett M and Lohse-Busch H. "Transcranial Pulse Stimulation with Ultrasound in Alzheimer's Disease—A New Navigated Focal Brain Therapy". In: *Advanced Science* 7.3 (2020), p. 1902583.

[76] Leung S, Moore D, Webb T, Snell J, Ghanouni P and Pauly K. "Transcranial focused ultrasound phase correction using the hybrid angular spectrum method". In: *Scientific Reports* 11 (Mar. 2021).

[77] Pichardo S, Moreno-Hernández C, Drainville RA, Sin V, Curiel L and Hynynen K. "A viscoelastic model for the prediction of transcranial ultrasound propagation: application for the estimation of shear acoustic properties in the human skull". In: *Physics in Medicine & Biology* 62.17 (2017), p. 6938.

[78] Pichardo S, Sin VW and Hynynen K. "Multi-frequency characterization of the speed of sound and attenuation coefficient for longitudinal transmission of freshly excised human skulls". In: *Physics in Medicine and Biology* 56.1 (2010), pp. 219–250.

[80] Goss SA, Johnston RL and Dunn F. "Comprehensive compilation of empirical ultrasonic properties of mammalian tissues". In: *The Journal of the Acoustical Society of America* 64.2 (1978), pp. 423–457.

[81] Schoen SJ and Arvanitis C. "Heterogeneous angular spectrum method for trans-skull imaging and focusing". In: *The Journal of the Acoustical Society of America* 146.4 (2019), pp. 2813–2813.

[86] Schneider U, Pedroni E and Lomax A. "The calibration of CT Hounsfield units for radiotherapy treatment planning". In: *Physics in Medicine and Biology* 41.1 (1996), pp. 111–124.

[88] Dedes V, Stergioulas A, Kipreos G, Dede A, Mitseas A and Panoutsopoulos G. "Effectiveness and Safety of Shockwave Therapy in Tendinopathies". In: *Materia Socio Medica* 30.2 (2018), p. 141.

[89] Khokhlova V, Yuldashev P, Rosnitskiy P, Maxwell AD, Kreider W, Bailey MR and Sapozhnikov O. "Design of HIFU Transducers to Generate Specific Nonlinear Ultrasound Fields". In: *Physics Procedia* 87 (2016). 44th Annual Symposium of the Ultrasonic Industry Association, UIA 44th Symposium, 20-22 April 2015, Washington, DC, USA and of the 45th Annual Symposium of the Ultrasonic Industry Association, UIA 45th Symposium, 4-6 April 2016, Washington, DC, USA, pp. 132 –138. ISSN: 1875-3892.

[90] Legon W, Bansal P, Tyshynsky R, Ai L and Mueller JK. "Transcranial focused ultrasound neuromodulation of the human primary motor cortex". In: *Scientific reports* 8.1 (2018), pp. 1–14.

[92] Xiong Y, Wu Q, Mi B, Zhou W, Liu Y, Liu J, Xue H, Hu L, Panayi A and LiuG. "Comparison of efficacy of shock-wave therapy versus corticosteroids in plantar fasciitis: a meta-analysis of randomized controlled trials". In: *Archives of Orthopaedic and Trauma Surgery* 139 (Apr. 2019).

## Online

[49] *K-Wave Documentation: A MATLAB toolbox for the time-domain simulation of acoustic wave fields*. http://www.k-wave.org/documentation/k-wave.php, visited on 20.05.20.

[58] *MTS medical*. https://www.mts-medical.com, visited on 07.09.21.

[64] *Nondestructive Evaluation Techniques*. https://www.nde-ed.org/NDETechniques/Ultrasonics/index.xhtml, visited on 23.04.21.

[72] *Piezo-ceramic Transducers*. https://www.acoustics.co.uk/product/piezo-ceramic-transducers/, visited on 23.04.21.

[73] *Piezoelectric materials for ultrasonic probes*. https://www.ndt.net/article/platte2/platte2.htm, visited on 23.04.21.

[79] *S3373 – Normal beam transducer*. https://acs-international.com/instruments/transducers/piezoelectric-1-10-mhz/single-crystal/s3373-normal-beam-transducer/, visited on 23.04.21.

[82] *Storz Duolith SD1 Sepia*. https://www.storzmedical.com/en/disciplines/urology/product-overview/duolith-sd1-ultra-uro, visited on 07.09.21.

[83] *Storz Duolith SD1 Sepia Manual*. https://www.manualslib.com/manual/1600481/Chattanooga-Intelect-Focus-Shockwave.html, visited on 07.09.21.

[84] *Swiss PiezoClast*. https://www.mtr-ag.ch/swiss-piezoclast.html, visited on 23.04.21.

[85] *Therapy sources and focal zones designed for individual indications*. https://elvation.de/en/piezo-stosswelle/eswt/therapiequellen/, visited on 23.04.21.

[87] *Urogold Brochure*. http://www.mts-medical.com/wp-content/uploads/2016/04/MTS_MDOC_UG100_brochure_8S_E_15-08-19.pdf, visited on 21.05.21.